Title
Search for topological semimetal and topological superconductor candidates

Author
Emmanouilidou, Evdoxia

Publication Date
2020

Peer reviewed|Thesis/dissertation

UNIVERSITY OF CALIFORNIA

Los Angeles

Search for topological semimetal and topological superconductor candidates

A dissertation submitted in partial satisfaction

of the requirements for the degree

Doctor of Philosophy in Physics

by

Evdoxia Emmanouilidou

2020

ABSTRACT OF THE DISSERTATION

Search for topological semimetal and topological superconductor candidates

by

Evdoxia Emmanouilidou
Doctor of Philosophy in Physics
University of California, Los Angeles, 2020
Professor Ni Ni, Chair

The discoveries of the two-dimensional quantum Hall effect, the quantum spin Hall effect, and three-dimensional topological insulators started a new era in solid-state physics. Topology soon became a word in most solid state physicists' vocabulary. A topological phase of matter is characterized by a nonzero topological invariant, which is determined by the bulk electronic wavefunctions of a material. The conventional insulators and metals have a zero, or trivial, topological invariant, and their properties are not affected by the topology of their band structure. Topologically non-trivial materials, however, display a host of exotic phenomena in their transport and spectroscopic properties, and band topology has to be invoked to explain them.

Band topology has even emerged as a classification principle of the states of matter, with the topological invariant characterizing the topological class of the materials. Soon after the discovery of topological insulators, topological semimetals were theoretically predicted and experimentally realized. These are gapless systems characterized by protected band crossings with linear energy dispersions resembling those of relativistic particles. The physical realization of these systems is important not only because of the opportunity to study novel quantum phases of matter and emergent phenomena which have led to the discoveries of surface Dirac cones, surface Fermi arcs, the chiral anomaly and colossal photovoltaic effects, but also because they hold promise for applications in quantum devices.

Although it has recently been realized that topological materials are fairly ubiquitous in nature, signatures of their nontrivial topology are still not easily accessible due to the lack of ideal material realizations. For years this was the main obstacle in the study of nodal-line semimetals. For topological physics to be accessible, two things must occur. First, the nodes (line or point) must be very close to the Fermi level and second, there should be no other trivial bands at the Fermi level. The search for material realizations of ideal semimetals of each type is the subject of my dissertation.

An ideal nodal-line semimetal predicted to satisfy both of these criteria is CaAgAs. We are the first group to synthesize single crystals of this material, and study their transport properties and band structure. We additionally studied CaCdGe, a compound with the same crystal structure and topological nodal line, but a much more complicated Fermi surface with trivial bands near the Fermi level. By comparing the transport properties of these two materials, our study provided evidence that the large magnetoresistance and the highly debated linear magnetoresistance seen in topological semimetals might simply be due to electron-hole compensation and charge fluctuations, respectively. Furthermore, a topological surface state was observed in our CaAgAs in our collaborative angle-resolved photoemission spectroscopy experiment, unambiguously proving that this material was correctly dubbed the "hydrogen atom" of nodal-line semimetals.

Experimental work provides key insights that lead to a revision of the theory and thus our understanding of the physics of a material. This is what our study on CuMnAs accomplished. CuMnAs was predicted to be an antiferromagnetic Dirac semimetal, with a topological protection that relied on a theoretically predicted magnetic structure. However, no such structure had ever been experimentally confirmed. In our study, we grew single crystals of CuMnAs, resolved this magnetic structure and showed that it was actually different from the theoretically predicted one. Although this led to the Dirac fermions no longer being protected, our collaborative first-principles calculations found that it leads to the emergence of spin-polarized surface states, a much sought after property for spintronics.

Many of the topological semimetals that are currently being studied were first synthe-

sized decades ago. However, in light of new predictions regarding the topology of their band structure, their properties are now being re-examined. Our studies of $NbGe_2$, a chiral non-centrosymmetric superconductor first studied in the 1970s and recently predicted to host Kramers-Weyl fermions, reveal that it might be possible for this material to harbor a superconducting topological surface state.

The dissertation of Evdoxia Emmanouilidou is approved.

Stuart Brown

Paula Loredana Diaconescu

Ni Ni, Committee Chair

University of California, Los Angeles

2020

To Evripidis

Table of Contents

List of Figures . . . . . **x**

List of Tables . . . . . **xix**

Acknowledgements . . . . . **xx**

Curriculum Vitae . . . . . **xxii**

1 Background and history of three-dimensional topological materials . . . **1**

2 Overview of nontrivial topology, magnetism, quantum oscillations and superconductivity **12**

2.1 The Berry phase 13

2.2 The quantum Hall effect 16

2.3 The Z_2 or Quantum Spin Hall insulator 18

2.4 3D Topological Insulators 20

2.5 Topological semimetals; Weyl, Dirac and Nodal-line 22

2.5.1 Weyl semimetals 22

2.5.2 Dirac semimetals 25

2.5.3 Nodal-line and Kramers-Weyl semimetals 26

2.6 Brief overview of common magnetic interactions and structures and metamagnetic transitions 27

2.7 Elements of magnetotransport in semimetals and topological semimetals . . 30

2.8 Superconductivity 33

3 Experimental methods **37**

3.1 Single crystal growth using the flux method . . . 37
3.2 Crystal structure and composition determination . . . 40
3.2.1 Powder X-ray diffraction . . . 40
3.2.2 Energy dispersive X-ray spectroscopy . . . 40
3.3 Electrical and thermodynamic properties . . . 40
3.3.1 Resistivity, magnetoresistance and Hall resistivity . . . 40
3.3.2 Magnetization . . . 41
3.3.3 Specific heat . . . 41
3.3.4 Single crystal neutron diffraction . . . 42

4 Magnetotransport properties of the single crystalline nodal-line semimetal candidates Ca*TX* (*T*= Ag, Cd; *X*= As, Ge) . . . 43

4.1 Introduction . . . 43
4.1.1 Single crystal growth of CaAgAs and CaCdGe . . . 45
4.2 Transport properties of CaAgAs and CaCdGe . . . 47
4.3 Shubnikov-de Haas oscillations in CaCdGe . . . 53
4.4 Fermiology revealed by quantum oscillations and DFT calculations . . . 57
4.5 Topological surface states revealed by ARPES in CaAgAs . . . 58
4.6 Conclusion and outlook . . . 60

5 Magnetic order induces symmetry breaking in the single-crystalline orthorhombic CuMnAs semimetal . . . 61

5.1 Introduction . . . 61
5.1.1 Single crystal growth of CuMnAs . . . 65
5.2 Electrical transport and thermodynamic properties . . . 68
5.3 The magnetic structures of PA and PB . . . 70

5.4 Bulk band structure calculations with experimentally determined magnetic structure . . . 74
5.5 Spin-flop transition in the orthorhombic antiferromagnetic topological semimetal $Cu_{0.95}MnAs$ . . . 76
5.6 Conclusion . . . 82

6 Fermiology and Type-I superconductivity in the chiral superconductor $NbGe_2$ . . . 83
6.1 Introduction . . . 83
6.1.1 Single crystal growth of $NbGe_2$ . . . 84
6.1.2 Transport properties and Fermiology of $NbGe_2$ . . . 86
6.2 Berry phase revealed by the dHvA oscillations . . . 89
6.3 Quasi linear magnetoresistance arising from open Fermi surfaces . . . 93
6.4 Type-I superconductivity with a full superconducting gap . . . 95
6.5 Conclusion . . . 99

7 Conclusion . . . 101

A Temperature dependent resistance curves for CuMnAs crystals from all synthesis trials . . . 102

B First principles calculations . . . 106

Bibliography . . . 108

List of Figures

1.1 (a),(b) Surface electronic band dispersion in Bi_2Se_3 along the $\bar{\Gamma}$ - $\bar{M}$ and $\bar{\Gamma}$ - $\bar{K}$ momentum-space cuts. (c) The momentum distribution curves from (a) show that two surface bands converge at a single Dirac point at $\bar{\Gamma}$. (d) The 3D BZ and its projection on the (111) plane. (e) The Fermi surface (FS) of the 2D surface states is a circle around Γ if the chemical potential lies inside the band gap. (f) Theoretically calculated electronic structure of the (111) surface in the presence and absence of SOC. Simply degenerate surface bands that cross the Fermi level appear only when SOC is included in the calculations. Taken from [10]. 3

1.2 Spin momentum locking in Bi_2Te_3 using spin-resolved ARPES. Taken from [11]. 4

1.3 (a) The non-primitive tetragonal unit cell of Cd_3As_2, which consists of 160 atoms. (b) The band structure, with 3D Dirac band touching points near the Γ point. (c), (d) The valence (c) and conduction (d) bands near the Γ point mapped using ARPES. Adapted from [13]. 5

1.4 The crystal structure and electronic structure of Na_3Bi. Taken from [18]. 7

1.5 NLMR in Na_3Bi due to charge pumping between the two branches of the lowest LL. Taken from [20]. 8

1.6 (a) The crystal structure of TaAs, with the red arrow indicating where the crystal can be cleaved. (b) The FS on the (001) surface of TaAs, including Fermi arcs as well as trivial Fermi pockets. (c) A schematic of the Fermi arcs connecting W1 and W2 nodes with chiral charges $\pm$ 2 and 1 respectively. (d) Photoemission intensity plot around W1 (left) and the extracted Fermi arcs (right.) Taken from [22]. 9

2.1 (a) The chiral edge mode arises at the interface between the QHE and the vacuum, a trivial insulator. (b) At the same interface, the gap between the valence and conduction bands closes, leading to an edge state. Taken from [34]. 17

2.2 (a) The states at $\Gamma_a = 0$ and $\Gamma_b = \pi/a$ connect pairwise, and the bands intersect the Fermi level (FL) an even number of times. (b) The bands intersect the FL an odd number of times and cannot be eliminated. Shaded bands correspond to bulk bands, while the lines indicate edge states. Taken from [34]. 19

2.3 The counter-propagating edge states of the spin Hall insulator. Taken from [34]. 20

2.4 (a) A schematic of a Dirac cone in the surface of a strong 3D TI. (b),(c) Fermi loops in the surface BZ for E_{F1} (b), and E_{F2} (c). Arrows indicate spin chirality. Taken from [41]. 21

2.5 (a) Fermi arcs connect two Weyl nodes of opposite chirality. (b) Fermi arcs observed through ARPES measurements in the monophosphide family of Weyl semimetals. Taken from [48]. 23

2.6 Type-II Weyl nodes. Electron and hole pockets touch at Weyl nodes. Taken from [45]. 24

2.7 Origin of the chiral anomaly. Adapted from [45]. 26

2.8 Example band structure of a Kramers-Weyl semimetal in the absence (a) and presence of SOC (b). Adapted from [50]. 27

2.9 (a) An example two-sublattice collinear AFM state. (b) Spin-flop state. (c) Above a critical magnetic field it becomes energetically favorable for the system to switch into the spin-flop phase. Adapted from [51]. 29

3.1 (a) A glovebox filled with Ar gas where most of the materials are kept. (b) The apparatus for evacuating and sealing quartz tubes. Tubes are connected to a pumping line, evacuated, and sealed off using a blow torch. (c) Sealed quartz tubes, with the starting materials held inside the Al_2O_3 crucibles. (d) Box furnaces that can reach 1100^oC. 38

3.2 Pictures of single crystals grown using the flux method, against a 1mm scale. (a) CaCdGe, (b) CuMnAs, (c) $NbGe_2$. 39

4.1 Binary phase diagram for Ca-Cd (a) and Ge-Cd (b). Taken from [83, 84]. 46

4.2 The powder x-ray diffraction patterns of CaCdGe and CaAgAs. The ticks below each pattern indicate the Bragg peak positions determined by the respective crystal structure. Some very small impurity peaks are detected in both patterns; in CaAgAs this corresponds to AgAs, and in CaCdGe it is due to Cd. 46

4.3 (a) Crystal structure of CaAgAs and CaCdGe. The TX_4 octahedra are shown in blue and the Ca atoms are shown in green. (b) and (c) Mirror symmetry protected nodal-lines in CaAgAs and CaCdGe. (b) Schematic of a band structure diagram for the nodal-line feature in CaAgAs and CaCdGe. The conduction and valence bands consist of the Ag(Cd) 4d and As(Ge) 4p orbitals, respectively. The band crossings near the Γ point are protected because the two bands have opposite mirror eigenvalues. (c) and (d) First-principles calculated band structures of CaAgAs near the Γ point without SOC (c) and with SOC. (e) Wilson loop calculation of the SOC band structure on the $k_z = 0$ and $k_z = \pi/2$ planes. . . . 48

4.4 (a) Temperature dependence of the electrical resistivity ρ_{xx} for CaCdGe and CaAgAs at $B = 0$ T with $I//c$. (b) MR of CaCdGe and CaAgAs single crystals at T = 2 K with $I//c$ and $B \perp ac$. 49

4.5 CaAgAs single crystal with $I//c$ and $B \perp ac$: (a) Hall resistivity ρ_{yx}. (b) Field dependent transverse MR. (c) Temperature dependent carrier density and mobility. 50

4.6 CaCdGe single crystal S3 with $I//c$ and $B \perp ac$: (a) transverse magnetoresistivity ρ_{xx}. (b) Hall resistivity ρ_{yx}. The symbols correspond to experimental data, while the lines are the curves obtained from the two band model fitting. (c) Temperature dependent carrier densities. (d) Temperature dependent mobilities. 51

4.7 (a) The oscillations in $\delta\rho_{xx}$ are periodic in 1/B and their amplitude decays as the temperature is lowered. Inset: Measurement configuration. (b) Temperature dependence of the normalized amplitude of the oscillations denoted as A/A(2K). Inset: FFT spectrum of the oscillations for a few representative temperatures. The magnetic field was perpendicular to the *ac* plane. (c) 1/B dependence of the quantity $ln(\delta\rho_{xx}/4\rho_0 R_T)$ with a fit to extract the Dingle temperature. (d) The LK fit of the 3 K data. Black dots indicate data points and the green dashed line corresponds to the fit. 54

4.8 (a) and (b) Angular dependence of the experimental F_a^{SdH} (yellow lines; see text) and the calculated F_β^{DFT} (black lines; see text) with the measurement geometries in the insets. (c) and (d) The electronic band structure of CaCdGe with SOC: (c) using the LDA/GGA potential and (d) using the MBJ potential. (e) The Fermi pockets associated with (d). 56

4.9 ARPES measurements and DFT calculations of the band dispersion along high symmetry directions. The red arrows indicate the lower part of the topological surface states. (a) - (c) ARPES momentum-energy maps along (a) Γ-A, (b) Γ - M, and (c) Γ-K. (d)-(f) DFT-derived angle-resolved density of states along (d) Γ-A, (e) Γ - M, and (f) Γ-K. The bright curves indicate topological surface states and the yellow dashed line shows the approximate Fermi level position that agrees with the ARPES data. (g) The DFT calculated band structure of CaAgAs with SOC. The inset shows the detail of the band dispersion along Γ - M near the nodal point. The nodal line around the Γ point is gapped out under SOC, resulting in a topological insulator with $\Delta = 73$ meV. Adapted from [2]. 59

5.1 (a),(b) Crystal structure of ORT CuMnAs. (a) $CuAs_4$ (orange) and $MnAs_4$ (blue) tetrahedral building blocks. (b) The distorted Mn honeycomb lattice (Mn in blue). (c) Powder x-ray diffraction patterns of ORT (pulverized single crystals from batch A) and TET (from powder synthesis) phases. Ticks indicate the Bragg peak positions. Inset: A picture of an ORT single crystal against a mm sized grid. The as-grown surface is the bc plane. 62

5.2 Taken from [101]. (a) The crystal structure of the orthorhombic CuMnAs(P), with red arrows showing the orientations of the magnetic moments of the Mn atoms. (b) The Brillouin zone of CuMnAs(P) and its projection on the (010) surface. (c) Illustration of the screw rotation symmetry S_{2z}. The red dashed line corresponds to the rotation axis, and the yellow circle corresponds to the Mn atom that the orange arrrow is pointing at, after the rotation about the z axis (C_{2z}) and a half translation along the (101) direction (τ=(1/2,0,1/2)). (d) The electronic structure of CuMnAs along high-symmetry lines in the presence (blue) and absence (red) of SOC. The magnetic moments of the Mn atoms are predicted to be along the z direction. The insets (yellow boxes) show the details of the band crossings near the Fermi level, which has been set to zero. 64

5.3 PA: (a) Normalized resistivity ρ(T)/ρ(400 K) and its derivative dρ/dT vs T .Inset: Hall resistivity ρ_{yx} vs T. PB [(b)–(d)] (b) Normalized resistivity ρ(T)/ρ(400 K) and dρ/dT vs T.(c) Susceptibility M/H and d(M/H)/dT vs T.(d) Heat capacity C_p vs T.Inset: C_p/T vs T^2. 69

5.4 (a) The (1,1,0) intensity vs ω for PA. (b) A comparison between the (1,1,0) peak intensity and the dρ/dT vs T. The red line corresponds to the power-law fit. (c) Magnetic structure of PA in the CAFM state. Only the Mn sublattice is shown. (d) The view of the magnetic structure from the b direction. Mn atoms are shown in blue. "+" denotes spins pointing out of plane while "-" denotes spin pointing in plane. 72

5.5 (a),(b) Intensity vs ω for PB. The black arrows indicate the trend of the peak intensity with decreasing temperature. (c) A cut of the neutron scattering in the $hk0$ plane. (d) A comparison between the (0.9,1,0) peak intensity and dρ/dT vs T . The light blue box marks the temperature region where CAFM and ICAFM compete and coexist. 73

5.6 (a) Calculated band structures of the ORT CuMnAs with SOC and the magnetic structure shown in Figure 5.4 (c). The inset shows the Brillouin zone and its projection to the (010) surface. Δ is the band gap of a massive topological fermion along ΓX line. (b) The detail of the band structure marked by the yellow box in (a). (c) Fermi-surface contour on the (010) surface at the calculated Fermi level. Corresponding electronic spectra along (d) $\bar{k}_x = \pi$/a and (e) $\bar{k}_z = 0$. The Fermi level is set to zero. 75

5.7 Temperature dependence of the susceptibility χ of $Cu_{0.95}MnAs$ with a magnetic field of 1 T, applied parallel to the a, b and c axes. Inset: The derivative of the quantity χ T with respect to temperature. The dashed lines indicate the transition temperatures. 76

5.8 (a) The magnetization, M, of $Cu_{0.95}MnAs$ at several temperatures for H // b. (b) The magnetoresistance, MR, of $Cu_{0.95}MnAs$ at several temperatures, for H // b and I // b. Inset: The MR for for fields up to 35 T. (c)-(d) The derivatives of M and MR with respect to H. The dashed lines go through the peaks of the derivatives, which is the criterion we used to determine the transition temperatures. 78

5.9 (a) The field dependence of the magnetization of $Cu_{0.95}MnAs$ for 2 K, 20 K, 40 K and 60 K with the field parallel to a. (b) The field dependence of the magnetization of $Cu_{0.95}MnAs$ for 2 K and 40 K with the field parallel to c. . . . 79

5.10 The magnetic phase diagram of $Cu_{0.95}MnAs$ with the field parallel to the b axis. 80

5.11 (a)-(b) The isothermal magnetization (a) and magnetoresistance (b) of $Cu_{0.98}Mn_{0.96}As$ for certain temperature values. The magnetic field was applied parallel to the b axis. 81

6.1 (a) The binary phase diagram of Nb-Ge. Taken from [125]. (b) A picture of the vertical tube furnace used for the synthesis of $NbGe_2$. Arrows indicate Ar flow, and the cylinder indicates the approximate location of the Ta tube. 84

6.2 The x-ray powder diffraction pattern of $NbGe_2$, with indexed peaks. The peaks with asterisks are due to impurities, most likely due to Ge flux. The crystal structure and a picture of a single crystal against a mm background are shown as insets. 85

6.3 The resistivity of a $NbGe_2$ single crystal at 0 T. Inset: zoomed-in plot of the superconducting transition. 87

6.4 (a) The contour plot of the FFT frequencies as a function of angle. Three frequency branches can be distinguished, labeled α, α' and β. Strong spin splitting is observed for α and α'. The black dots correspond to the DFT calculated frequencies. The inset shows the measurement geometry. (b) The orbital-resolved electronic band structure of bulk $NbGe_2$ with SOC. The blue and red dots indicate Nb-4*d* orbitals and Ge-4*p* orbitals, respectively. The red arrows denote the positions of Weyl points. (c) The Fermi surfaces in the full BZ of $NbGe_2$. The first three panels show hole like pockets and the last panel an electron pocket. The extremal cross sections with oscillation frequencies less than 500 T are labeled A, A′, B, C and C′. From a comparison of dHvA and DFT, it is clear that the α, α' and β branches correspond to A, A′ and B, respectively. 88

6.5 F_β branch: (a) $\Delta\tau$, obtained after subtracting a polynomial background, as a function of 1/B for temperatures up to 3.2 K. (b) The FFT plot of $\Delta\tau$, revealing $F_\beta = 257$ T at this angle. (c) A fit of the amplitude at a fixed magnetic field of 8.8 T to obtain the effective mass associated with the orbit. (d) Data at 1.8 K (black line) with LK fit (red line). 90

6.6 (a) The FFT spectrum of the oscillations obtained with the magnetic field at an angle of $\approx 60^o$ with respect to the [011] axis. (b) Fit of the temperature dependence of the FFT amplitude to determine the effective masses. (c)-(e) $\Delta\tau$ (black line) with the LK fit with two frequencies shown in red. For both frequencies, (c) ϕ_i and T_D are all free parameters; (d) T_D are free parameters and ϕ_i are set to be equal; (e) ϕ_i are free parameters and T_D are set to be equal. 91

6.7 (a) and (b) MR at several temperatures. (c) Hall resistivity at various temperatures. (d) The calculated MR at 20 K and 100 K with offset. The calculation was done by solving the Boltzmann transport equation within the relaxation time approximation. 94

6.8 (a) A comparison of the electronic part of the specific heat $C_{el}/\gamma_n T_c$ to the predictions of the BCS model. Inset: C_p/T as a function of T^2, with the fit to $C_p/T = \gamma + \beta T^2$ and the derived parameters shown as an inset. (b) $M - H$ loop at 0.5 K. (c) Specific heat with $H\|[111]$ direction at various fields. The criterion inferring T_c is shown. (d) Magnetic isotherms with $H \perp [111]$ at several temperatures. The criterion inferring T_c is shown. (e) Resistivity under various fields with $H\|[011]$. The criterion inferring T_c is shown. (f) $H - T$ phase diagram, with values determined from specific heat, magnetic susceptibility and resistivity measurements. The purple line corresponds to a fit to the expression $H_c(T) = H_c(0)[1 - (T/T_c)^2]$. 96

6.9 The electron-phonon coupling weighted phonon band structure of $NbGe_2$. The size and color of each marker denotes the mode and wave-vector resolved electron-phonon coupling. The colorbar denotes the value of the electron-phonon coupling. 99

A.1 The temperature dependent resistance for pieces selected from batch A. 103

A.2 The temperature dependent resistance for pieces selected from batch B. 104

A.3 The temperature dependent resistance for pieces selected from batch C. 104

A.4 The temperature dependent resistance for pieces selected from batch D. 105

A.5 The temperature dependent resistance for pieces selected from batch E. 105

List of Tables

5.1 Synthesis details of Cu_xMn_yAs single crystals 66

5.2 Single crystal crystallographic data of PA and PB in the ORT *Pnma* space group at 300 K. 67

5.3 Atomic coordinates and equivalent isotropic displacement parameters of PA and PB at 300 K. U_{eq} is defined as 1/3 of the trace of the orthogonalized U_{ij} tensor ($Å^2$) and SOF stands for site occupancy factor. 67

6.1 Effective masses, Dingle temperatures, quantum lifetimes and mobilities, and ϕ_i Berry phases for pockets α, α' and β summarized from Figures 6.6 and 6.5. . . . 93

Acknowledgements

Completing this dissertation has been a long and difficult journey and I am grateful for the support and help of many people who helped me finish it.

It has been a privilege to work with Dr. Ni Ni. Her continuous support, encouragement and motivation have kept me going all these years. I would not have been able to finish this dissertation had it not been for her mentoring and all of her "You can do it!"'s.

Thanks must also go to previous and current members of the Ni lab who have always been there to lend a hand when things got hard and helped me become a better experimentalist. The contributions of our many collaborators must also be mentioned here. Their work complemented the work done in the Ni lab and helped us improve our understanding of the physics of our materials, and I am incredibly grateful for all their help. Chapter 4 is based on [1] and [2]. G. Kotliar's group, T.-R. Chang and S.-Y. Xu performed theoretical calculations for us, while ARPES experiments were carried out by C. Liu's group. Chapter 5 is based on [3] and [4]. H. Cao helped us with neutron diffraction measurements and W. Xie's group with single crystal X-ray diffraction. S.-C. Zhang's group performed theoretical calculations, and D. Graf helped us with high magnetic field measurements. Chapter 7 is based on [5]. T.-R. Chang's group performed the theoretical analysis. The work at the Ni lab was performed with support from the US Department of Energy (DOE) and the National Science Foundation (NSF).

My time at UCLA would not have been the same without the people I met there. My classmates and I survived our first year of classes together, studied countless hours for and celebrated passing the comp. Although I did not keep in touch with many of them, I will always cherish these memories.

Many thanks must also go to my parents who encouraged me from a young age to do well in school. My early education played a huge role in my later success, and I have them to thank for pushing me to do my best.

Attending grad school at UCLA has been a life-changing experience. I would not have been able to complete my application if it hadn't been for my friend Evripidis' help. We spent countless hours together proofreading essays and emails, and you were always there to remind me that I should believe in myself. This dissertation is dedicated to you.

Lastly, this journey would not have been the same without Seth's love and support. Thank you for all the times you made me laugh when I was having a difficult day and for not letting me give up when I thought what I was trying to do was impossible.

Curriculum Vitae

March 2013 B.S. in Physics, Aristotle University of Thessaloniki

Publications

[1] Eve Emmanouilidou, Bing Shen, Xiaoyu Deng, Tay-Rong Chang, Aoshuang Shi, Gabriel Kotliar, Su-Yang Xu, and Ni Ni. Magnetotransport properties of the single-crystalline nodal-line semimetal candidates $CaTX(T = \mathrm{Ag}, \mathrm{Cd}; X = \mathrm{As}, \mathrm{Ge})$. *Physical Review B*, 95:245113, Jun 2017.

[2] Eve Emmanouilidou, Huibo Cao, Peizhe Tang, Xin Gui, Chaowei Hu, Bing Shen, Junyi Wu, Shou-Cheng Zhang, Weiwei Xie, and Ni Ni. Magnetic order induces symmetry breaking in the single-crystalline orthorhombic CuMnAs semimetal. *Physical Review B*, 96:224405, Dec 2017.

[3] Eve Emmanouilidou, Jinyu Liu, David Graf, Huibo Cao, and Ni Ni. Spin-flop phase transition in the orthorhombic antiferromagnetic topological semimetal $Cu_{0.95}MnAs$. *Journal of Magnetism and Magnetic Materials*, 469:570 – 573, 2019.

[4] Eve Emmanouilidou, Sougata Mardanya, Jie Xing, P. V. Sreenivasa Reddy, Amit Agarwa, Tay-Rong Chang, and Ni Ni. Fermiology and Type-I superconductivity in the chiral superconductor $NbGe_2$ with Kramers-Weyl Fermions. *Physical Review B*, under review (2020)

[5] Matthew Pelliccione, Alec Jenkins, Preeti Ovartchaiyapong, Christopher Reetz, Eve Emmanouilidou, Ni Ni, and Ania C Bleszynski Jayich. Scanned probe imaging of nanoscale magnetism at cryogenic temperatures with a single-spin quantum sensor. *Nature Nanotechnology*, 11(8):700–705, 2016.

[6] Xiao-Bo Wang, Xiao-Ming Ma, Eve Emmanouilidou, Bing Shen, Chia-Hsiu Hsu, Chun-Sheng Zhou, Yi Zuo, Rong-Rong Song, Su-Yang Xu, Gan Wang, et al. Topological surface electronic states in candidate nodal-line semimetal CaAgAs. *Physical Review B*, 96(16):161112, 2017.

[7] Bing Shen, Eve Emmanouilidou, Xiaoyu Deng, Alix McCollam, Jie Xing, Gabriel Kotliar, Amalia I Coldea, and Ni Ni. Significant change in the electronic behavior associated with structural distortions in monocrystalline $SrAg_4As_2$. *Physical Review B*, 98(23):235130, 2018.

[8] Xiaoqing Zhou, Qihang Liu, QuanSheng Wu, Tom Nummy, Haoxiang Li, Justin Griffith, Stephen Parham, Justin Waugh, Eve Emmanouilidou, Bing Shen, et al. Coexistence of tunable Weyl points and topological nodal lines in ternary transition-metal telluride $TaIrTe_4$. *Physical Review B*, 97(24):241102, 2018.

[9] Shu Cai, Eve Emmanouilidou, Jing Guo, Xiaodong Li, Yanchun Li, Ke Yang, Aiguo Li, Qi Wu, Ni Ni, and Liling Sun. Observation of superconductivity in the pressurized Weyl-semimetal candidate $TaIrTe_4$. *Physical Review B*, 99(2):020503, 2019.

[10] Jinyu Liu, Pengfei Liu, Kyle Gordon, Eve Emmanouilidou, Jie Xing, David Graf, Bryan C Chakoumakos, Yan Wu, Huibo Cao, Dan Dessau, et al. Nontrivial topology in the layered dirac nodal-line semimetal candidate $SrZnSb_2$ with distorted Sb square nets. *Physical Review B*, 100(19):195123, 2019.

[11] Bing Shen, Chaowei Hu, Huibo Cao, Xin Gui, Eve Emmanouilidou, Weiwei Xie, and Ni Ni. Structural distortion and incommensurate noncollinear magnetism in $EuAg_4As_2$. *Physical Review Materials*, 4(6):064419, 2020.

[12] Jie Xing, Erxi Feng, Yaohua Liu, Eve Emmanouilidou, Chaowei Hu, Jinyu Liu, David Graf, Arthur P Ramirez, Gang Chen, Huibo Cao, et al. Néel-type antiferromagnetic order and magnetic field–temperature phase diagram in the spin-1/2 rare-earth honeycomb compound $YbCl_3$. *Physical Review B*, 102(1):014427, 2020.

CHAPTER 1

Background and history of three-dimensional topological materials

The discovery of topological insulators started a new era for the field of condensed matter physics by drawing interest to the idea of a new type of classification of matter that went beyond the concept of symmetry breaking. Prior to that, physicists classified the different states of matter according to the symmetries they broke. For instance, the transition from the gaseous phase to a solid can be thought of as breaking translational invariance; magnets break time-reversal symmetry and superconductors break gauge symmetry. Not all distinct phases of matter can be classified in terms of spontaneous symmetry breaking however and this became apparent with the integer quantum Hall effect (IQHE), which defied such an explanation and needed the concept of topology in order to be understood. Its experimental observation and theoretical understanding took place in the 1980s, but interest in topological order was rekindled much later with the discovery of topological insulators, which spurred a flurry of interest in this field and led to the subsequent prediction and experimental realization of several other materials with topological order and novel properties, that are important not only for advancing our understanding of condensed matter physics, but also for technological applications. In this chapter I will give an overview of the discoveries of these topological phases of matter in a chronological order, and discuss the most notable materials and their experimental signatures.

Topology is a field of mathematics concerned with the study of geometrical properties of objects that remain unchanged under continuous deformations such as stretching or bending. Imagine how a coffee cup can be continuously deformed into a donut, without breaking or

cutting it. These two objects are said to be topologically equivalent, and they can be identified by their number of holes, which is known as the genus. Surfaces with different genuses cannot be continuously deformed into one another, and are topologically inequivalent. In condensed matter systems, the role of the genus is played by the topological invariant, which is essentially an integral over the band structure. Materials where this integral vanishes are topologically trivial, whereas those with a non-zero topological invariant are characterized by measurable physical properties that arise precisely from their non-trivial topology.

Nonmagnetic topological insulators (TIs) were predicted when it was realized that arguments for the topological characterization of the quantum spin Hall state, the "cousin" of the integer quantum Hall state that exhibits quantized spin Hall conductance and vanishing charge Hall conductance, can be extended to 3D materials [6–8]. Topological surface states that are protected from gapping out by time reversal $\mathcal{T}$ symmetry were also predicted as a result of topological order [6], while band inversion is a necessary condition for the emergence of these surface states. The first 3D TI was experimentally discovered in the thermoelectric semiconducting alloy $Bi_{0.9}Sb_{0.1}$ using angle resolved photoemission spectroscopy (ARPES). [9] This material however had a small band gap and complicated surface structure, and this motivated the search for candidates with simpler surface structure. Not long after the discovery of $Bi_{0.9}Sb_{0.1}$ as a TI, Bi_2Se_3 and Bi_2Te_3 were experimentally confirmed to be 3D TIs. What motivated this search was the fact that, while in $Bi_{0.9}Sb_{0.1}$ the topological order originates from bulk band-inversions at the three equivalent L points, in Bi_2Se_3 only one band is inverted, so a simpler surface state is expected. Bi_2Se_3 has a rhombohedral crystal structure and a hexagonal Brillouin zone (BZ), as shown in Figure 1.1(d). Figure 1.1 (a)-(b) show clear 'V' shaped bands approaching the Fermi level along the $\bar{\Gamma}$ - $\bar{M}$ and $\bar{\Gamma}$ - $\bar{K}$ momentum lines. A comparison with the theoretically predicted band structure showed that the V band was a surface Dirac cone enclosing a Kramer's point (Γ). Because of its simple topological surface spectrum, Bi_2Se_3 was termed the "hydrogen atom" of strong TIs.

The use of spin-resolved ARPES allowed the observation of spin-momentum locking, a

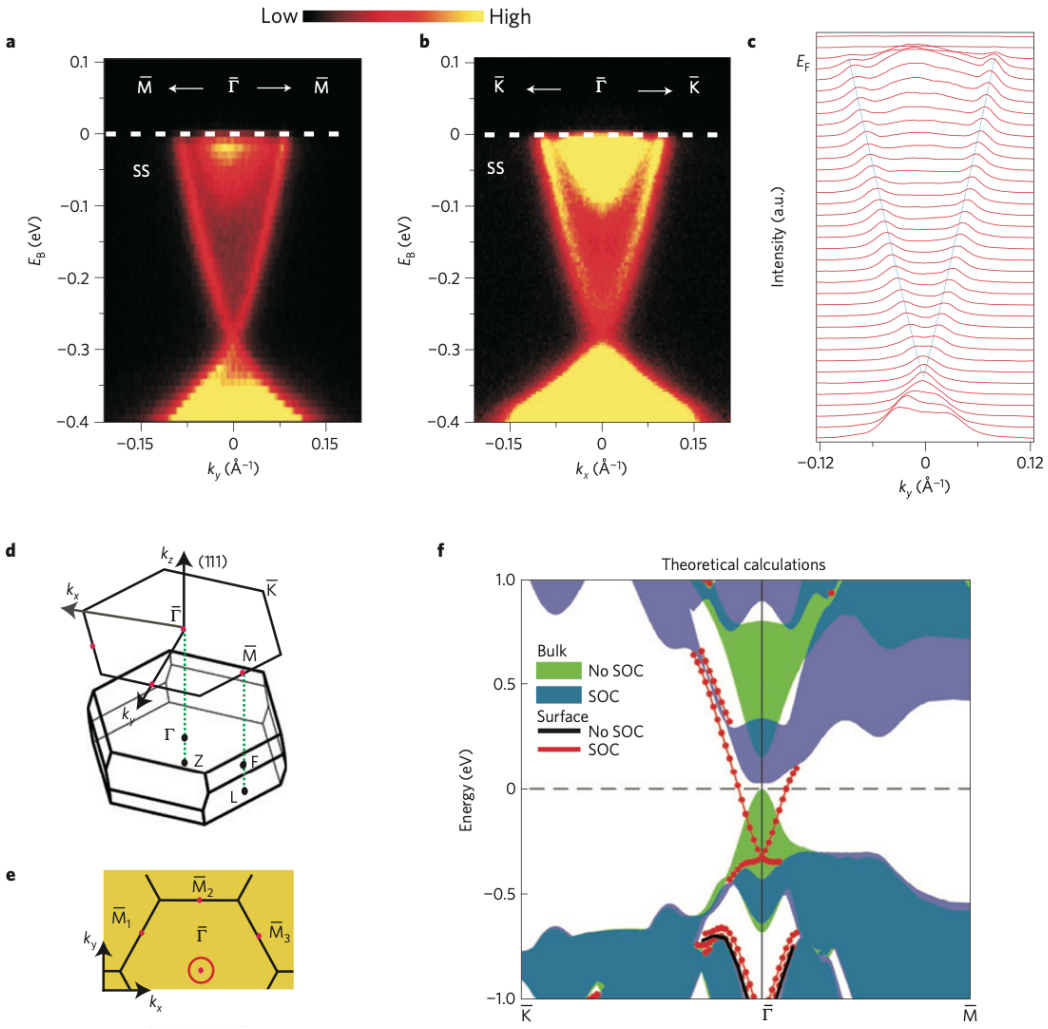

Figure 1.1: (a),(b) Surface electronic band dispersion in Bi_2Se_3 along the $\bar{\Gamma}$ - $\bar{M}$ and $\bar{\Gamma}$ - $\bar{K}$ momentum-space cuts. (c) The momentum distribution curves from (a) show that two surface bands converge at a single Dirac point at $\bar{\Gamma}$. (d) The 3D BZ and its projection on the (111) plane. (e) The Fermi surface (FS) of the 2D surface states is a circle around Γ if the chemical potential lies inside the band gap. (f) Theoretically calculated electronic structure of the (111) surface in the presence and absence of SOC. Simply degenerate surface bands that cross the Fermi level appear only when SOC is included in the calculations. Taken from [10].

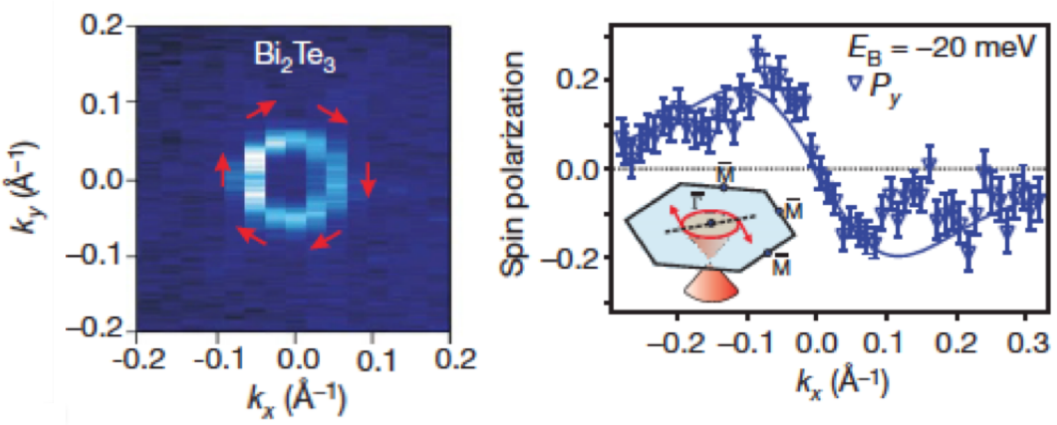

Figure 1.2: Spin momentum locking in Bi_2Te_3 using spin-resolved ARPES. Taken from [11].

key signature of topological order in TIs. Bi_2Te_3 was a better candidate than Bi_2Se_3 for this purpose because in Bi_2Se_3 there is an additional component to the density of states around the Γ point due to the degenerate bulk conduction band. Figure 1.2 shows the ARPES intensity map at the chemical potential of the (111) surface with red arrows indicating the direction of the spin projection around the Fermi surface. As shown on the right panel, photoelectrons emmitted along the k_x cut are spin-polarized along the y-direction. Electrons of opposite momentum have polarization signals of equal magnitude and opposite spin, indicating that there is one-to-one correspondence between spin and momentum that is due to the topology of Bi_2Te_3.

The discoveries of 3D TIs were soon followed by the prediction and experimental observation of nonmagnetic topological semimetals, such as Cd_3As_2, Na_3Bi and $ZrTe_5$. These are materials that respect both $\mathcal{T}$ and space inversion $\mathcal{I}$ symmetries. A finite amount of SOC lifts the degeneracy of any bands that cross due to band-inversion, however the presence of additional symmetries can protect some band crossings from opening up. In Cd_3As_2, this role is played by the C_4 rotational symmetry, which ensures the existence of two band touching points with low energy excitations that can be described by the Dirac equation for massless particles [12]. Unlike 3D TIs, 3D Dirac semimetals possess bulk Dirac fermions with linear energy dispersions along all three momentum directions.

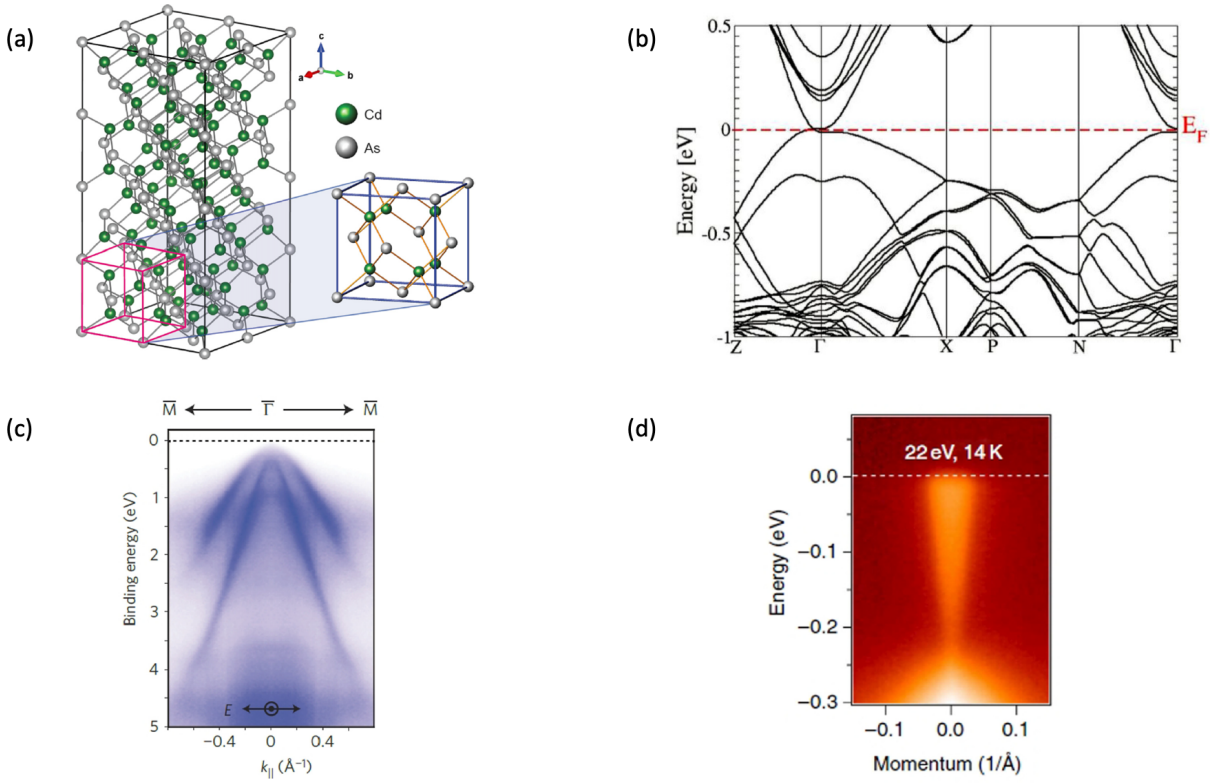

Figure 1.3: (a) The non-primitive tetragonal unit cell of Cd_3As_2, which consists of 160 atoms. (b) The band structure, with 3D Dirac band touching points near the Γ point. (c), (d) The valence (c) and conduction (d) bands near the Γ point mapped using ARPES. Adapted from [13].

Cd_3As_2 has a tetragonal crystal structure with the centrosymmetric space group $I4_1/cd$. Figure 1.3 (a) shows its complex crystal structure, which holds 160 atoms in the unit cell. The band structure is shown in Figure 1.3 (b), with symmetry allowed band crossings near the Γ - Z line. Here too, ARPES measurements continued to be the best suited experimental technique to confirm the electronic structure of these materials. Figure 1.3 (c) shows the band dispersion along the M-Γ-M direction, with a linearly dispersing band seen clearly in addition to another hole type wealy parabolic bulk band. Figure 1.3 (d) shows the dispersion of the conduction band in the direction perpendicular to the Γ-Z line. The shape of these 3D conical bands presented clear evidence for the existence of massless 3D fermions.

The topological character of the surface states in 3D TIs, the linearly dispersing bands and the Fermiology of 3D Dirac semimetals can also be probed by studying the quantum oscillations that can appear in thermodynamic or transport properties. For example, the first transport measurements on Cd_3As_2 were conducted over 40 years ago, and it was shown to have extremely high mobility of unknown origin as well as linear magnetoresistance (MR) [14, 15]. After the discovery of its topological properties, interest in its peculiar transport properties was renewed and, naturally, it was suspected that the presence of Dirac fermions might be responsible for these properties. Studies on the ultrahigh mobility and giant MR came shortly after the confirmation of Dirac fermions in the bulk. Liang et al. [16] observed large, unsaturating MR in all of their samples and interestingly, that only their low mobility samples exhibited a linear MR, while samples with high mobility had an MR $\propto H^{\alpha}$, with α = 2-2.5. The linear MR was observed at fields far below the Landau limit, so it could not be explained as being due to transport at the lowest Landau level, and instead, a mechanism involving charge fluctuations was proposed [16, 17].

The other celebrated 3D Dirac semimetal is Na_3Bi. As discussed previously, the protection of the band touching points with linear dispersions is guaranteed by $\mathcal{T}$, $\mathcal{I}$ as well as additional crystalline symmetries, which in the case of Na_3Bi is a 3-fold rotational symmetry [19]. Its hexagonal crystal structure, with space group $P6_3/mmc$, consists of Na-Bi honeycomb layers stacked along the c axis with Na atoms between these layers. ARPES

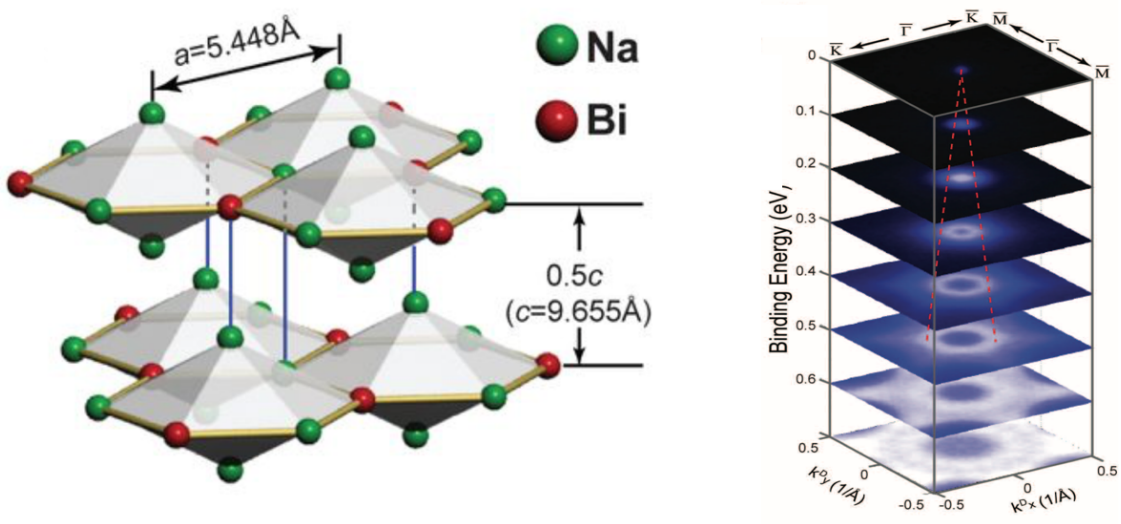

Figure 1.4: The crystal structure and electronic structure of Na_3Bi. Taken from [18].

measurements again confirmed the presence of a Dirac point at Γ, by observing linear energy dispersion. Figure 1.4 shows a plot of constant energy contours at different binding energies, with the red dashes lines added to highlight the conical shape of the energy dispersion [18].

A Dirac point can be split into two with the application of magnetic field which breaks $\mathcal{T}$ symmetry and removes the spin degeneracy of the bands, splitting a Dirac point into two Weyl points of opposite chirality. Such field-induced Weyl nodes have been suggested in Cd_3As_2, Na_3Bi and $ZrTe_5$. Another way that the spin degeneracy can be removed is through the removal of inversion symmetry $\mathcal{I}$. Such a material would be an intrinsic Weyl semimetal. The first nonmagnetic intrinsic Weyl semimetal that was discovered was TaAs. First-principles calculations predicted TaAs, along with other monophosphides, to be Weyl semimetals hosting 12 pairs of Weyl nodes in their Brillouin zone. The existence of Weyl nodes is ensured by the lack of $\mathcal{I}$ symmetry in these noncentrosymmetric compounds [21]. Figure 1.6 (a) shows the crystal structure of TaAs, which crystallizes in a tetragonal crystal structure with space group $I4_1md$, which has no $\mathcal{I}$ summetry. In addition to linear band dispersions near the band touching points, Weyl semimetals are characterized by an additional "smoking gun" signature known as a Fermi arc. Fermi arcs are discontinuous Fermi surfaces that start and end at surface projections of two Weyl nodes with opposite chiral-

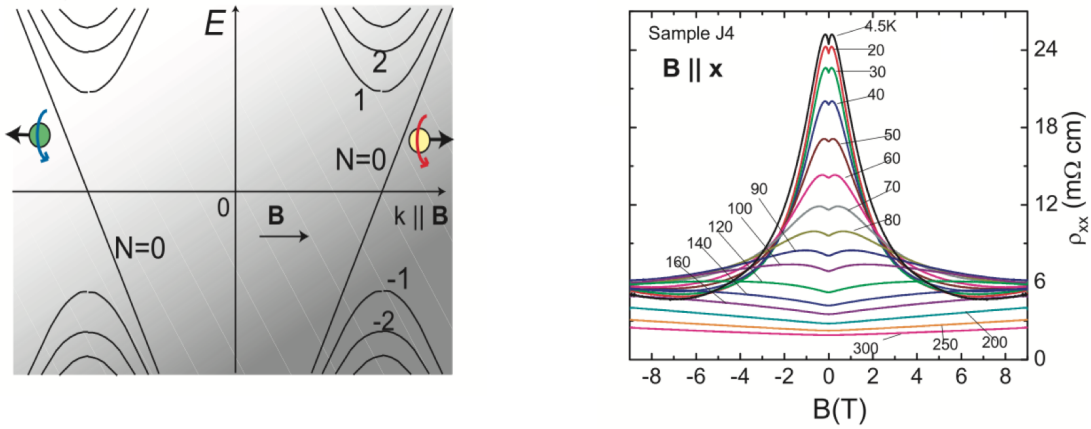

Figure 1.5: NLMR in Na_3Bi due to charge pumping between the two branches of the lowest LL. Taken from [20].

ity. These were disentangled from normal surface states forming Fermi surface pockets and matched to pairs of Weyl nodes with perfect agreement with theoretical calculations [22]. Figure 1.6 (d) shows Fermi surface arcs on the (001) surface of TaAs connecting the Weyl nodes. The topological character of TaAs has also manifested in transport properties and quantum oscillations. At 1.8 K and 9T, TaAs exhibits an extemely high transverse MR that reaches $\approx$ 80,000% due to the electron-hole compensation effect. Additionally, analysis of the Shubnikov de Haas (SdH) oscillations showed strong evidence for the presence of a nontrivial π Berry phase [23].

The existence of pairs of Weyl points with opposite chirality was proposed to give rise to another novel transport property, the negative longitudinal magnetoresistance (NLMR). This occurs when E // B, and is a consequence of the electron tansfer between nodes of opposite chiralities [13]. While the chiral anomaly expected when Dirac points are split into two Weyl points was not unambiguously proven in Cd_3As_2 or the Weyl semimetal TaAs due to the artificial current jetting effect, it was observed in Na_3Bi. Xiong et al. [20] provided strong evidence for the chiral anomaly in this material by detecting a large NLMR. Figure 1.5 shows the lowest Landau level (LL) (N=0) which disperses linearly with k with slopes determined by the chirality $\chi = \pm 1$. When electric and magnetic fields are applied parallel

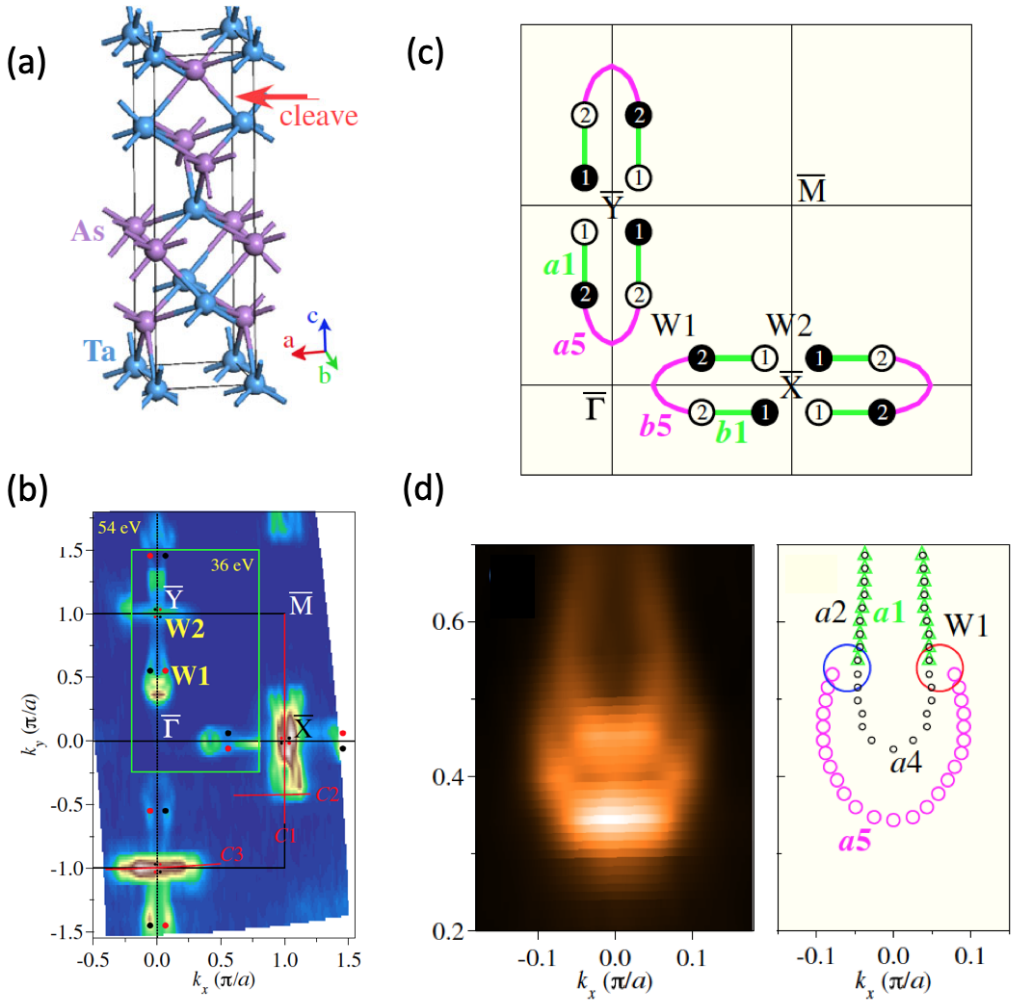

Figure 1.6: (a) The crystal structure of TaAs, with the red arrow indicating where the crystal can be cleaved. (b) The FS on the (001) surface of TaAs, including Fermi arcs as well as trivial Fermi pockets. (c) A schematic of the Fermi arcs connecting W1 and W2 nodes with chiral charges ± 2 and 1 respectively. (d) Photoemission intensity plot around W1 (left) and the extracted Fermi arcs (right.) Taken from [22].

to each other electrons are pumped between the two branches, and this causes the MR to decrease. This observation was further confirmed by an experiment which exaggerated the artificial current jetting effect [24].

The investigation of the interplay between topology, magnetism, electron correlations and charge transport has recently attracted more and more interest due to the successful material realization of magnetic topological materials such as magnetic Weyl semimetals and magnetic topological insulators. In magnetic Weyl semimetals, the presence of Weyl points is ensured by breaking $\mathcal{T}$ symmetry via intrinsic magnetism rather than external magnetic field, as was the case for Nb_3Bi. One important example from this category is $Co_3Sn_2S_2$, where the Berry curvature around the magnetic Weyl nodes gives rise to a giant intrinsic anomalous Hall effect (AHE) [25]. More recently the interplay between magnetism and topology has been manifested in van der Waals materials with the discoveries of intrinsic antiferromagnetic (AFM) and ferromagnetic (FM) topological insulators in the Mn-Bi-Te family of materials [26–28]. Even more exotic materials such as topological superconductors, which can host Majorana particles, have also been predicted [29].

The enormous success of the investigation of the effects of non-trivial topology on physical properties has been largely driven by the material realization of compounds with band structure characteristics such as band inversion, Dirac, and Weyl nodes. However, ideal material realizations with clean band structures where only minimum band crossings exist at the Fermi level are still rare and thus highly desirable. To address this material challenge, my thesis work focuses on the search, design, growth and characterization of the ideal topological material realization. In this dissertation I discuss my work on topological nodal line semimetals, an AFM Dirac semimetal and a topological superconductor. Chapter 4 focuses on CaAgAs, where we show that it is the "hydrogen atom" of nodal line semimetals. In nodal line semimetals, the conduction and valence band cross along a closed curve. Through a comparative study with its "sister" compound CaCdGe we show that the existence of another electron pocket changes the transport properties dramatically. We then elucidate the origin of the usually-observed extremely large magnetoresistance and the debated linear

magnetoresistance in topological semimetals. ARPES measurements performed through a collaboration reveal a topological surface state and a single donut-like Fermi pocket, providing clear evidence that CaAgAs indeed is the "hydrogen atom" of nodal line semimetals. In Chapter 5 I discuss the synthesis and characterization of CuMnAs single crystals, which was predicted to be an AFM 3D Dirac semimetal with clean band structure. I will discuss the synthesis of crystals with slightly different stoichiometries, and the profound effects that these have on the magnetism. Our experimentally determined magnetic structure led to new theoretical predictions about the surface states in this material. The metamagnetic properties of CuMnAs will also be discussed. Chapter 6 focuses on $NbGe_2$, a chiral non-centrosymmetric superconductor predicted to host Kramers-Weyl fermions. I will discuss our results from an analysis of the de Haas-van Alphen oscillations observed in the magnetic torque, namely a complex Fermi surface with pockets characterized by spin-splitting and how it compares to first-principles calculations, as well as our observation of semi-linear magnetoresistance. I will finally discuss our finding that $NbGe_2$ with a full superconducting gap is one of very few binary compounds that are Type-I superconductors and interestingly shows a Type-II to Type-I crossover around 1.5 K.

CHAPTER 2

Overview of nontrivial topology, magnetism, quantum oscillations and superconductivity

The physical properties of a material have long been understood in the framework of the lattice, orbit, spin and charge degrees of freedoms. It was not until the discovery of the quantum Hall effect (QHE) in a two-dimensional (2D) electron gas, where quantized Hall conductance emerged under magnetic fields in the absence of spontaneous symmetry breaking, that the important role of band topology in determining the physical properties of a material was realized. Twenty years later, after the prediction, material realization and observation of 3D TIs, the study of new phases and phenomena caused by non-trivial topology is exploding, making the last decade one of the most active periods in discovering novel emergent phenomena. Band topology has even emerged as a classification principle of the states of matter, with the topological invariant characterizing the topological class of materials. Essential elements in the determination of the band topology are the Berry phase, the Chern invariant and the Z_2 invariant, which will be discussed first in this chapter. Rigorous calculations will not be reproduced here as they are beyond the scope of this dissertation, but elements of these theories will be presented in a simplified manner. Following that, I will discuss the main elements of the theoretical predictions of the topological phases discussed in previous chapters such as topological insulators and the various topological semimetals. Lastly, I will also give an overview of the magnetic phases and transitions characterizing the materials I will discuss in later chapters, the analysis of quantum oscillations and a brief discussion on superconductivity.

2.1 The Berry phase

In his 1983 paper titled "Quantal phase factors accompanying adiabatic changes", Michael Berry argued that the implications of adiabatic change for a quantum mechanical system were incomplete [30]. According to the adiabatic theorem, when the Hamiltonian $\mathcal{H}$ of a system with n eigenstates is altered slowly, the system will remain in the nth eigenstate, and pick up a dynamical phase factor of the form $E_n t/\hbar$ as well as an additional phase of the form $\gamma_n(t)$, known as the geometrical phase factor.

The wavefunction of a system that started in state $\left|n(\vec{R}(0))\right\rangle$ and evolved with $\mathcal{H}$ can be written as

$$|\psi(t)\rangle = exp\left[\frac{-i}{\hbar}\int_0^t dt' E_n(\vec{R}(t'))\right] exp(i\gamma_n(t)) \left|n(\vec{R}(t))\right\rangle \tag{2.1}$$

The geometrical phase factor $\gamma_n(t)$ can be determined by substituting 2.1 into Schrodinger's equation

$$\mathcal{H}(\vec{R}(t)) |\psi(t)\rangle = i\hbar \left|\dot{\psi}(t)\right\rangle \tag{2.2}$$

and leads to

$$\gamma_n = \int_{\mathcal{C}} d\vec{R} \cdot \mathcal{A}_n(\vec{R}) \tag{2.3}$$

where

$$\mathcal{A}_n(\vec{R}) = i\left\langle n(\vec{R})\right| \frac{\partial}{\partial \vec{R}} \left|n(\vec{R})\right\rangle \tag{2.4}$$

$\mathcal{A}_n(\vec{R})$ is known as the Berry connection. The Berry connection is gauge dependent and it was previously believed that one can always choose a suitable gauge such that γ_n can be canceled out, and was thus deemed unimportant.

Berry challenged this conclusion by considering what happens under a cyclic evolution along a closed path $\mathcal{C}$, with $\vec{R}(T) = \vec{R}(0)$. If a gauge transformation of the form

$$\left|n(\vec{R})\right\rangle \rightarrow e^{i\zeta(\vec{R})} \left|n(\vec{R})\right\rangle \tag{2.5}$$

is made, $\rightarrow e^{i\zeta(\vec{R})}$ must be single-valued, meaning that

$$\zeta(\vec{R}(0)) - \zeta(\vec{R}(T)) = 2\pi \times n \tag{2.6}$$

where n is an integer. This shows that for a closed path, γ_n can only change by a factor of 2π, and cannot be removed. It is thus a gauge-invariant quantity given by

$$\gamma_n = \oint_{\mathcal{C}} d\vec{R} \cdot \mathcal{A}_n(\vec{R}) \tag{2.7}$$

In analogy with electrodynamics, we can define the Berry vector potential

$$\vec{\Omega}_n(\vec{R}) = \nabla_{\vec{R}} \times \mathcal{A}_n(\vec{R}) \tag{2.8}$$

and rewrite Equation 2.7 as

$$\gamma_n = \int_{\mathcal{S}} d\vec{S} \cdot \Omega_n(\vec{R}) \tag{2.9}$$

We can now focus on how these concepts apply to crystalline solids, where the parameter space is the band structure. The band structure of a crystal, within the independent electron approximation, is determined by the single electron $\mathcal{H}$

$$\mathcal{H} = \frac{p^2}{2m} + V(\vec{r}) \tag{2.10}$$

V($\vec{r}$) is the periodic potential of the crystal, and according to Bloch's theorem, single

electron wavefunctions can be written as

$$\psi(\vec{r}) = e^{i\vec{k}\cdot\vec{r}} u_{\vec{k}}(\vec{r}) \tag{2.11}$$

where $\vec{k}$ is the crystal momentum and u is a function that satisfies the periodic boundary condition

$$u_{\vec{k}}(\vec{r} + \vec{a}) = u_{\vec{k}}(\vec{r}) \tag{2.12}$$

where $\vec{a}$ is the Bravais lattice vector. If we consider a closed path in $\vec{k}$ space, such as one that can be generated by a magnetic field that induces cyclotron motion, then Bloch states will pick up a Berry phase given by

$$\gamma_n = \oint_{\mathcal{C}} d\vec{k} \cdot \left\langle u_n(\vec{k}) \middle| i\nabla_{\vec{k}} \middle| u_n(\vec{k}) \right\rangle \tag{2.13}$$

Here too we can define the Berry curvature of the bands as

$$\vec{\Omega}_n(\vec{k}) = \nabla_k \times \left\langle u_n(\vec{k}) \middle| i\nabla_{\vec{k}} \middle| u_n(\vec{k}) \right\rangle \tag{2.14}$$

As we can see from Equation 2.14, the Berry curvature is a quantity that depends only on the wavefunction of the material.

To start seeing how a nonzero Berry curvature can appear in physically measurable quantities, we will consider the dynamics of Bloch electrons in an electric field $\vec{E}$ [31]. If we consider a crystal under the perturbation of a weak electric field $\vec{E} = -\nabla V - \frac{\partial \vec{A}}{\partial t}$, the Hamiltonian can be written as

$$\mathcal{H} = \frac{(\vec{p} + e\vec{A})^2}{2m} + V(\vec{r}) \tag{2.15}$$

If we re-define the crystal momentum so that it is gauge invariant

$$\vec{k} = \vec{k} + \frac{e}{\hbar}\vec{A}(t) \tag{2.16}$$

then $\vec{k}$ will satisfy the equation of motion $\dot{\vec{k}} = -\frac{e}{\hbar}\vec{E}$, and it can be shown that [31]

$$\vec{v}_n(\vec{k}) = \frac{\partial \epsilon_n(\vec{k})}{\hbar \partial \vec{k}} - \frac{e}{\hbar}\vec{E} \times \Omega_n(\vec{k}) \tag{2.17}$$

A nonzero Berry curvature must be taken into account for a complete description of electron dynamics. The second term in Equation 2.17 is sometimes called the anomalous Hall velocity, and is what gives rise to what is known as the intrinsic anomalous Hall effect. Interestingly, this expression was derived in the 1950s [32], but it took several years for the connections with the Berry phase to be made.

Although Equation 2.17 shows that the velocity of Bloch electrons is not fully described just by a band dispersion contribution, in many cases the Berry curvature vanishes, and the textbook equation is valid. Specifically, when a crystal respects both $\mathcal{T}$ and $\mathcal{I}$ symmetries, the Berry curvature is equal to zero. If a system breaks either of those symmetries however, then the Berry curvature term must be considered for a complete description of the electron dynamics.

2.2 The quantum Hall effect

The QHE was first observed in the 1980s when Klitzing et al. applied strong magnetic fields to a two-dimensional electron gas and found the Hall conductivity to be quantized in units of $e^2/\hbar$ [33]. Using equation 2.17, one can show that for a 2D insulator, the Hall conductivity can be written as

$$\sigma_{xy} = \frac{e^2}{\hbar} \int_{BZ} \frac{d^2k}{(2\pi)^2} \Omega_{k_x k_y} \tag{2.18}$$

This is an integral of the occupied states over the entire BZ and is an example of what is known as the Chern number. This number is a topological invariant of the system, meaning that it does not change when $\mathcal{H}$ is varied smoothly, and different gapped phases that can be continuousy deformed into one another are said to be topologically equivalent.

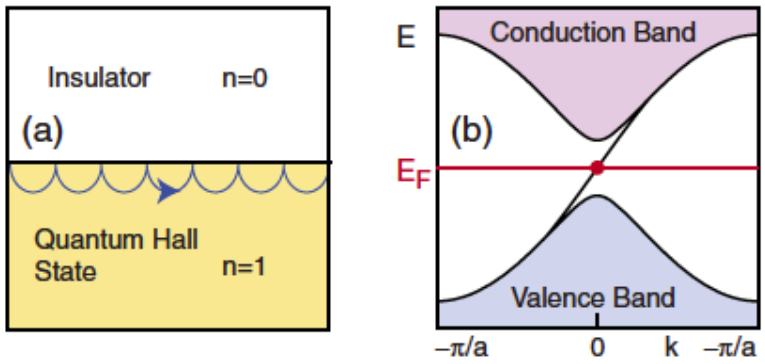

Figure 2.1: (a) The chiral edge mode arises at the interface between the QHE and the vacuum, a trivial insulator. (b) At the same interface, the gap between the valence and conduction bands closes, leading to an edge state. Taken from [34].

The Hall conductivity in the QHE is the Chern number multiplied by the factor $e^2/\hbar$. The phenomenon was first explained by Thouless et al. [35] and we can see that essentially the only condition that is necessary for the Hall conductivity to be quantized is that the Chern number of the bands must be nonzero. Perhaps the most important experimental consequence of topology is the presence of gapless conducting states at the interfaces between systems that are not topologically equivalent. Such edge states are responsible for the quantized Hall conductivity observed in the QHE [36], and we can think of them (semi-classically) as arising from the motion of electrons whose cyclotron orbits bounce off the edge of the material. The edge states also only carry current in one direction and are thus called chiral. The existence of these states is rooted in the topological character of the QHE. At the interface between the QHE and a trivial insulator, such as the vacuum, the energy gap must close, because the two states are characterized by different topological invariants. If $\mathcal{H}$ changes near the surface, the number of edge states can also change as well. However, the difference between right and left moving chiral edge modes is determined by the topology of the system and cannot change. This bulk-boundary correspondence is summarized by [34]

$$N_R - N_L = \Delta n \tag{2.19}$$

where Δn is the difference in Chern numbers across the interface.

2.3 The Z_2 or Quantum Spin Hall insulator

As discussed previously, the QHE is a state that breaks $\mathcal{T}$, and the Chern number requires either $\mathcal{T}$ or $\mathcal{I}$ to be broken. However, a different class of insulators which are topologically distinct from trivial insulators can still exist without breaking $\mathcal{T}$.

$\mathcal{T}$ is defined by the operator

$$\mathcal{T} = e^{i\phi}\sigma_y\Theta \tag{2.20}$$

where Θ is the complex conjugation operator. In classical mechanics, applying $\mathcal{T}$ twice should take a system back to its original state. In quantum mechanics however, and more specifically when we are considering spin 1/2 particles, $\mathcal{T}^2$ = -1 [37]. This has very important consequences which are summarized in Kramers' theorem, and states that, for a system that respects $\mathcal{T}$, all energy levels must be doubly degenerate. This is true for every system with an odd number of fermions. For every eigenstate with energy E, there must be another state with the same energy.

Figure 2.2 shows the electronic states of a $\mathcal{T}$ invariant 2D insulator along k_x, where $\Gamma_a = 0$ and $\Gamma_b = \pi/a$. Generally, Kramer's doublets can occur at different points k and -k. However, at high symmetry points k=0 or k=π/a, -k is just k, so each one of these points are doubly degenerate. The addition of SOC can lift this degeneracy away from high symmetry points, as shown in Figure 2.2, but because energy is a smooth function of k, these energy states must be connected again at Γ_a or Γ_b. There are two ways that this can happen, and they are intimately connected to the topological structure of the material [37].

Figure 2.2 (a) shows two states at Γ_a connected to the same Kramer's doublet at Γ_b. We can see that in this case, depending on where the chemical potential lies, we might have 0, 2 pairs, 4 pairs etc. of edge states. The existence of edge states is not guaranteed in this case, so this would be an example of a trivial insulator. In the case described in Figure 2.2 (b) on

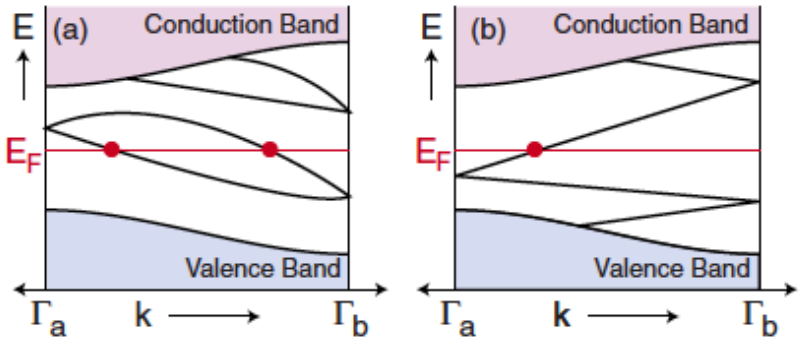

Figure 2.2: (a) The states at $\Gamma_a = 0$ and $\Gamma_b = \pi/a$ connect pairwise, and the bands intersect the Fermi level (FL) an even number of times. (b) The bands intersect the FL an odd number of times and cannot be eliminated. Shaded bands correspond to bulk bands, while the lines indicate edge states. Taken from [34].

the other hand, the states at Γ_a are connected to different Kramer's doublets at Γ_b. In this case, regardless of the location of the chemical potential, there will always be an odd number of edge states crossing it or, more specifically, an odd number of left moving states, with the corresponding number of right moving states. $\mathcal{T}$ invariant 2D insulators can therefore either be trivial, with an even number of edge states, or topological, with an odd number of edge states at the FL. Kane and Mele introduced a new type of topological invariant to describe $\mathcal{T}$ invariant systems, which can take the values $\nu = 0$ (trivial) or 1 (nontrivial) [38]. At the interface between two 2D insulators, the number of edge states intersecting the FL is given by

$$N_K = \Delta\nu \; mod \; 2 \tag{2.21}$$

This state is also known as the quantum spin Hall insulator, and was first predicted to exist in graphene [39] and later in HgTe/CdTe quantum wells [40].

The name spin Hall insulator is a result of the fact that these insulators are characterized by a Hall conductivity of zero, but a finite spin Hall conductivity. We can see this by plotting Figure 2.2 from $-\pi/a$ to π/a, as shown in 2.3 (b). The two edge states that are originating from the Kramer's doublet at k=0, are counter-propagating but have opposite spins.

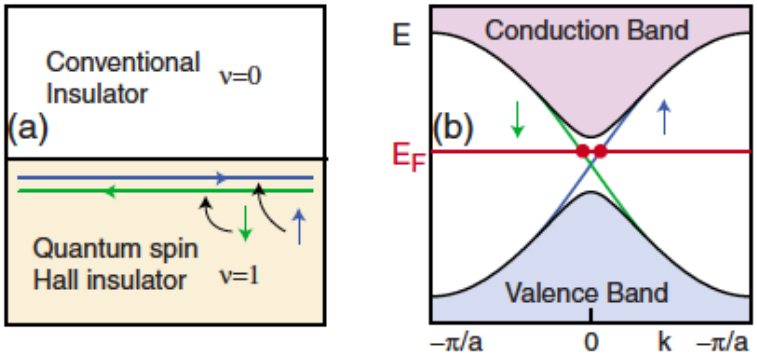

Figure 2.3: The counter-propagating edge states of the spin Hall insulator. Taken from [34].

2.4 3D Topological Insulators

A huge breakthrough in this field was achieved with the prediction that topologically protected states could also be realized in 3D materials. The 3D topological insulators are characterized by topologically protected surface states, rather than edges, and four Z_2 invariants $\nu_0;\nu_1\nu_2\nu_3$. The surface BZ is characterized by four Kramer's points, which are degenerate in the presence of $\mathcal{T}$, but the presence of SOC can lift the degeneracy away from these points.

There are 2 categories of 3D TIs; weak and strong. The main difference between the two is that the first can be regarded as a system of stacked 2D TIs, while the latter cannot. Weak TIs are still considered a somewhat obscure topic, and have eluded clear experimental observation, so they will not be further discussed here.

Strong 3D TIs were experimentally observed soon after they were predicted, and some of those discoveries were discussed in the previous chapter. The Bi_2Se_3 family of materials is characterized by a surface band structure such as the one illustrated in Figure 2.4, with (a) showing the surface band structure in the bulk band gap. The band crossing point(s) occur at Kramers points, and the dispersion is linear in k_x and k_y, hence the name Dirac cone. Figures 2.4 (b) and (c) show the surface Fermi circle depending on where the FL lies. In a strong 3D TI, the surface Fermi circle encloses an odd number of Dirac points. $\mathcal{T}$ requires states at (k_x,k_y) and (-k_x,-k_y) to have opposite spins, and that results in the spin rotating

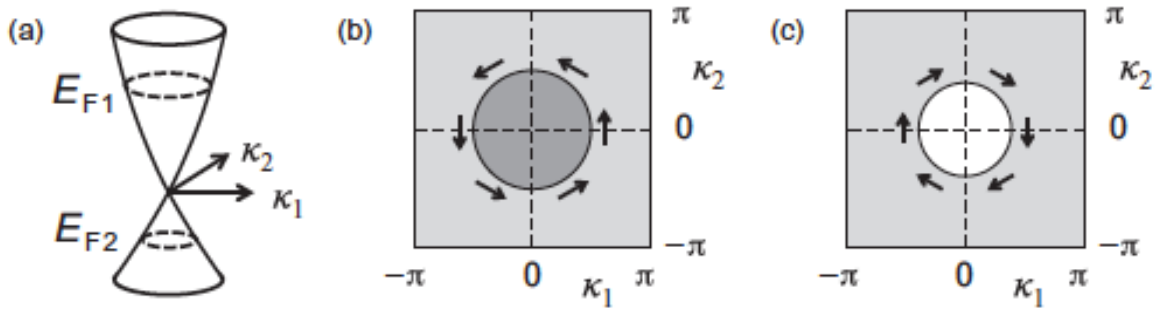

Figure 2.4: (a) A schematic of a Dirac cone in the surface of a strong 3D TI. (b),(c) Fermi loops in the surface BZ for E_{F1} (b), and E_{F2} (c). Arrows indicate spin chirality. Taken from [41].

around the Fermi loop.

It should be noted here that the evaluation of the Z_2 invariants is far from trivial. A huge simplification of the procedure can be made for materials that respect $\mathcal{I}$; the sign of the product of the parities of all occupied bands can be used to distinguish topologically trivial from non-trivial phases [42]. Specifically, trivial insulators always have a positive product of parities, while those with an odd product are non-trivial (even refers to +1 and odd to -1). This simplification led to the search for materials showing band inversion between valence and conduction bands of opposite parity as a result of strong SOC. This is because an inversion between bands of opposite parity will change the sign of the products of the parities, and drive a material that was previously trivial to becoming a topological phase.

It is also possible for surface states to be protected as a result of crystal symmetries [43]. Liang Fu introduced the term "topological crystalline insulator" to describe insulators which cannot be smoothly deformed into the trivial atomic insulator, when $\mathcal{T}$ and certain point group symmetries are preserved. He considered insulators with the $\mathcal{C}_4$ or $\mathcal{C}_6$ rotational symmetries and showed that the (001) surface surface can host gapless surface states that disperse quadratically.

2.5 Topological semimetals; Weyl, Dirac and Nodal-line

The idea that metals can have a topologically nontrivial electronic structure is not new; as early as 2007 it was hypothesized that a topological gapless state could come about as a result of a phase transition between the spin Hall and insulating phases in 3D [44], it wasn't until the discovery of Dirac and Weyl semimetals that topological semimetals emerged at the forefront of quantum materials research.

2.5.1 Weyl semimetals

The defining characteristic of Weyl semimetals is again the existence of band touching points, where two bands are degenerate at particular points in momentum space. We might expect that band touching points are rare or unstable unless they are protected by a symmetry, however, that is not always the case. Consider a material with non-degenerate bands, such as a noncentrosymmetric or magnetic material, and suppose two bands touch at some point $\vec{k}_0$ at energy E_0. The Hamiltonian near that point can be expanded as a Taylor series [45]

$$\mathcal{H}(\vec{k}) = E_0\hat{\sigma}_0 \pm \hbar v_F(\vec{k} - \vec{k_0}) \cdot \hat{\sigma} \tag{2.22}$$

Such a point cannot be removed. Changing E_0 or $\vec{k}_0$ can introduce a mass term which will only change the location of the node, and changing v_F will only change the slope of the dispersion.

If we set $E_0 = 0$, the equation takes a form very similar to that of a Weyl Hamiltonian, which represents massless chiral particles. Hermann Weyl envisioned neutrinos as the particles that would be described by this equation, and almost certainly could not have expected that particles described by his $\mathcal{H}$ would first be observed in solid state systems. These band touching points are named Weyl points or nodes because of this similarity of their band dispersion to the Weyl equation.

The energies of the $\mathcal{H}$ described by Equation 2.22 with $E_0 = 0$ and $\vec{k}_0$ =0 are given by

$$E_{\pm}(\vec{k}) = \pm\hbar v_F\sqrt{k_x^2 + k_y^2 + k_z^2} \tag{2.23}$$

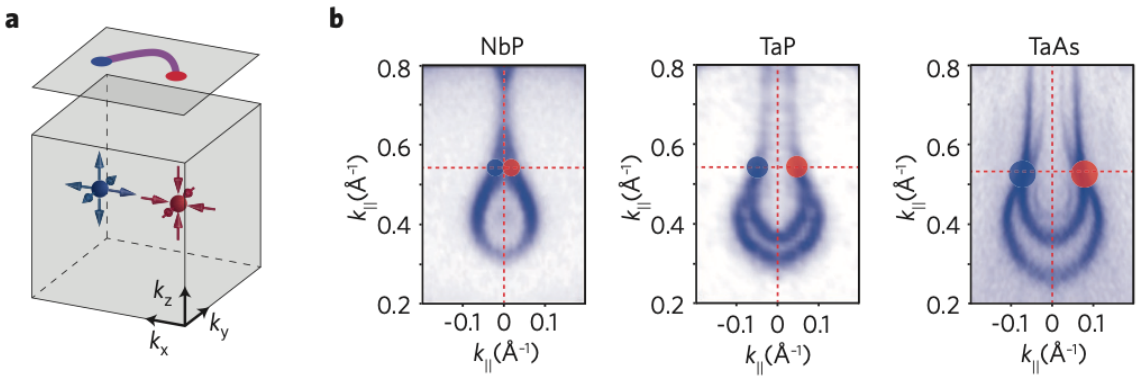

Figure 2.5: (a) Fermi arcs connect two Weyl nodes of opposite chirality. (b) Fermi arcs observed through ARPES measurements in the monophosphide family of Weyl semimetals. Taken from [48].

Recall that because Weyl semimetals break either $\mathcal{T}$ or $\mathcal{I}$, they have a nonzero Berry curvature. The Berry curvature of the $\pm$ band associated with a Weyl node is given by [46]

$$\vec{\Omega}(\vec{k}) = \frac{\chi}{2}\frac{\vec{k}}{k^3} \tag{2.24}$$

Using the analogy between the Berry curvature and electrodynamics, Weyl nodes are often said to act as monopoles, or sources and sinks of Berry curvature, with charge $\frac{\chi}{2}$.

If we consider a system with N Weyl nodes at momentum $\vec{k}_i$ each with chirality χ_i, the net Berry curvature of they system is given by [46]

$$\vec{\Omega}(\vec{k}) = \frac{1}{2}\sum_{i=1}^{N}\chi_i\frac{\vec{k}-\vec{k}_i}{k^3} \tag{2.25}$$

The monopole charge can be found by taking the divergence of the Berry curvature,

$$\int_{BZ} d^3k\nabla_{\vec{k}}\cdot\vec{\Omega}(\vec{k}) = 2\pi\sum_{i=1}^{N}\chi_i\int_{BZ} d^3k\delta(\vec{k}-\vec{k}_i) = 2\pi\sum_{i=1}^{N}\chi_i \tag{2.26}$$

According to the "no-go" theorem [47], this sum must be equal to zero, meaning that Weyl nodes can only exist in pairs of opposite chirality. This has a spectacular experimental consequence, the existence of Fermi arcs.

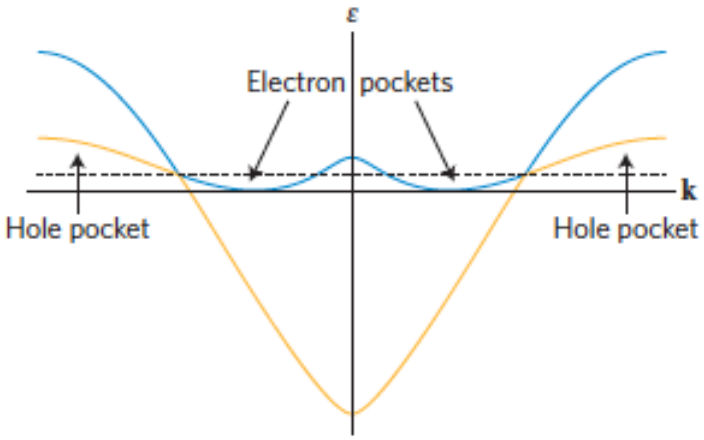

Figure 2.6: Type-II Weyl nodes. Electron and hole pockets touch at Weyl nodes. Taken from [45].

A non-zero Berry curvature means that Weyl semimetals are characterized by a non-zero Chern number, and according to the bulk-boundary correspondence must have protected surface states. These surface states appear on surfaces parallel to a line connecting the Weyl nodes, and are known as Fermi arcs due to their arc-like appearance. Figure 2.5 shows observed Fermi arcs in the monophosphide family of Weyl semimetals.

The reason that Fermi arcs were so clearly observed in these materials is that their Weyl nodes are close to the FL, and additionally, there are few or zero trivial bands near the FL, highlighting the need for clean band structures for the signatures of nontrivial topology to be observed.

Weyl semimetals can be classified as Type-I or Type-II. To discuss this distinction we need to revisit Equation 2.22. If $\vec{k}_0$ is a Kramer's point, then Equation 2.22 applies as written, gives rise to Type-I semimetals. TaAs and the rest of the semimetals in this family are Type-I. If $\vec{k}_0$ on the other hand is away from a Kramer's point, then the coefficient of $\hat{\sigma_0}$ is not a constant, but also has a linear term and $\mathcal{H}$ becomes

$$\mathcal{H} = \hbar\tilde{v}_F(\vec{k} - \vec{k_0}) \cdot \hat{\sigma_0} \pm \hbar v_F(\vec{k} - \vec{k_0}) \cdot \hat{\sigma} \tag{2.27}$$

after setting E_0=0. If $\tilde{v}_F > v_F$, then the Weyl nodes are found at points where the electron

and hole pockets touch [45], as shown in Figure 2.22.

2.5.2 Dirac semimetals

Dirac semimetals are closely related to Weyl, however one important distinction between the two is that the first respect $\mathcal{T}$ and $\mathcal{I}$, and the band touching points, that typically arise from band inversions are protected from gapping out by additional rotational symmetries. Each Dirac node can be thought of as a pair of degenerate Weyl nodes of opposite chiralities χ. Another way that a 3D Dirac semimetal can be realized is by tuning some parameter of $\mathcal{H}$ so as to induce a transition between a topological and a trivial insulator.

In addition to spectroscopic properties, Dirac and Weyl semimetals also exhibit transport properties that provide evidence of their topological character. When a magnetic field is applied in a 3D (semi)metal, the electrons form Landau bands, meaning that they are quantized in the direction that is perpendicular to the field, but disperse in the other momentum directions. In Dirac and Weyl semimetals, when the FL is exactly at the charge neutrality point, the system is in the quantum limit where only the zeroth LL is occupied. The quantum limit is met when the magnetic field is strong enough to push all the LLs ab With the magnetic field applied along the z axis, the Landau levels for Weyl nodes are given by [49]

$$\epsilon_{nk_z} = v_F sgn(n)\sqrt{2\hbar|n|e\left|\vec{B}\right| + (\hbar k_z)^2} \; for \; n \neq 0 \tag{2.28}$$

and

$$\epsilon_{0k_z} = -\chi\hbar v_F k_z \; for \; n = 0 \tag{2.29}$$

The zeroth LL is chiral, and disperses linearly with k_z. If an electric field is applied, only a component that is parallel to the magnetic field can cause electrons to propagate, with an equation of motion

$$\hbar\frac{dk_z}{dt} = -eE_z \tag{2.30}$$

This forces right-handed particles and left-handed anti-particles to be produced, as shown

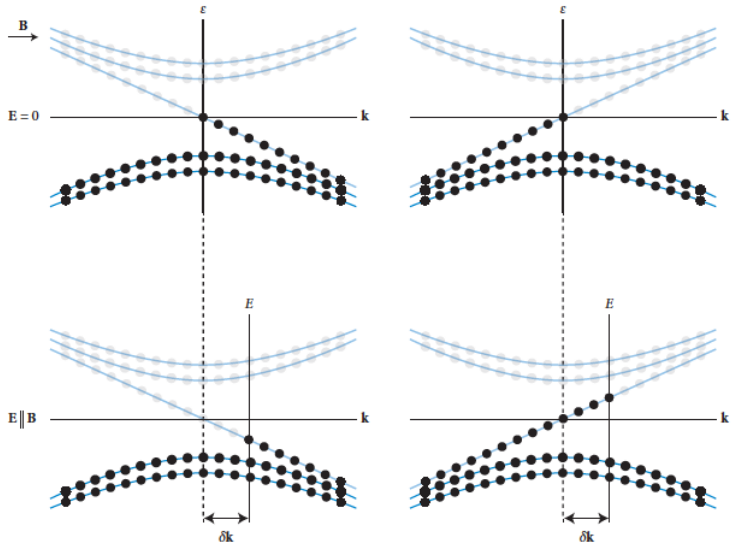

Figure 2.7: Origin of the chiral anomaly. Adapted from [45].

schematically in Figure 2.7 (or vice versa).

In Dirac and Weyl semimetals this phenomenon leads to a negative longitudinal magnetoresistance, while in magnetic Weyl semimetals, which are systems where the $\mathcal{T}$ is broken by the systems intrinsic magnetism, it can lead to an anomalous Hall effect.

2.5.3 Nodal-line and Kramers-Weyl semimetals

Nodal-line semimetals are yet another category of topological semimetals that is characterized by conduction and valence bands crossing at closed loops in momentum space. The bulk Fermi surface of these materials is 1D and the density of states near the nodal touchings is proportional to $|E - E_F|^2$. Additionally, they can be identified by surface states with unique shape, known as "drumhead" surface states.

Although the presence of symmetries has so far been important in guaranteeing the presence of band crossings, chiral crystals present a different case. These materials lack $\mathcal{I}$ or mirror symmetries, and are characterized by band crossings at Kramers points, which are guaranteed by chirality, lattice translation and time-reversal symmetry requirements. In all non-magnetic chiral crystals with SOC, the bands will be split everywhere except at the

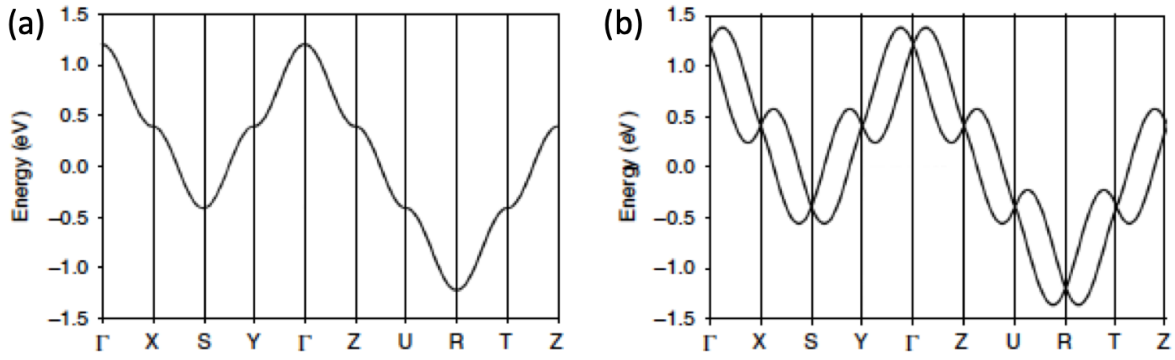

Figure 2.8: Example band structure of a Kramers-Weyl semimetal in the absence (a) and presence of SOC (b). Adapted from [50].

Kramers points, where Kramers theorem requires that the bands remain degenerate. These degeneracies are characterized by a Chern number and carry a chiral charge just as Weyl fermions, and were thus termed Kramers-Weyl fermions [50]. The effect of SOC on the band structure and the degenerate band crossings are illustrated in 2.8.

2.6 Brief overview of common magnetic interactions and structures and metamagnetic transitions

In most solids, magnetism arises due to atoms with incomplete d or f orbitals. In this section I will briefly go over some of the ways that magnetic moments can interact with each other to give rise to long range magnetic order. I will also discuss the origin of metamagnetic transitions, which were observed in some of the materials that will be discussed in later chapters.

Two magnetic moments μ_1 and μ_2 can interact with each other via the magnetic dipolar interaction with energy given by

$$E = \frac{\mu_0}{4\pi r^3}[\vec{\mu_1} \cdot \vec{\mu_2} - \frac{3}{r^2}(\vec{\mu_1} \cdot \vec{r})((\vec{\mu_2} \cdot \vec{r}))] \tag{2.31}$$

This interaction is, however, too weak to account for the observed ordering in magnetic materials, which can be accounted for by the so-called exchange interactions. These interactions

are essentially a result of the exclusion principle for electrons, and the effective Hamiltonian for a large system of atoms is given by

$$\mathcal{H} = -\sum_{ij} J_{ij} \vec{S}_i \cdot \vec{S}_j \tag{2.32}$$

This is known as the Heisenberg model, and J_{ij} is the exchange constant between i^{th} and j^{th} spins. For a system of 2 electrons at $\vec{r}_1$ and $\vec{r}_2$, J is equal to

$$J = \int \psi_1^*(\vec{r}_1)\psi_2^*(\vec{r}_2)\hat{\mathcal{H}}\psi_1^*(\vec{r}_2)\psi_2^*(\vec{r}_1)d\vec{r}_1 d\vec{r}_2 \tag{2.33}$$

The calculation of this integral for a many body system is of course not trivial, but often the observed magnetic structures can be understood by considering J to be a constant for nearest neighbor interactions and 0 otherwise.

The sign of J in 2.32 determines the magnetic ordering. A positive J favors ferromagnetic (FM) ordering, while a negative favors AFM ordering. The simplest AFM case is the collinear one, which can be broken down to two interpenetrating sublattices, where the moments of each sublattice are parallel to each other, but opposite to those of the other sublattice. In more complex cases they can have a noncollinear arrangement, meaning that there is no single spin quantization axis for the entire crystal.

Detailed magnetic structures can only be resolved using neutron scattering. However, the magnetic susceptibility can offer some insight into the overall magnetic ordering in a crystal. The magnetic susceptibility of a system in its paramagnetic state is given by the Curie-Weiss law

$$\chi \propto \frac{1}{T - \Theta} \tag{2.34}$$

If one plots the inverse of the susceptibility, $1/\chi$, as a function of T, the intercept can provide a way to interpret the data. Specifically, if $\Theta = 0$, the material is a paramagnet, if it is positive it orders ferromagnetically, and if it is negative it orders antiferromagnetically.

The rest of this section will focus on the effects of strong magnetic fields in AFM systems with collinear magnetic structure. When a magnetic field is applied perpendicular to the sublattice magnetization, it causes the moments to tilt in the direction of the field, so that

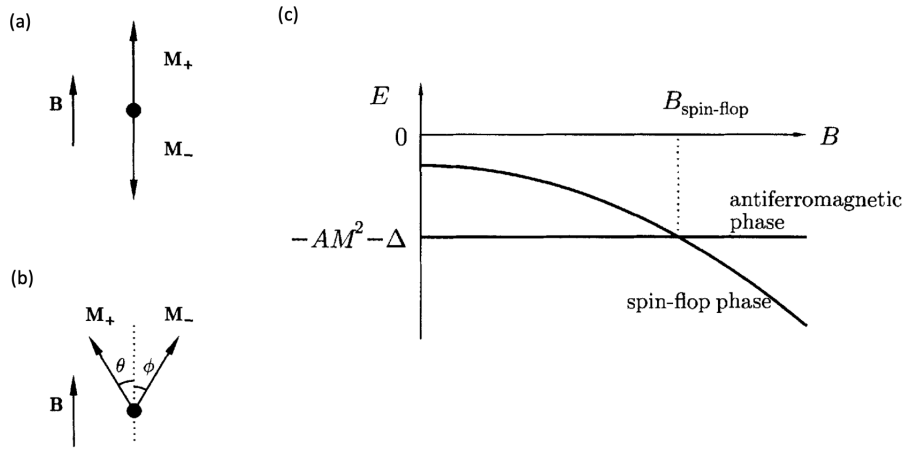

Figure 2.9: (a) An example two-sublattice collinear AFM state. (b) Spin-flop state. (c) Above a critical magnetic field it becomes energetically favorable for the system to switch into the spin-flop phase. Adapted from [51].

some net magnetization is produced along that direction. When a magnetic field is applied parallel to the sublattice magnetization, a critical field exists, above which moments suddenly change their orientation. Below this critical field which is known as the spin-flop field, the AFM state, shown in 2.9 (a), has the lowest energy. However, above the critical field the configuration that minimizes the energy of the system is shown in 2.9 (b). We can see why that is by writing down the energy of this two sublattice system, taking into account the Zeeman energies, exchange coupling and anisotropy, for the general case where one sublattice forms an angle θ with the magnetic field, and the other an angle ϕ [51]

$$E = -MBcos\theta - MBcos\phi + AM^2cos(\theta + \phi) - 1/2\Delta(cos^2\theta + cos^2\phi) \tag{2.35}$$

In the AFM case shown in 2.9 (a), $E = -AM^2 - \Delta$, and in the spin-flop phase, where $\phi = \theta$,

$$E = -2MBcos\theta + AM^2cos2\theta - \Delta cos^2\theta \tag{2.36}$$

Using the condition $\partial E/\partial\theta = 0$, one can calculate the angle that minimizes the energy, which will be a function of the magnetic field. This is graphed in Figure 2.9 (c), which shows

that at low fields the AFM state is energetically favorable, but the system undergoes a phase transition into the spin flop phase above the spin flop field. If the magnetic anisotropy is very strong it is also possible for the system to move into an FM state in a single step; this is known as the spin-flip transition.

2.7 Elements of magnetotransport in semimetals and topological semimetals

The application of a magnetic field can cause significant changes to the electrical transport in a semimetal. The transverse magnetoresistance (MR), obtained when electric and magnetic fields are perpendicular to each other, is given by

$$MR = \frac{\rho(B) - \rho(0)}{\rho(0)} \tag{2.37}$$

In a metal, this quantity is expected to have a quadratic field dependence and saturate quickly, however, semimetals often exhibit extremely high MR at low temperatures and high magnetic fields, which can reach a few thousand percent and even higher values have been observed in topological semimetals. The high MR can be attributed to electron-hole compensation, and high carrier mobilities. The carrier concentrations and mobilities can be easily extracted from the Hall resistivity ρ_{xy} when the transport is dominated by a single band at the FL; in this case ρ_{xy} is linear, and carrier density n and mobility μ can be calculated from equations

$$n = \frac{B}{e\rho_{yx}} \tag{2.38}$$

from which we can define the Hall coefficient $R_H = 1/\text{ne}$, and

$$\mu = R_H \cdot \sigma_{xx} \tag{2.39}$$

where σ_{xx} is the longitidunal conductivity, approximately equal to $1/\rho_{xx}$.

However, most semimetals have more than one band contributing to the transport properties. The carrier concentrations and mobilities are then estimated using the two-band

model, which assumes one eletron and one hole band contributing to the transport. Within this model, these quantities are then obtained by simultaneously fitting ρ_{xx} and ρ_{xy} to

$$\rho_{xx} = E_x/J_x = \frac{n_e\mu_e + n_h\mu_h + (n_e\mu_h + n_h\mu_e)\mu_e\mu_h B^2}{e(n_e\mu_e + n_h\mu_h)^2 + e(n_h - n_e)^2\mu_e^2\mu_h^2 B^2} \tag{2.40}$$

and

$$\rho_{yx} = E_y/J_x = \frac{B(n_h\mu_h^2 - n_e\mu_e^2) + (n_h - n_e)\mu_e^2\mu_h^2 B^3}{e(n_e\mu_e + n_h\mu_h)^2 + e(n_h - n_e)^2\mu_e^2\mu_h^2 B^2} \tag{2.41}$$

where n_e, n_h, μ_e and μ_h are fitting parameters, representing the carrier densities and mobilities of electrons and holes respectively.

When the carrier concentrations are equal to each other, combining Equations 2.37 and 4.1 leads to

$$MR = \mu_e\mu_h B^2 \tag{2.42}$$

In the case of perfect electron-hole compensation, MR is expected to increase quadratically without saturation, and is directly proportional to the product of the mobilities. This model has several shortcomings [52], however, it is still widely used as it can account for the high MR observed in compensated semimetals with high mobilities.

Another phenomenon that is frequently observed in the TMR of semimetals are the Shubnikov-de Haas (SdH) oscillations. Briefly, these oscillations arise from the quantization of the occupied bands into LLs. The spacing of these levels is proportional to the magnetic field. Increasing the magnetic field leads to a modulation of the density of states (DOS) at the FL, which can be detected as oscillations in physical properties that are dependent on the DOS. The energies of the LLs for nonrelativistic electrons in 3D materials with the magnetic field applied in the z-direction is given by [52]

$$\epsilon_{n,k} = \frac{\hbar eB}{m^*}(n - \frac{1}{2}) + \frac{\hbar^2 k_z^2}{2m^*} \quad (n = 1, 2, 3, ...) \tag{2.43}$$

while that of relativistic fermions is given by 2.28.

The SdH oscillations in a 3D system can be described by the Lifshitz - Kosevich formula

$$\Delta\rho \propto B^{1/2} R_T R_D R_S cos\left[2\pi\left(\frac{F}{B} - \gamma + \delta\right)\right] \tag{2.44}$$

R_T represents the thermal damping factor, which is a finite temperature correction to the Fermi-Dirac distribution, and is given by equation

$$R_T = \frac{\alpha T \mu}{B sinh(\alpha T \mu / B)} \tag{2.45}$$

R_D is the so-called Dingle damping factor, which represents the relaxation time due to impurity scattering,

$$R_D = exp(-\alpha T_D \mu / B) \tag{2.46}$$

and R_S is the spin damping factor, which accounts for the interference between two oscillations from spin-split LLs.

$$R_S = cos\left(\frac{\pi g \mu}{2}\right) \tag{2.47}$$

The constants μ and α are represent the ratio between the effective mass m^* and the free electron mass m_e, and the quantity $(2\pi^2 k_B m_e)/(\hbar e) = 14.69$ T/K, respectively. T_D is the so-called Dingle temperature, a useful quantity that is related to the quantum lifetime through equation

$$T_D = \hbar/(2\pi k_B \tau_q) \tag{2.48}$$

The frequency of the oscillations F, which can be determined by applying a Fast Fourier Transform (FFT), is related to the extremal cross section of the Fermi surface that is perpendicular to the magnetic field.

Of particular importance for the study of topological semimetals is the phase factor γ, which is equal to

$$\gamma = \frac{1}{2} - \frac{\phi_B}{2\pi} \tag{2.49}$$

where ϕ_B is the Berry phase. The cyclotron motion of particles with linear energy dispersions causes them to pick up a Berry phase of π, which can be determined by fitting the oscillations to Equation 2.44 [53]. However, non-ideal linear dispersions and gap openings at band crossing points can lead to deviations from a precise value of π. δ is a dimensionality factor which takes a value of 0 when the Fermi surface is 2D, and $\pm 1/8$ when the Fermi surface is 3D. The positive sign corresponds to a minimal (maximal) cross sectional area of the Fermi surface and the negative sign to a maximal (minimal) for electrons (holes) [54].

Quantum oscillations can also appear in the magnetization of a material, and this is known as the de Haas-van Alphen (dHvA). These oscillations can be probed using magnetization measurements and are described by

$$\Delta M \propto -B^{1/2} R_T R_D R_S sin\left[2\pi\left(\frac{F}{B} - \gamma + \delta\right)\right] \tag{2.50}$$

They can also be deteted by torque magnetometry, which takes advantage of the fact that a magnetic moment in a field B will experience a torque given by $\vec{\tau} = \vec{M} \times \vec{B}$. These oscillations are described by a similar expression as the SdH oscillations but with the sign depending on details of the Fermi pocket topology, given by

$$\Delta\tau \propto \pm B^{3/2} R_T R_D R_S sin\left[2\pi\left(\frac{F}{B} - \gamma + \delta\right)\right] \tag{2.51}$$

2.8 Superconductivity

Superconductivity was unexpectedly discovered in 1911 when Kamerlingh Onnes, who was trying to liquefy Helium, observed that the resistivity of a solid Hg sample abruptly dropped to zero at 4.2 K [55]. Currently, 33 elements and hundreds of other compounds are known to become superconducting under ambient pressure below a critical temperature T_c, where an interaction between conduction electrons causes them to form Cooper pairs. There are two spectacular phenomena that are associated with superconductivity; vanishing direct current (DC) electrical resistivity and a complete magnetic flux expulsion, independent of the superconductor's prior state (i.e. whether or not it was cooled below T_c under an applied field) also known as the Meissner effect. The observation of this phenomenon motivated a simple model of superconductivity summarized by a set of classical electrodynamic equations known as the London equations after the brothers Heinz and Fritz London who developed them [56]. These are the simplest equations that were introduced to describe superconducting phenomena on a macroscopic scale.

In a perfect conductor, Ohm's law is replaced by the first London equation

$$\vec{E} = \frac{\partial}{\partial t}\left(\frac{m}{n_s e^2}\vec{J}_s\right) = \frac{\partial}{\partial t}(\Lambda \vec{J}_s) \tag{2.52}$$

where $\vec{J_s}$ is the superconducting current density, m the electron mass and n_s the number density of superconducting carriers. This equation describes charges accelerating under the application of electric fields with no dissipation. The second London equation describes the relationship between magnetic field and superconducting current density:

$$\boldsymbol{\nabla} \times \vec{J_s} = -\frac{\vec{B}}{\Lambda} \tag{2.53}$$

If Ampere's law is applied to this equation then it can be re-written as

$$\nabla^2 \vec{B} = \frac{\mu_0 n_s e^2}{m} \vec{B} = \frac{1}{\lambda^2} \vec{B} \tag{2.54}$$

The solution to this equation is an exponential function, indicating that applied magnetic fields decay within a superconductor with a characteristic length λ known as the penetration depth.

Another successful phenomenological theory was provided by Vitaly Ginzburg and Lev Landau 15 years after the London theory was developed [57], and was based on Landau's previous theory of second-order phase transitions. In their work, they proposed that the free energy of a superconductor, F, can be written near T_c in terms of a complex order parameter $\psi(\vec{r})$, which is zero above T_c and nonzero in the superconducting state. The square of ψ was later interpreted as the density of the superconducting carriers.

Another important quantity in the description of superconductivity is the coherence length ξ. It was first introduced by Pippard to describe the length over which two electrons interacted with each other and is given by

$$\xi_0 = a \frac{\hbar v_f}{k_B T_c} \tag{2.55}$$

where v_F is the Fermi velocity and a is a proportionality constant.

Ginzburg and Landau introduced the dimensionless parameter κ given by $\kappa = \lambda/\xi$. Both the penetration and the coherence length are temperature dependent quantities that diverge as $(T_c - T)^{-1/2}$, so the ratio is essentially independent of temperature. The superconductors that had been discovered up to that point had $\lambda \approx 500$ Å and $\xi \approx 3{,}000$ Å so $\kappa << 1$.

These belong to the class that would later be called Type-I superconductors. They are characterized by one critical field H_c, above which superconductivity is abruptly destroyed.

When the penetration depth λ is much greater than the coherence length ξ, the magnetic field can penetrate the superconductor enough so that a mixture of superconducting and normal domains can form. Their formation is determined by the sign of the surface energy between the two domains, which is also associated with the value of the parameter κ. When the surface energy is positive and $\kappa < 1/\sqrt{2}$ the formation of domains is not favorable; these are the Type I superconductors that exist in either the Meissner or the normal states. When the surface energy is negative and $\kappa > 1/\sqrt{2}$ the formation of domains in the superconducting state is favorable. These Type-II superconductors are characterized by two critical fields H_{c1} and H_{c2}. Below H_{c1}, the superconductor expels the field completely, but between H_{c1} and H_{c2} magnetic flux is allowed to penetrate the sample in the form of vortices that are surrounded by the superconducting condensate. Above H_{c2}, the superconductor enters the normal state.

On a microscopic level, superconductivity can be explained by the Bardeen-Cooper-Schrieffer (BCS) theory, a remarkable theory that explained nearly all of the observed phenomena in conventional superconductors starting from interactions between electrons and atoms in a solid. The attractive interaction that leads to the formation of a Cooper pair is thought to be mediated by electron-phonon coupling, and this was based on the observation of the isotope effect, which refers to the observation that for many superconductors their critical temperature T_c and the atomic mass M vary according to $T_c M^{\alpha} =$ constant, with $\alpha \approx 1/2$. The fact that the Debye frequency varies as $\omega_D \propto M^{-1/2}$ hinted at lattice vibrations being involved in the mechanism that gives rise to superconductivity. The Cooper pair wavefunction has the following form [58]:

$$\psi_0(\vec{r}_1 - \vec{r}_2) = \left[\sum_{k>k_F} g_k cos\left[\vec{k}\cdot(\vec{r}_1 - \vec{r}_2)\right]\right](\uparrow\downarrow - \downarrow\uparrow) \tag{2.56}$$

Some of the assumptions of this theory are that the two electrons have to have equal and opposite momenta, and the coefficients g_k spherical symmetry. To obey the Pauli exclusion principle, a spin singlet configuration is necessary. Such a superconductor is termed conventional and is characterized by an isotropic, nodeless gap.

In a system that has no $\mathcal{I}$ symmetry, an asymmetric crystal field potential of the form

$$\vec{E} = -\nabla\Phi \tag{2.57}$$

can give rise to an antisymmetric spin-orbit interaction described by equation [59]

$$(\vec{E} \times \vec{p}) \cdot \vec{S} \tag{2.58}$$

also known as Rashba spin-orbit interaction. The pairing state in this case can no longer be described as spin-singlet or spin-triplet and, similarly, the spatial wavefunction cannot be taken to be symmetric or antisymmetric. It is this possibility of an admixture between spin-singlet and spin-triplet states and thus unconventional superconductivity that has made noncentrosymmetric superconductors an attractive new field of research in unconventional superconductivity.

Superconductivity and topology can coexist in materials known as topological superconductors. Topological superconductors are a class of exotic materials characterized by bulk superconductivity and with a nontrivial topology of their band structure expected to lead to the emergence of gapless surface states that host Majorana fermions [34]. The Majorana fermion is a type of exotic quasiparticle which has its origins in relativistic quantum mechanics, and its unique property is that it is its own antiparticle. While these hypothetical fermions have so far eluded detection as free particles, in condensed matter systems, where electrons and holes play the roles of particles and antiparticles respectively, the excitations in the middle of the superconducting gap are Majorana fermions. The protected surface states of topological superconductors are also expected to be of importance to topological quantum computing. Following theoretical predictions regarding the emergence of Majorana fermions due to interactions at the interface between conventional superconductors and topologically protected surface states [60], experimentalists have mostly focused their efforts in inducing superconductivity in systems that are already well known to be topological. Examples include $Cu_xBi_2Se_3$ [61] and $Sr_xBi_2Se_3$ [62], where Cu/Sr atoms are intercalated between Se layers.

CHAPTER 3

Experimental methods

3.1 Single crystal growth using the flux method

The importance of single crystals to solid state physics research cannot be emphasized enough. It would be fair to say that almost none of the experimental discoveries that have allowed the field to progress would have been possible, had it not been for the discoveries of methods to synthesize high quality single crystalline materials. Having a single ordered phase whose orientation can be determined is essential for the elucidation of the Fermi surface of a material through SdH or dHvA oscillations. Additionally, many properties, such as the magnetization or the resistivity, are anisotropic and can only be studied in a material that is a single ordered phase. Spectroscopic surface-sensitive techniques like ARPES or STM also rely heavily on the availability of high quality single crystals.

Single crystals for all of the materials studied in this dissertation were grown using the high temperature solution growth method, also known as flux growth. This method is based on traditional crystallization methods used in chemistry, where the solute has high solubility in a solvent at high temperatures but very limited solubility at low temperatures, and can precipitate out of solution. The flux here refers to the solvent; it can be further classified as self-flux when one of the constituents of the target compound is used as the solvent. This is usually preferable to the non-self flux method, as it avoids the introduction of impurities into the single crystals. The choice of flux is governed by several criteria; it should have a low melting point, low vapor pressure, not react with the crucible used and, most importantly, the rest of the elements must be soluble in it.

In solid state and inorganic chemistry, flux growth is one of the most commonly used

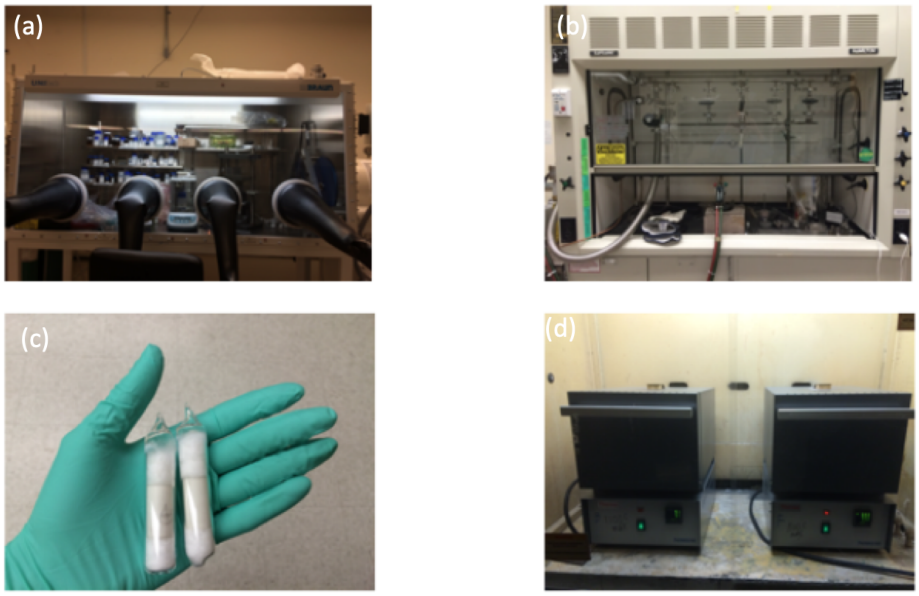

Figure 3.1: (a) A glovebox filled with Ar gas where most of the materials are kept. (b) The apparatus for evacuating and sealing quartz tubes. Tubes are connected to a pumping line, evacuated, and sealed off using a blow torch. (c) Sealed quartz tubes, with the starting materials held inside the Al_2O_3 crucibles. (d) Box furnaces that can reach 1100^{o}C.

techniques to grow single crystals. It should be noted, however, that many other techniques exist; these include the Bridgman, floating zone, and the Czochralski methods. The downside of these methods is that they can only be used to synthesize materials that melt congruently or near-congruently. The flux method on the other hand is much more flexible and does not require that the materials melt congruently. Some of the other benefits conferred by the flux method are the small amounts of materials required, the relatively simple equipment and the fast growth time scales, which are typically 1-2 weeks long. This is particularly important as optimization of the single crystal growth usually requires several attempts where the initial composition of the solution or the temperature profile are adjusted in order to maximize the size and quality of the single crystals.

The most commonly used crucibles to hold the materials are composed of Al_2O_3, which does not get attacked by most of the elements used as solutions (Bi, Ga, Ge In, Sn etc.) [63].

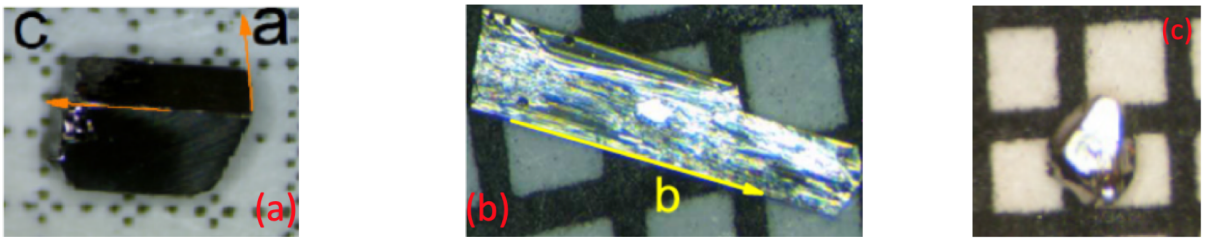

Figure 3.2: Pictures of single crystals grown using the flux method, against a 1mm scale. (a) CaCdGe, (b) CuMnAs, (c) $NbGe_2$.

To protect the solution from reacting with O_2 or N_2 in the air, the crucible is placed into an amorphous silica tube, evacuated using a pumping station and finally sealed off using an O_2 - CH_4 blow torch (Figure 3.1 (b)). A small amount of quartz wool is placed below and above the crucible, as shown in Figure 3.1 (c). The quartz wool at the bottom ensures that the different expansion rates of the crucible and the quartz tube won't cause the latter to rupture, while the piece at the top plays the role of a filter when the flux is being removed. Furnaces with programmable temperature controllers are used to heat the solution in the desired manner. A typical temperature profile consists first of rapid heating (100 ^{o}C/h - 200 ^{o}C/h) to temperatures around or over 1000 ^{o}C. The mixture is then allowed to homogenize for a few hours, followed by slow cooling (2 ^{o}C/hour - 5 ^{o}C/hour). It is during this slow cooling step that crystallization occurs, and as a result, usually the slower the cooling rate the larger the size of the single crystals. A centrifuge is used while the solution is still liquid to extract the crystals. The choice of decanting temperature is also crucial; it should be high enough that the flux is still liquid, but low enough for the crystals to have had ample time to grow. Any remaining flux on the crystals can be mechanically or chemically removed. Figure 3.1 summarizes most of the aforementioned steps in pictures and Fig. 3.2 show the pictures of the materials which will be discussed in my thesis, against a 1mm scale.

3.2 Crystal structure and composition determination

3.2.1 Powder X-ray diffraction

To perform phase identification and determine the purity and the lattice parameters of the materials synthesized, X-ray powder diffraction measurements were performed at room temperature using a PANalytical Empyrean CuKα diffractometer. Phase identification was performed using the software HighScore Plus and Rietveld Refinement was performed using the FullProf software.

3.2.2 Energy dispersive X-ray spectroscopy

Energy Dispersive X-ray spectroscopy (EDS) was used to identify the composition of Cu_xMn_yAs single crystals. Measurements were performed using an energy dispersive X-ray spectroscopic analyzer (EDAX; EDAX Inc.) mounted on a scanning electron microscope (JEOL JSM 6700 F). In EDS, an electron beam incident on the material removes an electron from an inner shell, and when another, higher energy electron fills the hole left in the inner shell, it emits an X-ray. These X-rays are characteristic of the elements present in the sample, and their energy and intensity are used to determine the composition of the sample.

3.3 Electrical and thermodynamic properties

3.3.1 Resistivity, magnetoresistance and Hall resistivity

The temperature dependent resistivity, the magnetoresistance and Hall resistivity were measured in a Quantum Design (QD) Physical Properties Measurement System (PPMS). The majority of the measurements were performed between 300 K and 2 K, and a Dilution Refrigerator (DR) was used when studying the superconducting properties of $NbGe_2$. When The four-probe method was used for measurements of the longitudinal resistivity, and the 6-probe method was used for measurements of the Hall resistivity. Single crys-

tals were typically cut and polished so as to approach a rectangular geometry. Pt wires where attached using Epotek EE129 or EJ2312 silver epoxy. To eliminate unwanted contributions from mixed transport channels of the magnetotransport data, data were collected while sweeping the magnetic field from -9 T to 9 T. The data were then symmetrized to obtain $\rho_{xx}(B)$ using $\rho_{xx}(B) = (\rho_{xx}(B) + \rho_{xx}(-B))/2$ and antisymmetrized to get $\rho_{yx}(B)$ using $\rho_{yx}(B) = (\rho_{yx}(B) - \rho_{yx}(-B))/2$. The sign of ρ_{yx} is chosen so that hole carriers lead to positive ρ_{yx}. The magnetoresistance is defined as MR $= (\rho_{xx}(B) - \rho_{xx}(0))/\rho_{xx}(B)$. Some magnetoresistance measurements for CuMnAs were also performed at the National High Magnetic Field Laboratory (NHMFL) in Tallahassee, FL at magnetic fields reaching 18 T.

3.3.2 Magnetization

Magnetic susceptibility and isothermal magnetization were measured in a QD Magnetic Properties Measurement System (MPMS). The crystals were attached to a quartz sample holder using a small amount of GE varnish, a low temperature insulating varnish.

3.3.3 Specific heat

Specific heat measurements at constant pressure were performed in a QD PPMS between 400 K and 2 K for most materials. The DR option was employed to measure the superconductivity in $NbGe_2$. Sample preparation for specific heat measurements involved ensuring that the sample could fit on a 2 mm x 2 mm platform, and that it had a flat surface that would enhance good thermal contact with the sample platform. Apiezon N grease was used to attach the sample to the platform at temperatures below 300 K, and H grease at temperatures above 300 K. The relaxation technique is used to measure the specific heat; during a measurement, heat is applied to the sample at constant power for a certain amount of time, followed by a cooling period of the same length. The temperature of the platform T obeys

the following equation

$$C_{total}\frac{dT}{dt} = -K_w(T - T_b) + P(t) \tag{3.1}$$

C_{total} is the total heat capacity of the sample and sample platform; K_w is the thermal conductance of the supporting wires; T_b is the temperature of the thermal bath (puck frame); and P(t) is the power applied by the heater. The solution of this equation allows for a calculation of C_{total}.

3.3.4 Single crystal neutron diffraction

Neutron diffraction measurements were performed at the HB-3A four-circle diffractometer at the High Flux Isotope Reactor (HFIR), Oak Ridge National Laboratory (ORNL) to determine both crystal structure and magnetic properties of CuMnAs single crystals. Neutrons are spin 1/2 particles with a non-zero magnetic moment. It can interact with nuclei through the strong nuclear force, giving information about the crystal structure, but they can also couple to the net magnetic moments of atoms. This magnetic scattering is what enables us to deduce the magnetic structure of a material. The neutron wavelength was 1.546Å from a bent Si-220 monochromator [64]. The magnetic symmetry analysis was carried out on the Bilbao Crystallographic Server [65] and the data were refined with the FULLPROF Suite [66].

CHAPTER 4

Magnetotransport properties of the single crystalline nodal-line semimetal candidates CaTX (T= Ag, Cd; X= As, Ge)

This chapter is adapted from [1].

4.1 Introduction

Topological semimetals are characterized by protected crossings between conduction and valence bands. These materials have recently attracted significant interest because of deep connections to high-energy physics, novel topological surface states, and unusual transport phenomena. When we embarked on our study of CaCdGe and CaAgAs, nodal-line semimetals were the least explored of the proposed topological phases. In nodal-line semimetals, conduction and valence bands cross to form a 1D closed loop in momentum space. They differ from the Weyl semimetal in three aspects : (1) the bulk Fermi surface is 1D in nodal-line and 0D in Dirac/Weyl semimetals ; (2) the density of states near the nodal touchings is proportional to $|E - E_{\mathrm{F}}|^2$ in nodal-line and $|E - E_{\mathrm{F}}|$ in Weyl semimetals ; (3) on the surface, the nodal-lines are "stitched" together by a "drumhead" surface state, while Weyl nodes are connected by Fermi arc surface states. These unique properties of nodal-line semimetals make new physics accessible. For example, the weak dispersion of the drumhead surface states leads to a large density of states near the Fermi level. Possible interaction-induced instabilities on the surface of nodal-line semimetals have been widely discussed in theory [67–69].

Despite intense theoretical interest [70–77], there haven't been many experimental studies on nodal-line semimetals. One of the major reasons for that was the absence of ideal nodal-line semimetals. Ideal here refers to a semimetal with a band structure that contains only nodal lines near the Fermi energy, and no other topologically trivial Fermi pockets. Such a "hydrogen atom" nodal-line semimetal is crucial for separating the spectroscopic and transport signals of the nontrivial nodal lines from those of trivial states. For example, even before the discovery of TaAs, Fe, an elemental ferromagnetic metal, was known to have hundreds of Weyl nodes in its band structure [78]. However, Fe is not an ideal platform to study Weyl physics because its complicated Fermi surface is dominated by irrelevant (non-Weyl) trivial pockets. In fact, because Weyl nodes are symmetry allowed when time-reversal or inversion symmetry are broken, they are likely to exist in the band structure of most ferromagnetic or non-centrosymmetric compounds. It is therefore important to identify materials where the topological band crossings (Dirac nodes, Weyl nodes, or nodal-lines) are the dominant features at the Fermi level. Examples of such Weyl or Dirac semimetals are Cd_3As_2, Na_3Bi, and TaAs, and so, unsurprisingly, these compounds have been studied extensively. By contrast, in nodal-line semimetals, experimental work has been focused on $PbTaSe_2$ and ZrSiX (X=S, Se, Te) [79, 80]. However, both compounds have a quite complex band structure where multiple trivial pockets coexist with the nodal lines at the Fermi level. CaAgAs and CaAgP were recently predicted to be "hydrogen atom" nodal-line semimetals as only two nontrivial bulk bands touch along a line and no other trivial bands exist at the Fermi level [81]. They crystallize in the P-62m space group, and their crystal structure consists of a 3D network of edge and corner sharing $AgAs_4$ tetrahedra as shown in Figure 4.3(a). A study on polycrystalline CaAgAs/P that was published while we were studying this material revealed that it was a low carrier density metal and that CaAgAs was a more promising candidate than CaAgP for the purpose of studying nodal-line physics [82].

Single crystals are superior to polycrystalline samples for electrical transport and surface sensitive measurements, and this motivated us to study the magnetotransport properties of CaAgAs and its "sister" compound CaCdGe. In this chapter, I will show that our work

suggests that CaAgAs has a topological surface state and a single donut-like hole Fermi pocket, experimentally proving it is an ideal material realization of a topological nodal-line semimetal. Furthermore, we show that CaCdGe not only hosts the nontrivial nodal-line feature but also an extra trivial electron pocket at the Fermi level. Lastly, the comparative study of the magnetotransport in these two compounds elucidates the origin of the extremely larger magnetoresistance and the highly debated linear magnetoresistance observed in topological semimetals.

4.1.1 Single crystal growth of CaAgAs and CaCdGe

CaAgAs single crystals were grown using AgAs as self-flux. This step is commonly taken when the desired material includes As. As is an extremely hazardous element that sublimates at 614 ^{o}C. Its volatility can be minimized by allowing it to react with another element at temperatures below its sublimation point. As chunks were ground to form a fine powder using a mortar and pestle, and then mixed thoroughly with Ag powder at a 1:1 molar ratio. These procedures took place in the glovebox shown in Figure 3.1 (b), which is filled with Ar gas. This mixture was then pressed into a pellet, placed inside a quartz tube and slowly heated to 600 ^{o}C, where it was allowed to dwell for 1-2 days. This type of synthesis is an example of the solid state reaction, commonly used for the preparation of polycrystalline materials. The mixture never melts, but the high temperatures and close contact between the surfaces of particle grains facilitates the formation of bonds between them. AgAs was then mixed with Ca granules using a molar ratio of Ca:AgAs=1:4, placed in Al_2O_3 crucibles and then sealed inside quartz tubes under 1/3 atm of Ar. The quartz tube was heated to 1100 ^{o}C, kept at that temperature for 3 hours, and cooled to 750 ^{o}C at a rate of 3 ^{o}C per hour. The single crystals were subsequently separated from the flux by decanting using a centrifuge.

CaCdGe single crystals were grown using an excess of Cd as the flux. The binary phase diagrams of Ca-Cd and Ge-Cd were investigated to ensure that Ca and Ge would be soluble in Cd. As shown in Figure 4.1, a narrow window of solubility in Cd exists for both Ca and Ge.

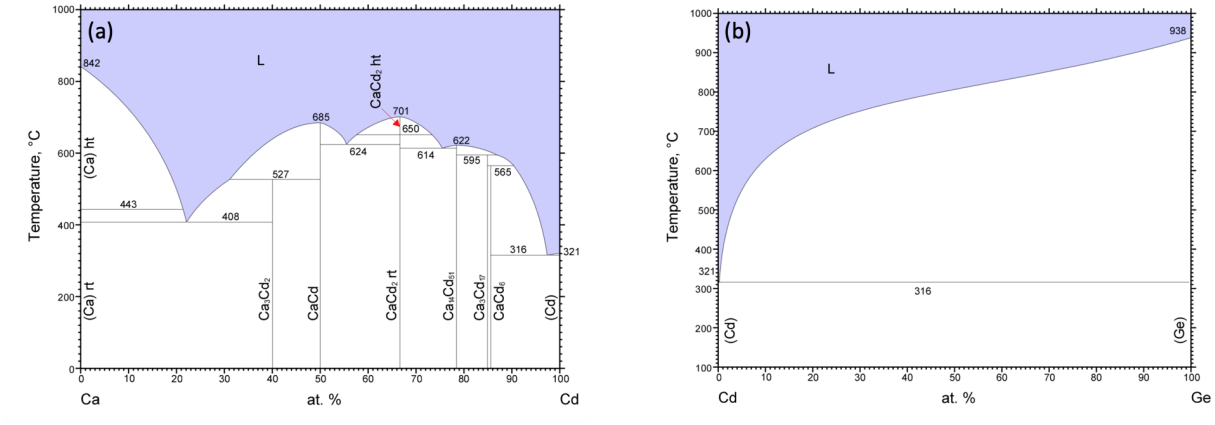

Figure 4.1: Binary phase diagram for Ca-Cd (a) and Ge-Cd (b). Taken from [83, 84].

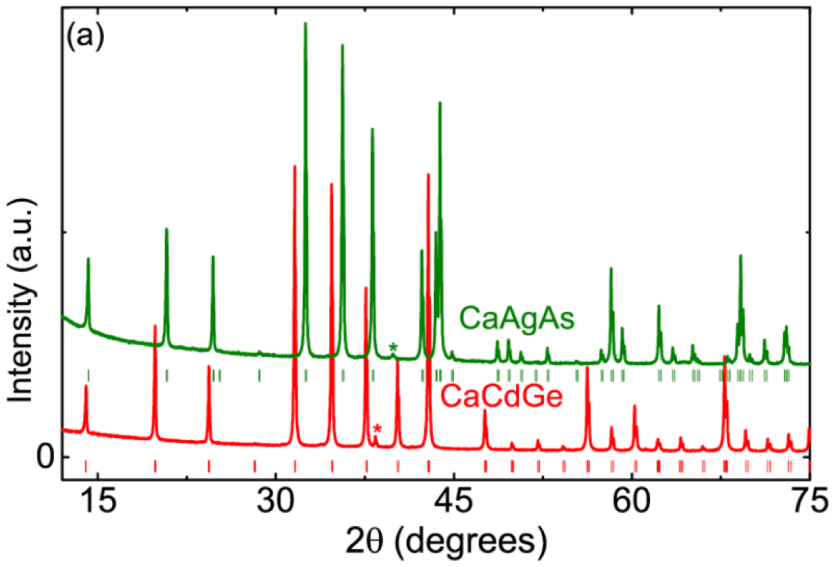

Figure 4.2: The powder x-ray diffraction patterns of CaCdGe and CaAgAs. The ticks below each pattern indicate the Bragg peak positions determined by the respective crystal structure. Some very small impurity peaks are detected in both patterns; in CaAgAs this corresponds to AgAs, and in CaCdGe it is due to Cd.

The materials were combined at a ratio of Ca:Ge:Cd=1:1:47 and sealed inside quartz tubes in the same manner as CaAgAs. Cd is a volatile, toxic element with high vapor pressure, so synthesis attempts must be carefully planned out. The solution was initially heated to 800 ^{o}C for 3 hours, and cooled to 400 ^{o}C at a rate of 3 ^{o}C/hour. However, only small needle-like crystals were obtained, which indicated that higher temperatures where necessary to grow larger single crystals. After several trials, an optimal temperature profile was determined; heating the solution to 1000 ^{o}C and increasing the amount of Cd by 25%, yielded large, thick single crystals. One such single crystal is shown in Figure 3.2 (a). This reaction took place in a furnace that had been placed inside a fume hood to ensure that no Cd vapor would enter the laboratory in the event of an explosion.

The x-ray diffraction patterns of CaAgAs and CaCdGe are shown in Figure 4.2. The refined lattice parameters were $a = b = 7.3056(1)$Å and $c = 4.4785(1)$Å for CaCdGe, and $a = b = 7.2041(1)$Å, c = 4.2699(1)Å for CaAgAs.

4.2 Transport properties of CaAgAs and CaCdGe

The valence analysis (Ca^{2+}, Ag^{1+}, As^{3-} for CaAgAs and Ca^{2+}, Cd^{2+}, Ge^{4-} for CaCdGe) suggests a semimetal/ semiconductor ground state for both compounds, which was confirmed by band structure calculations. As shown in Figure 4.3, the conduction and valence bands cross in the absence of SOC. The energy dispersion around the Fermi level is nearly linear and the band crossing forms a 1D loop (a nodal line) that encloses the Γ point. Theoretical calculations show that near the Γ point, the lowest conduction and valence bands consist of the Ag(Cd) 4d and As(Ge) 4p orbitals, respectively. A band inversion takes place near the Γ point as the top of the valence (As 4p) band moves above the bottom of the conduction (Ag 4d) band. Furthermore, because the z = 0 plane of the crystal is a mirror plane, the electron states on the $k_z = 0$ plane must be eigenstates of the mirror operator M_z.

The Ag 4d conduction band and the As 4p valence band have opposite mirror eigenvalues. This fact prevents them from hybridizing, leading to a nodal line on the $k_z = 0$ plane enclosing

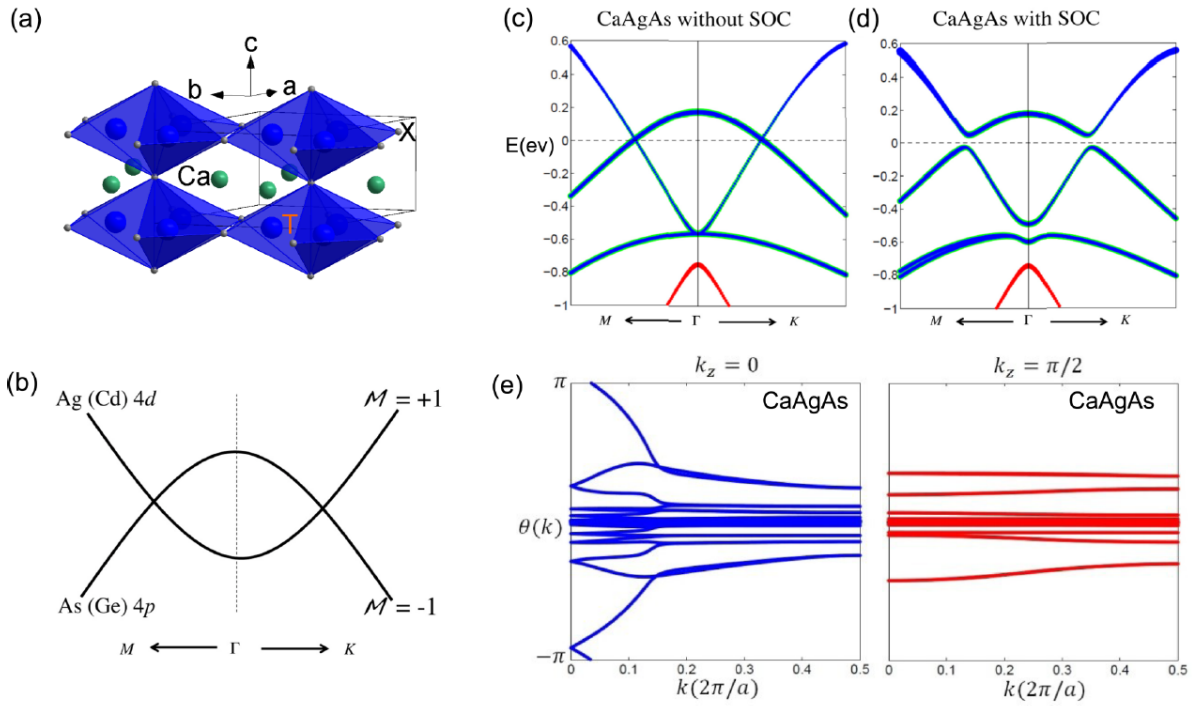

Figure 4.3: (a) Crystal structure of CaAgAs and CaCdGe. The TX_4 octahedra are shown in blue and the Ca atoms are shown in green. (b) and (c) Mirror symmetry protected nodal-lines in CaAgAs and CaCdGe. (b) Schematic of a band structure diagram for the nodal-line feature in CaAgAs and CaCdGe. The conduction and valence bands consist of the Ag(Cd) 4d and As(Ge) 4p orbitals, respectively. The band crossings near the Γ point are protected because the two bands have opposite mirror eigenvalues. (c) and (d) First-principles calculated band structures of CaAgAs near the Γ point without SOC (c) and with SOC. (e) Wilson loop calculation of the SOC band structure on the $k_z = 0$ and $k_z = \pi/2$ planes.

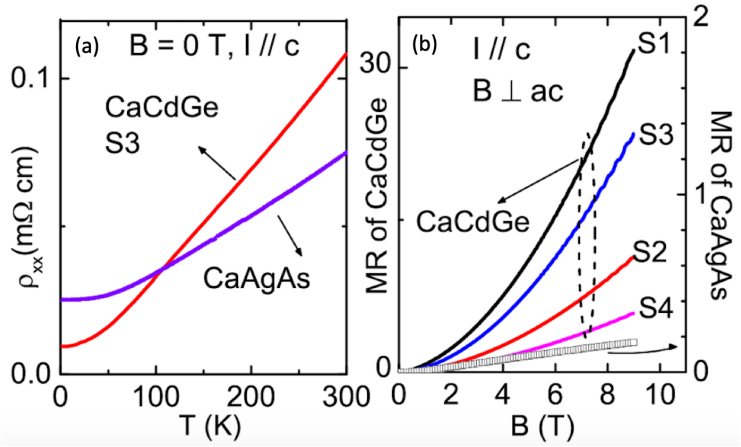

Figure 4.4: (a) Temperature dependence of the electrical resistivity ρ_{xx} for CaCdGe and CaAgAs at $B = 0$ T with $I//c$. (b) MR of CaCdGe and CaAgAs single crystals at T = 2 K with $I//c$ and $B \perp ac$.

the Γ point. The inclusion of SOC leads to the opening of a nontrivial gap of about 20meV, as shown in Figure 4.3(d). This can be clearly seen in the Wilson loop calculation of the SOC band structure on the $k_z = 0$ and $k_z = \pi/2$ planes shown in Figure 4.3(e). As long as the Fermi level is not located in this narrow gap, both CaAgAs and CaCdGe are expected to exhibit semimetallic behavior.

CaCdGe and CaAgAs both demonstrate metallic behavior, as can be seen in Figure 4.4(a). The RRR is 3 with a residual resistivity ρ_0 of 25 μΩ·cm for CaAgAs and 12 with a ρ_0 of 9 μΩ·cm for CaCdGe. Figure 4.4(b) shows the transverse magnetoresistance (MR) of four CaCdGe samples, and one CaAgAs sample. CaCdGe exhibits large, quadratic-like MR with no sign of saturation up to 9 T. S1 in particular, has an MR around 3200% at 2 K under 9 T. This behavior is reminiscent of the extremely large MR that was observed in materials such as the Weyl semimetals TaAs and NbP, the type II-Weyl semimetal WTe_2, the Dirac semimetal Cd_3As_2 and the weak topological insulator $NbAs_2$ [16, 23, 85–90]. In sharp contrast to the giant quadratic MR of CaCdGe, the MR of CaAgAs only reaches about 18% and most notably has a nonquadratic character, which agrees with what was observed in polycrystalline CaAgAs [82].

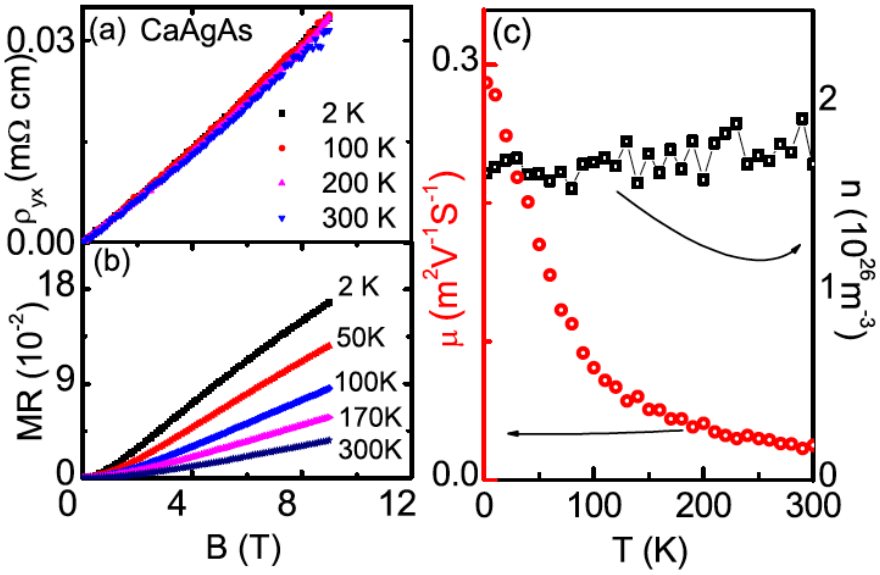

Figure 4.5: CaAgAs single crystal with $I//c$ and $B \perp ac$: (a) Hall resistivity ρ_{yx}. (b) Field dependent transverse MR. (c) Temperature dependent carrier density and mobility.

Figure 4.5(b) shows the MR of CaAgAs for some representative temperatures. While quadratic at small magnetic fields, it develops a linear behavior at high fields. Linear MR has also been observed in the topological semimetals Na_3Bi [91], WTe_2 [90], and Cd_3As_2 [16,89,92] that have linear energy-momentum dispersions, as well as materials with parabolic dispersions such as $Ag_{2-\delta}Se$ [93] or the GaAs quantum well [94], and recently in the candidate topological superconductor Au_2Pb [95]. Despite being a subject of study for decades, its origin is still under debate. Since it has been observed in a few topological semimetals, it was believed to be likely associated with the non-trivial band characters of these materials. However, the counter-experiment on the n-type GaAs well, which has a quadratic electron-like band structure, showed that this simple, defect-free system was also characterized by an extremely high (10^5% at 30T) linear MR, which was eventually attributed to density fluctuations [94]. Even though CaAgAs contains only nodal-lines at its Fermi level, since the MR is just around 18% at 2 K at 9 T, this suggests that the linear behavior is probably due to charge fluctuations as well, which is reasonable considering the possible As deficiency in this material.

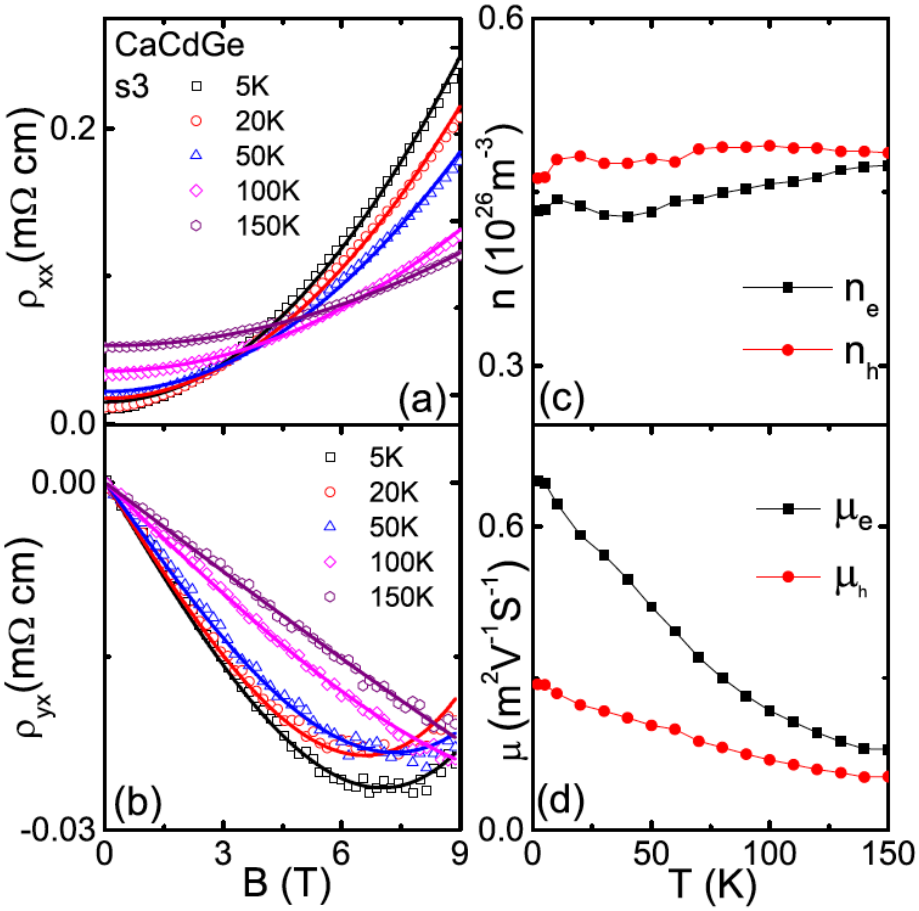

Figure 4.6: CaCdGe single crystal S3 with $I//c$ and $B \perp ac$: (a) transverse magnetoresistivity ρ_{xx}. (b) Hall resistivity ρ_{yx}. The symbols correspond to experimental data, while the lines are the curves obtained from the two band model fitting. (c) Temperature dependent carrier densities. (d) Temperature dependent mobilities.

Figure 4.5(a) shows the positive Hall resistivity ρ_{yx} of CaAgAs. It is linear with applied magnetic field up to 9 T and shows almost no temperature dependence, indicating single-band transport and that hole carriers overwhelmingly dominate the electrical transport. This is indeed consistent with the theoretical prediction that only one Fermi pocket exists at the FL [81]. Therefore, using single-band theory with $n = B/e\rho_{yx}$ and $\mu = R_H/\sigma_{xx}$, we obtained the temperature dependent carrier density n and mobility μ which are shown in Figure 4.5(c). The carrier density n is temperature independent and is of the order of 1.7 $\times$ 10^{26} m^{-3}, while μ shows a strong temperature dependence ranging from 0.3 m^2 V^{-1} s^{-1} at 2 K, to 0.025 m^2 V^{-1} s^{-1} at 300K.

The transport properties of CaCdGe are shown in Fig. 4.6(a)(b). We can see that CaAgAs and CaCdGe exhibit quite different behavior under magnetic field. While CaAgAs features a linear Hall resistivity and small MR, CaCdGe shows non-linear Hall resistivity and large MR. The non-linear Hall resistivity suggests that transport in this compound is governed by both electron and hole carriers and two-band model should be used. The carrier densities and mobilities of the carriers in CaCdGe were thus obtained using the semiclassical two band model [87, 96].

$$\rho_{xx} = E_x/J_x = \frac{n_e\mu_e + n_h\mu_h + (n_e\mu_h + n_h\mu_e)\mu_e\mu_h B^2}{e(n_e\mu_e + n_h\mu_h)^2 + e(n_h - n_e)^2\mu_e^2\mu_h^2 B^2} \tag{4.1}$$

and

$$\rho_{yx} = E_y/J_x = \frac{B(n_h\mu_h^2 - n_e\mu_e^2) + (n_h - n_e)\mu_e^2\mu_h^2 B^3}{e(n_e\mu_e + n_h\mu_h)^2 + e(n_h - n_e)^2\mu_e^2\mu_h^2 B^2} \tag{4.2}$$

where n_e, n_h, μ_e and μ_h are fitting parameters, representing the carrier densities and mobilities of electrons and holes respectively.

Simultaneously fitting our data to equations 4.1 and 4.2, allowed us to determine the temperature dependences of n_e, n_h, μ_e and μ_h. The fitting curves are shown as lines in Figures 4.6(a) and 4.6(b) and agree well with the experimental data. Figures 4.6(c) and 4.6(d) show the temperature dependent n_e, n_h, μ_e and μ_h calculated from the fits. Both electron and hole carrier densities are approximately equal to 5 $\times$ 10^{25} m^{-3} and show essentially no temperature dependence. This nearly perfect electron-hole compensation is most likely the

origin of the large MR we observed. Both μ_e and μ_h (Figure 4.6(d)) increase with decreasing temperatures, consistent with the idea of weaker scattering at lower temperatures. At 2K, μ_e is equal to 0.7 m^2 V^{-1} S^{-1}, and μ_h is equal to 0.3 m^2 V^{-1} S^{-1}. The mobilities are smaller than those observed in other compensated semimetals [97], leading us to believe that they are not responsible for the large, nonsaturating MR, which we ultimately attributed to the near perfect electron-hole compensation.

4.3 Shubnikov-de Haas oscillations in CaCdGe

In CaCdGe, Shubnikov-de Haas (SdH) oscillations were observed above 6 T in the resistivity, as can be seen in Fig. 4.7(a). These oscillations are a result of the singularity in the density of states that occurs every time a Landau level crosses the Fermi level as we discussed in Chap. 2. We analyzed the SdH data by first subtracting a polynomial background and then plotting $\delta\rho_{xx} = \rho_{xx}$-$\rho_{bkg}$ as a function of $1/B$.

Figure 4.7(a) shows $\delta\rho_{xx}$ for S1 as a function of $1/B$ at a few representative temperatures with I//c and B⊥ac. The oscillations are periodic in $1/B$ and their frequency F is related to the extremal cross sectional area S of the Fermi surface perpendicular to the magnetic field through the Onsager relation [96]

$$F = \frac{\hbar S}{2\pi e} \tag{4.3}$$

The fast Fourier transform (FFT) spectrum of the oscillations reveals only one frequency around 204 T, which is labeled as F_a^{SdH} and shown in the inset of Fig. 4.7(b). The amplitude of the oscillations, taking finite temperature and impurity scattering effects into account, is described by the Lifshitz-Kosevich formula, given by equation

$$\frac{\delta\rho_{xx}}{4\rho_0} \propto R_T R_D \tag{4.4}$$

where R_T and R_D are given by equations 2.45 and 2.45 respectively. By fitting the temperature dependence of the oscillations at fixed field, we extracted an effective mass of 0.23 m_e, as shown in Fig. 4.7(b). We calculated a Dingle temperature of 8.9 K. By fitting the 3

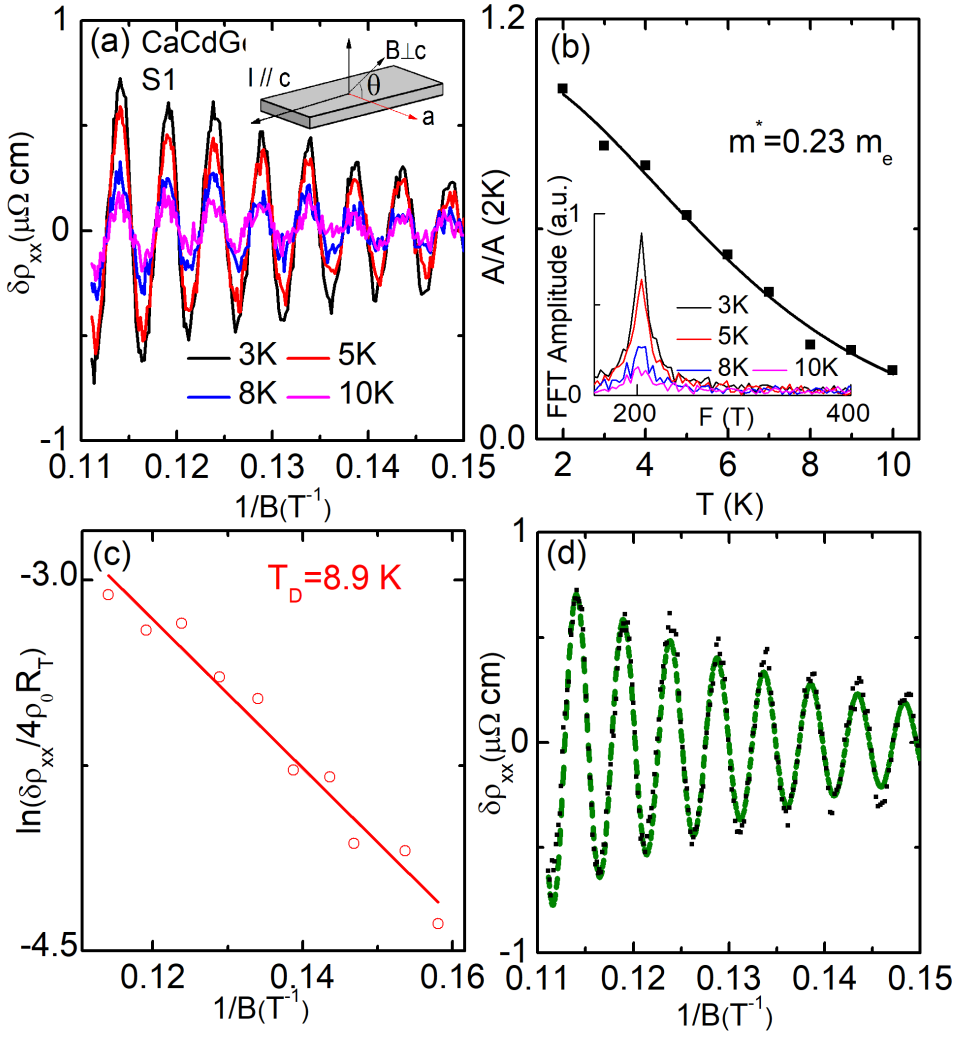

Figure 4.7: (a) The oscillations in $\delta\rho_{xx}$ are periodic in 1/B and their amplitude decays as the temperature is lowered. Inset: Measurement configuration. (b) Temperature dependence of the normalized amplitude of the oscillations denoted as A/A(2K). Inset: FFT spectrum of the oscillations for a few representative temperatures. The magnetic field was perpendicular to the *ac* plane. (c) 1/B dependence of the quantity $ln(\delta\rho_{xx}/4\rho_0 R_T)$ with a fit to extract the Dingle temperature. (d) The LK fit of the 3 K data. Black dots indicate data points and the green dashed line corresponds to the fit.

K data with the LK formula Eq. 2.44, we obtained a trivial Berry phase of 0.21π. This is consistent with our conclusion that the observed oscillations are associated with the trivial electron Fermi pocket.

The appearance of oscillations in CaCdGe can be understood by considering that at 2 K and 9 T, $\hbar\omega_C = \hbar eB/m^* = 4.52$ meV, much larger than $k_BT = 0.17$ meV, meaning that thermal smearing effects that can obscure quantum oscillations have been overcome at these experimental conditions. In contrast, for CaAgAs, $\omega\tau$ is equal to $|\rho_{yx}|/\rho_{xx}$ and at 2 K and 9 T it is equal to 1.2. This would place it in the intermediate field region, and explain why quantum oscillations were not observed under our experimental conditions. Using the Onsager relation, we estimated the Fermi wave vector

$$k_F = \sqrt{2eF/\hbar} \tag{4.5}$$

and the Fermi velocity

$$v_F = \hbar k_F/m^* \tag{4.6}$$

to be 0.079 $\mathring{A}^{-1}$ and 4.0×10^5 m s^{-1} respectively.

Metallic systems are characterized by two different relaxation times. The transport lifetime τ_{tr} is given by equation

$$\tau_{tr} = \frac{\mu m^*}{e} \tag{4.7}$$

and is a measure of backscattering processes that relax the current. The quantum lifetime τ_q on the other hand, reflects all processes that can give rise to Landau level broadening [16, 98]. The ratio τ_{tr}/τ_q typically exceeds 1, as the quantum lifetime takes into account more scattering mechanisms. However, extremely high values have been associated with novel mechanisms that protect against backscattering and give rise to an extremely high mobility [16]. Using equation 2.48 and $T_D = 8.9$ K, we calculated a quantum lifetime of 1.4×10^{-13} s at 2 K. We estimated the transport lifetime using the effective mass we calculated and the average of the electron and hole mobilities, which resulted in the value 6.5×10^{-13} s. Thus, the ratio τ_{tr}/τ_q was estimated to be 4.6, which is typical of metallic systems, indicating that no clear topological protection of the scattering is at play here.

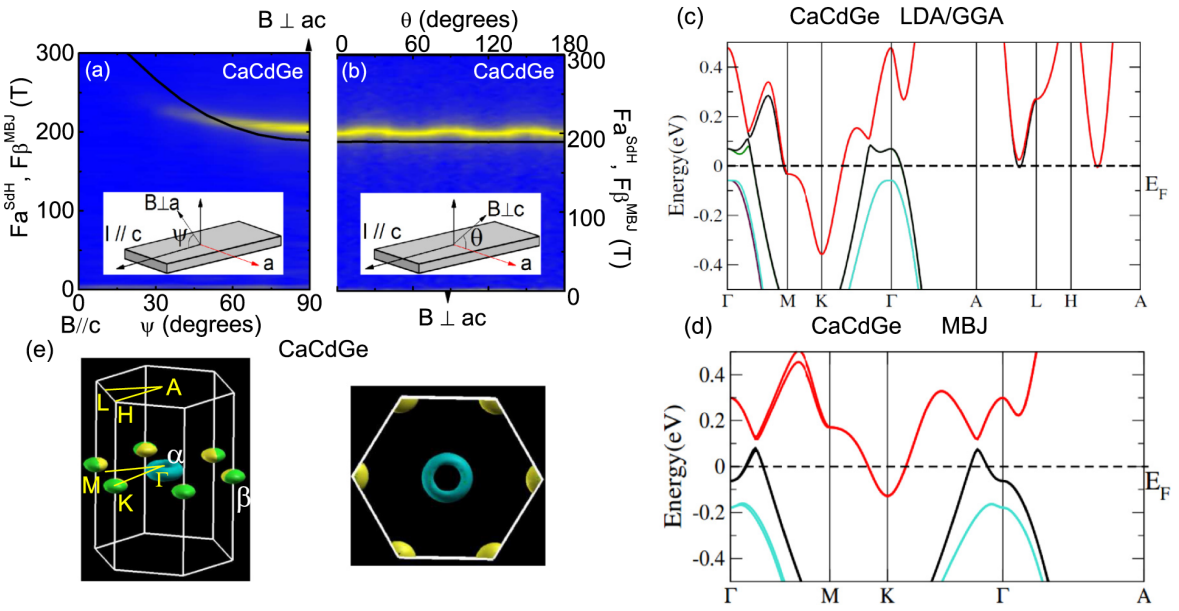

Figure 4.8: (a) and (b) Angular dependence of the experimental F_a^{SdH} (yellow lines; see text) and the calculated F_β^{DFT} (black lines; see text) with the measurement geometries in the insets. (c) and (d) The electronic band structure of CaCdGe with SOC: (c) using the LDA/GGA potential and (d) using the MBJ potential. (e) The Fermi pockets associated with (d).

4.4 Fermiology revealed by quantum oscillations and DFT calculations

The angular dependence of the SdH oscillations we observed in CaCdGe allowed us to determine portions of its Fermi surface experimentally. By adjusting the theoretical calculations with the experimentally mapped-out Fermi surfaces, we can reveal the Fermiology of CaCdGe. Figures. 4.8(a) and (b) show the angular dependence of F_a^{SdH} with two different rotation geometries depicted in the insets, respectively. This allows us to study the 3D characteristics of the Fermi pocket associated with F_a^{SdH}. As plotted in Fig. 4.8(b), when the field is rotated in the basal hexagonal *ac* plane, F_a^{SdH} shows a sixfold rotational symmetry with a ratio of 1.028 between maxima and minima. This is consistent with its hexagonal crystal structure and indicates small in-plane anisotropy of the associated Fermi pockets.

The theoretically predicted band structures are shown in Figs. 4.8(c) and 4.8(d). Details of this calculation can be found in Appendix B. Regardless of the choice of potential, an extra trivial band (red), besides the nontrivial band carrying the nodal-line feature as proposed in CaAgAs (black), also crosses the Fermi level in CaCdGe. The calculated band structures show that both conduction and valence bands cross the Fermi level, supporting our experimental observation of electron-hole compensation.

Despite the similarities between the two calculated band structures, their calculated angular dependence of the quantum oscillation frequencies are quite different. We were unable to relate F_a^{SdH} to any of the Fermi pockets arising from the LDA/GGA band structure since all pockets are very large. On the other hand, the size of F_a^{SdH} matches well with the oval shaped β Fermi pocket in Fig. 4.8(e), which originates from the trivial band shown in red when the MBJ potential was used. The comparison between the F_a^{SdH} (yellow line) and the calculated oscillation frequency associated with the β pocket, F_β^{DFT} (black lines) is shown in Figs. 4.8(a) and 4.8(b). Although the magnitudes of the two frequencies are in good agreement with each other, F_β^{DFT} shows much stronger anisotropy than F_a^{SdH} in the *ac* plane but weaker anisotropy in the *ab* plane and does not exhibit the six-fold rotational

symmetry observed in the experimental data. No frequencies associated with the toroidal α Fermi pocket were observed under our experimental conditions, which might be possible if higher magnetic field is applied, as was the case for CaAgAs [99].

4.5 Topological surface states revealed by ARPES in CaAgAs

ARPES measurements performed by our collaborators on our crystals provided clear evidence that CaAgAs is indeed a "hydrogen atom" topological nodal-line semimetal. Its topological surface state is protected by a mirror reflection symmetry; the mirror reflection plane is the plane where the Ca atoms are located, between two $AgAs_4$ octahedra. The nodal ring around the Γ point in the absence of SOC is expected to give rise to a topologically protected surface when projected onto the (0001) surface [81]. The DFT calculations of the band structure of CaAgAs with the inclusion of SOC are shown in Figure 4.9(g). When SOC is taken into account, it causes a gap of 73 meV to open at the Γ point while the topological surface state is still protected by $\mathcal{T}$. ARPES measurements showed clear evidence of this surface state. These results, along with a comparison to angle-resolved density of states (AR-DOS) calculations, are summarized in Figs. 4.9(a)-(e). Figure 4.9(a) shows linear bands on both sides of the Γ point along the Γ-A direction. These bands are absent from the bulk band structure, but can be seen in the AR-DOS (Figure 4.9(d)), which contains information from both bulk and surface bands, indicating that the linear bands are surface bands. Linear bands, marked by red arrows, can also be observed along the other two directions (Figures 4.9(b) and (c)), and correspond to the surface state obtained by DFT calculations along those directions (Figures 4.9(e)-(f)), which is connected to the Dirac cone topological surface state near the theoretical Fermi level. These linear bands undoubtedly correspond to the topological surface state, providing evidence that CaAgAs really is the "hydrogen atom" of topological nodal line semimetals.

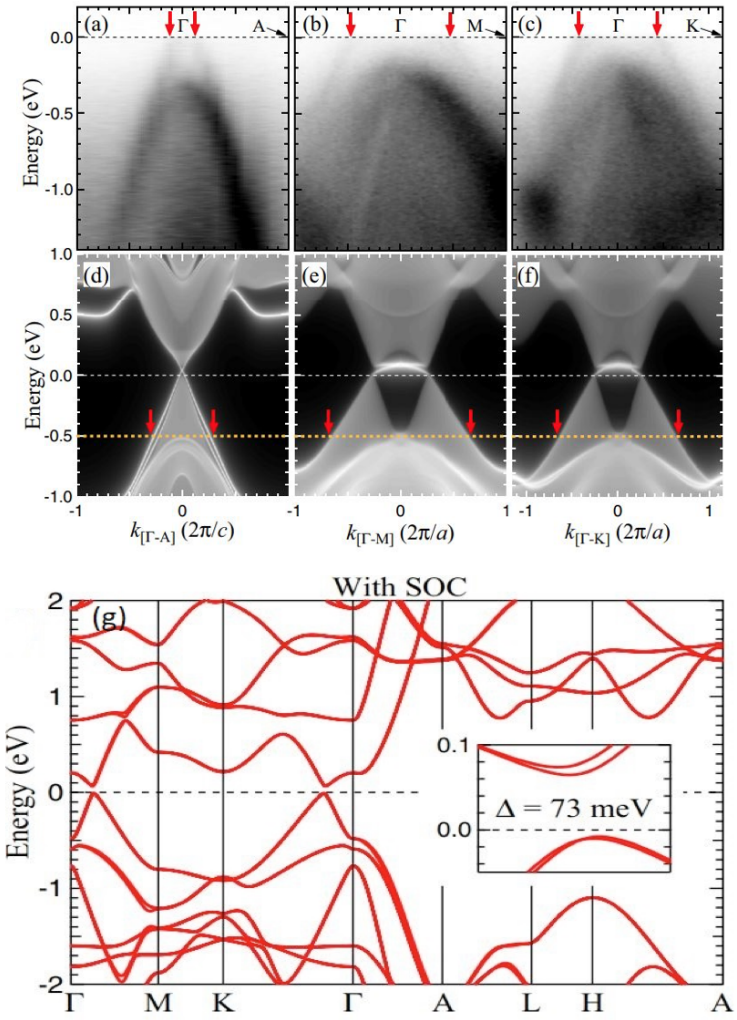

Figure 4.9: ARPES measurements and DFT calculations of the band dispersion along high symmetry directions. The red arrows indicate the lower part of the topological surface states. (a) - (c) ARPES momentum-energy maps along (a) Γ-A, (b) Γ - M, and (c) Γ-K. (d)-(f) DFT-derived angle-resolved density of states along (d) Γ-A, (e) Γ - M, and (f) Γ-K. The bright curves indicate topological surface states and the yellow dashed line shows the approximate Fermi level position that agrees with the ARPES data. (g) The DFT calculated band structure of CaAgAs with SOC. The inset shows the detail of the band dispersion along Γ - M near the nodal point. The nodal line around the Γ point is gapped out under SOC, resulting in a topological insulator with $\Delta = 73$ meV. Adapted from [2].

4.6 Conclusion and outlook

CaAgAs was predicted to be a topological nodal-line semimetal with only the nodal-line feature at the Fermi level. To engineer a similar band structure and elucidate the effect of non-trivial band characteristics, we also synthesized single crystals of its "sister" compound CaCdGe. CaCdGe has the same crystal structure but with different electron fillings. Therefore, these two materials provide an ideal platform to perform comparative studies. Our magnetoresistance, Hall measurements and DFT calculations reveal that CaAgAs is a single-band material with one donut-like hole Fermi pocket, consistent with the proposal that it is the first "hydrogen atom" nodal-line semimetal. Our quantum oscillations measurement on CaCdGe are consistent with the DFT calculations, suggesting that that CaCdGe has one donut-like hole Fermi pocket originating from the band with the nodal-line feature and one trivial ovoid-like electron Fermi pocket. The additional trivial electron pocket in CaCdGe has a large impact on the magnetotransport properties leading to an extremely large non-saturating quadratic MR up to 3200%, while in CaAgAs it is small and linear. Our data analysis suggests that the electron-hole compensation effect is responsible for the extremely large MR observed in CaCdGe and that charge fluctuations can account for the linear MR in CaAgAs, elucidating that neither effect is necessarily associated with non-trivial band topology. Furthermore, our collaboration with the ARPES group directly imaged the topological surface state and revealed a single donut-like hole Fermi pocket at the Fermi level, providing smoking gun evidence of CaAgAs being the first material realization of the "hydrogen atom" topological nodal-line semimetal. It is worth noting that a recent study of CaAgAs under a magnetic field up to 45 T shows quantum oscillation and the data analysis indicates a non-trivial Berry phase of π for the donut-like pocket [99].

CHAPTER 5

Magnetic order induces symmetry breaking in the single-crystalline orthorhombic CuMnAs semimetal

The majority of this chapter has been adapted from [3].

5.1 Introduction

As with many of the recently studied topological semimetals, CuMnAs was first synthesized and characterized years before any of its topological properties were predicted [100]. What piqued our interest in this material was the theoretical prediction by Tang et al. that 3D antiferromagnetic (AFM) Dirac semimetals can, under certain conditions, break both time reversal $\mathcal{T}$ and inversion $\mathcal{P}$ symmetries but preserve their product $\mathcal{PT}$, allowing a topological protection of the Dirac crossings even in the presence of SOC [101]. The authors then proposed that the orthorhombic AFM semimetals CuMnAs and CuMnP could be material realizations of such AFM Dirac semimetals with very few band crossing at the Fermi level.

CuMnAs has two polymorphs and both of them are proposed to show non-trivial topology; a tetragonal (TET) phase which crystalizes in the space group $P4/nmm$, and an orthorhombic (ORT) phase crystalizing in the $Pnma$ space group. The TET phase consists of alternating layers of edge-sharing $CuAs_4$ and $MnAs_4$ tetrahedra. It has been proposed to have favorable applications in spintronics [102, 103] and to feature a topological metal-insulator transition driven by the Néel vector [104]. The ORT phase consists of a 3D network of edge-sharing $CuAs_4$ and $MnAs_4$ tetrahedra, where the Mn atoms form a 3D distorted hon-

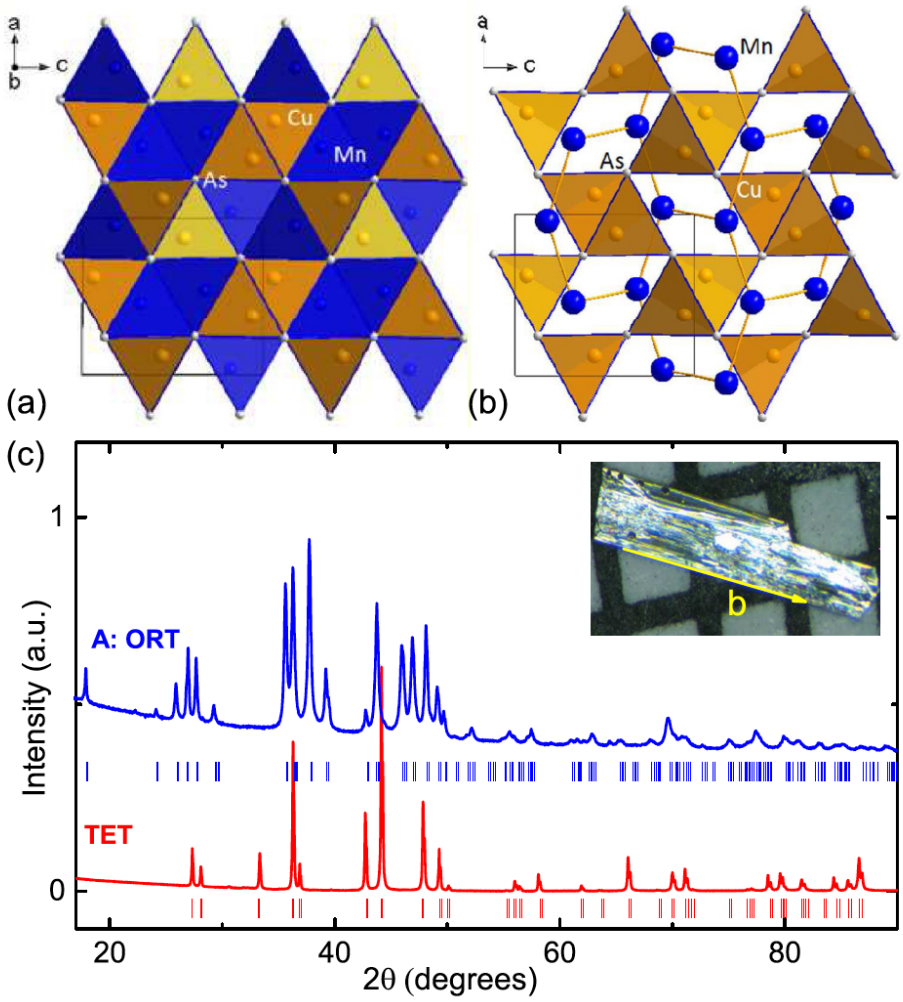

Figure 5.1: (a),(b) Crystal structure of ORT CuMnAs. (a) $CuAs_4$ (orange) and $MnAs_4$ (blue) tetrahedral building blocks. (b) The distorted Mn honeycomb lattice (Mn in blue). (c) Powder x-ray diffraction patterns of ORT (pulverized single crystals from batch A) and TET (from powder synthesis) phases. Ticks indicate the Bragg peak positions. Inset: A picture of an ORT single crystal against a mm sized grid. The as-grown surface is the bc plane.

eycomb lattice, as shown in Figs. 5.1(a) and 5.1(b). This space group has many symmetries that can be generated by a combination of 3 key symmetries; inversion $\mathcal{P}$, the gliding mirror reflection of the y-plane R_y, and the two-fold screw rotation about the z-axis S_{2z}.

The predicted, most energetically favorable AFM structure of ORT CuMnAs is shown in Figs. 5.2(a) and 5.2(b). The magnetic moments of the Mn atoms related by inversion symmetry are in opposite directions; this means that although $\mathcal{P}$ and $\mathcal{T}$ are broken, $\mathcal{PT}$ is preserved. In the absence of SOC, multiple band crossings are predicted along high-symmetry lines, as shown in Fig. 5.2(d). When SOC is taken into account in the first-principles calculations, the presence of the crossing points depends on the orientation of the magnetic moments of the Mn atoms. The authors found that only when the moments were aligned along the z-axis, the S_{2z} symmetry was still preserved, leading to the protection of the four-fold degenerate band crossing points along the X-U line, and the gapping of the rest as shown in Figure 5.2(d).

Although the physical properties of the polycrystalline ORT CuMnAs have already been studied [100], neither single crystals nor the magnetic structure determination of the ORT phase have been made before. Both are crucial for symmetry analysis and further investigation by ARPES and STM techniques to understand the topology of the material. In this chapter I will discuss the characterization of Cu_xMn_yAs single crystals, including the experimental determination of their magnetic structure using neutron-diffraction experiments. As expected from the theoretical prediction, we confirmed that the $\mathcal{P}$ and $\mathcal{T}$ symmetries were broken, but their combination $\mathcal{PT}$ was preserved. However, we found that the experimentally determined magnetic order breaks the S_{2z} symmetry, and thus massless Dirac fermions are no longer robust. First-principles calculations taking into account the observed magnetic structure showed that ORT CuMnAs can host an interesting topological phase with spin-polarized surface states, which could be promising for spintronics applications.

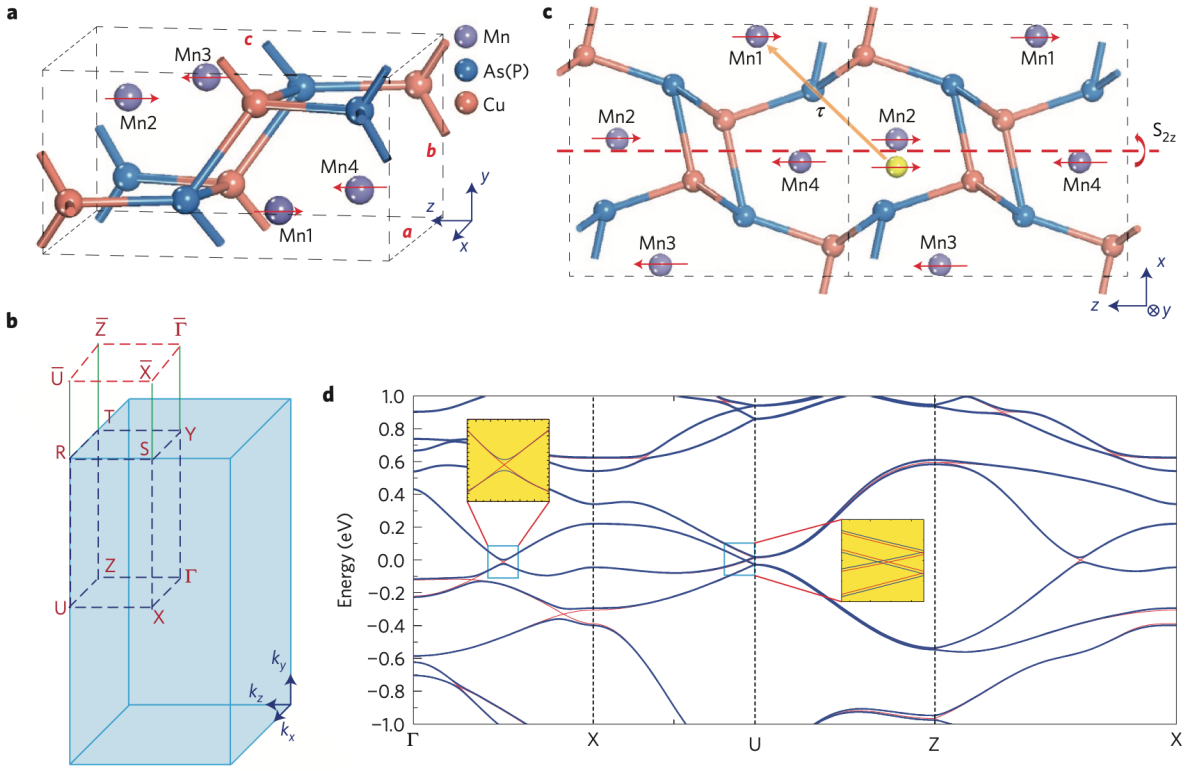

Figure 5.2: Taken from [101]. (a) The crystal structure of the orthorhombic CuMnAs(P), with red arrows showing the orientations of the magnetic moments of the Mn atoms. (b) The Brillouin zone of CuMnAs(P) and its projection on the (010) surface. (c) Illustration of the screw rotation symmetry S_{2z}. The red dashed line corresponds to the rotation axis, and the yellow circle corresponds to the Mn atom that the orange arrrow is pointing at, after the rotation about the z axis (C_{2z}) and a half translation along the (101) direction (τ=(1/2,0,1/2)). (d) The electronic structure of CuMnAs along high-symmetry lines in the presence (blue) and absence (red) of SOC. The magnetic moments of the Mn atoms are predicted to be along the z direction. The insets (yellow boxes) show the details of the band crossings near the Fermi level, which has been set to zero.

5.1.1 Single crystal growth of CuMnAs

Cu_xAs_yMn has two polymorphs; a tetragonal (TET) phase and an orthorhombic (ORT) phase. Using the solid state reaction technique, we determined that stoichiometric or slightly less As leads to the ORT CuMnAs phase, while 6 % of extra As results in the TET phase and a slight amount of MnAs. We did not further characterize or try to synthesize TET single crystals, but focused on studying the ORT phase.

Single crystals in the ORT phase were grown using Bi as the flux [105]. Cu shots, Mn granules, As and Bi chunks were mixed together and placed inside a 5-ml alumina crucible. The alumina crucible was then placed inside an evacuated quartz tube with 1/3 atm of Ar gas. The ampoule was subsequently heated to 1100 ^{o}C for 3 h, cooled to 850 ^{o}C in 2 h and then cooled to 400 ^{o}C at a rate of 3 ^{o}C/h. To investigate the effect of annealing, some batches were annealed at 400 ^{o}C for 24 h before the single crystals were separated from the flux using a centrifuge. Several different nominal compositions were attempted, as shown in Table 5.1 as we discovered a remarkable sensitivity of the magnetic properties on the composition, which will be discussed in more detail in the relevant chapter. We anticipated that the stoichiometry and site mixing of Cu and Mn might be difficult to control as several off-stoichiometric compounds, such as ORT $CuMn_3As_2$ and $Cu_2Mn_4As_3$ had already been discovered [105]. A picture of a typical CuMnAs single crystal is shown in Figure 3.2 (b). The crystals have a rectangular plate-like growth habit, with a typical thickness of 0.07mm. The as-grown surface corresponds to the *bc* plane. Powder diffraction data for both the ORT and TET phases are shown in Figure 5.1 (c), with the vertical lines corresponding to the respective Bragg peak positions.

Collaborative single crystal x-ray diffraction was performed on CuMnAs single crystals. It was used to determine the stoichiometry of batches A and B (see Table 5.1), which will be referred to as PA and PB and studied in detail using resistivity, magnetization, specific heat and neutron diffraction measurements. Five different structural models were used in the refinement. Model I assumes vacancies on both Cu and Mn sites. Model II assumes Mn on Cu sites. Model III assumes Cu on Mn sites. Model IV assumes Cu vacancy and Cu on Mn sites.

Batch	Cu: Mn: As: Bi
A	1 : 1 : 0.9 : 12
B	1 : 1 : 1 : 12
C	1 : 1 : 1.1 :12
D	0.9 : 1 : 1 : 12
E	1.1 : 1 : 1 : 12

Table 5.1: Synthesis details of Cu_xMn_yAs single crystals

Model V assumes Mn vacancies and Mn on Cu sites. Using single-crystal x-ray diffraction data, we found that Models I, II, and III resulted in the best refinements. Combined with the SEM-EDX data, from which we determined a concentration of $Cu_{0.98(3)}Mn_{0.98(4)}As_{1.02(4)}$ for both PA and PB, we concluded that both site vacancies and site disorders are present in both batches. Tables 5.2 and 5.3 summarize the refined crystal structure, atomic positions, and site occupancies of PA and PB. The major difference between the two is the exact stoichiometry. PA has fully occupied Mn sites with 5.0(2)% of Cu site vacancies, leading to a chemical formula of $Cu_{0.95}MnAs$, while PB has vacancies in both Cu and Mn sites and a chemical formula of $Cu_{0.98}Mn_{0.96}As$. For the rest of this chapter, $Cu_{0.95}MnAs$ will be denoted as PA and $Cu_{0.98}Mn_{0.96}As$ as PB. The differences in the physical properties between PA and PB most likely arise from the different stoichiometries of the Mn and Cu sites. It is worth noting that due to the similar atomic numbers of Cu and Mn, it is difficult to extract reliable information on the Cu/Mn site disorder using only single-crystal x-ray-diffraction data. Therefore, collaborative single-crystal neutron-diffraction data were also used to investigate the extent of Cu/Mn site mixing. Taking into account the number of vacancies revealed by single-crystal x-ray diffraction, the refinement of the neutron-diffraction data suggests 6% of site disorder in PB and 5% of site disorder in PA.

Table 5.2: Single crystal crystallographic data of PA and PB in the ORT *Pnma* space group at 300 K.

CuMnAs	PA	PB
F.W. (g/mol)	190.22	190.05
$a(\mathring{A})$	6.5716(4)	6.5868(4)
$b(\mathring{A})$	3.8605(2)	3.8542(3)
$c(\mathring{A})$	7.3047(4)	7.3015(5)
$V(\mathring{A}^3)$	185.32(2)	185.36(6)
No. reflections; R_{int}	1624;0.0210	2189;0.0304
R_1; wR_2	0.0172; 0.0342	0.0227; 0.0459
Goodness of fit	1.154	1.047

Table 5.3: Atomic coordinates and equivalent isotropic displacement parameters of PA and PB at 300 K. U_{eq} is defined as 1/3 of the trace of the orthogonalized U_{ij} tensor ($\mathring{A}^2$) and SOF stands for site occupancy factor.

Atom	Site	SOF	x	y	z	U_{eq}
PA: $Cu_{0.95}MnAs$						
Cu	4c	0.950(2)	0.37684(6)	1/4	0.05894(5)	0.0120(1)
Mn	4c	1	0.46024(7)	1/4	0.67737(6)	0.0121(2)
As	4c	1	0.25394(4)	1/4	0.37525(4)	0.0080(1)
PB: $Cu_{0.98}Mn_{0.96}As$						
Cu	4c	0.977(3)	0.3770(1)	1/4	0.0590(1)	0.0120(2)
Mn	4c	0.964(4)	0.4589(1)	1/4	0.6773(1)	0.0122(2)
As	4c	1	0.2544(1)	1/4	0.3754(1)	0.0079(1)

5.2 Electrical transport and thermodynamic properties

The resistivities of the ORT single crystals were typically around a few tenths of mΩ· cm and showed metallic behavior. Resistivity measurements were performed on crystals from all the batches shown in Table 5.1, and we observed two distinct behaviors; some of the crystals showed two transitions, whereas others only one. Figures 5.3(a) and 5.3(b) show the normalized resistivity, ρ(T)/ρ(400 K), of piece A (PA) from batch A and piece B (PB) from batch B. The resistivities of crystals from batches C-E can be found in Appendix A. Figure 5.3(a) shows only one resistivity drop in PA, suggesting the existence of one phase transition. The derivative of the resistivity, dρ/dT, shows a sharp peak at 360 K. On the other hand, PB shows two slope changes in the resistivity, suggesting the occurrence of two successive phase transitions. The dρ/dT plot indicates that one transition appears around 320 K and the other occurs around 230 K. The quality of the single crystals is clearly very sensitive to the nominal concentration of Cu/Mn/As. If we take the resistivity of the polycrystalline CuMnAs as an indicator of the quality of the sample, we can see that only when the starting As concentration is slightly less than the stoichiometric concentration (batch A), do the resulting single crystals show only one resistivity slope change around 360 K. This is similar to what was observed in polycrystalline CuMnAs, whose composition was verified by EDS measurements to have a 1:1:1 ratio. Even for batch E where only one transition was observed, it was found to occur around 300 K, which is 60 K lower than the one in the polycrystalline sample, suggesting poorer sample quality or deviation from the stoichiometric composition.

The inset of Figure 5.3(a) shows the field-dependent Hall resistivity ρ_{yx}(H) of PA at 2 and 100 K. Its positive sign indicates that holes dominate the transport, and the linear field dependence suggests that the single-band model can be used. Using equation 2.38, we estimated the carrier density to be $\approx 6.5 \times 10^{20}$ cm^{-3}. This value is significantly greater than that of the Dirac semimetals Cd_3As_2 [16], Na_3Bi [91], and the Weyl semimetal TaAs [85], but comparable to that of the Dirac nodal-line semimetal candidates ZrSiSe [80] and CaAgAs [1].

The temperature-dependent susceptibility [M/H(T)] and heat capacity [C_p(T)] of PB are presented in Figs. 5.3(c) and 5.3(d). Two slope changes can also be observed in the

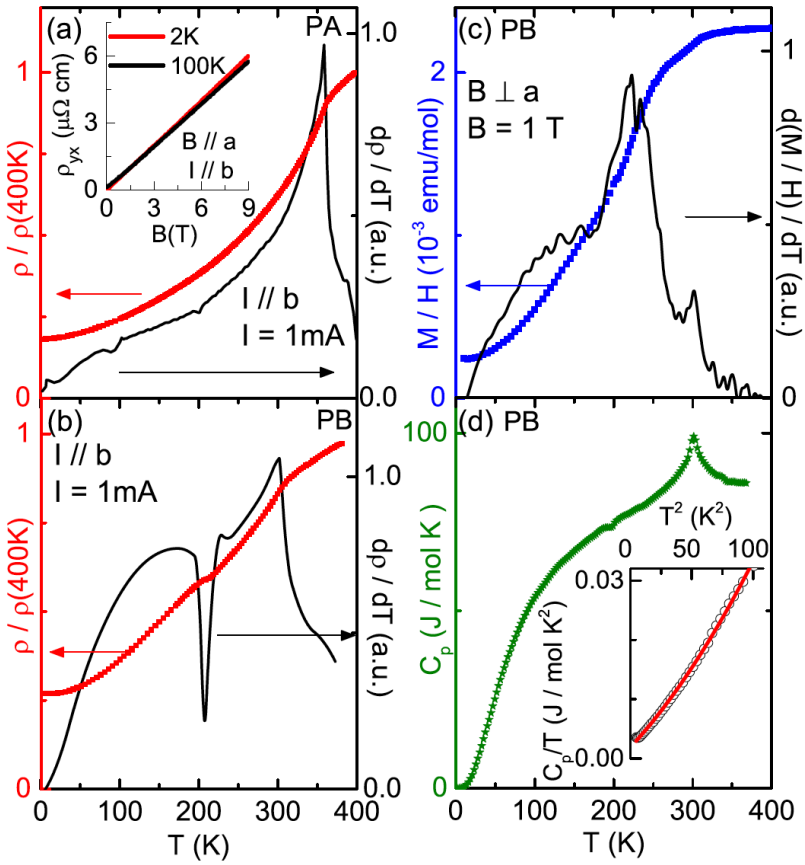

Figure 5.3: PA: (a) Normalized resistivity ρ(T)/ρ(400 K) and its derivative dρ/dT vs T .Inset: Hall resistivity ρ_{yx} vs T. PB [(b)–(d)] (b) Normalized resistivity ρ(T)/ρ(400 K) and dρ/dT vs T.(c) Susceptibility M/H and d(M/H)/dT vs T.(d) Heat capacity C_p vs T.Inset: C_p/T vs T^2.

M/H(T) data, which can be clearly seen in $d(M/H)/d$T. From 300 K to 400 K, the highest temperature we were able to measure, the magnetic susceptibility is almost temperature independent, showing no Curie-Weiss behavior. The specific heat shows only one heat-capacity jump around 320 K without any anomaly at 230 K, suggesting that the phase transition at 230 K is most likely a transition between two ordered phases. Since both phase transitions are at high temperatures, we were able to fit the C_p/T data from 2 to 10 K using equation

$$C_p = \gamma T + \alpha T^3 + \beta T^5, \tag{5.1}$$

where the first term refers to the electronic heat capacity and the rest to the low-temperature lattice heat capacity. We deduced a Sommerfeld coefficient $\gamma = 1.88$ mJ mol^{-1} K^{-2} which indicates a small density of states at the Fermi level for the ORT CuMnAs.

5.3 The magnetic structures of PA and PB

Neutron-diffraction experiments were also performed to elucidate the nature of the observed phase transitions. Figure 5.4(a) presents the rocking curve scan at (1,1,0) on PA. A large peak is observed at 150 K, but is absent at 400 K, indicating the presence of AFM order at 150 K. The onset of the increase in the (1,1,0) peak intensity agrees well with the peak in dρ/dT , as shown in Figure 5.4(b). This second order paramagnetic to antiferromagnetic phase transition, that can be fit by the power law

$$I(T)/I_0 = [M(T)/M_0]^2 = A + (1 - T/T_N)^{2\beta} \tag{5.2}$$

where M_0 is the saturation moment. Using $T_N = 360$ K, the critical exponent is $\beta = 0.35(3)$, which suggests the breakdown of the mean-field theory ($\beta = 0.5$) and thus a strong spin fluctuation near T_N. The magnetic and nuclear structure of $Cu_{0.95}MnAs$ was refined using 76 effective magnetic reflections. $P_{n'ma}$ is the only magnetic symmetry that can fit the data. The R factor was 0.0508 and the goodness of fit 6.08. The refined propagation vector **k**=0 indicates that the unit cell of magnetic structure coincides with that of the crystal structure, leading to commensurate antiferromagnetism (CAFM). Figures 5.4(c) and 5.4(d)

show the refined CAFM structure. Mn spins sit on a distorted honeycomb sublattice and order parallel to each other along the b axis [Figure 5.4(c)] with the nearest-neighboring spins antiferromagnetically aligned to each other [Figure 5.4(d)]. This magnetic structure is the same as the one proposed theoretically by Tang et al., but with the spin orientation along the b, instead of the c axis. The refined magnetic moment at 150 K is 4.0(1) μ_B/Mn.

To elucidate the difference in the magnetic structures between PA and PB, neutron diffraction measurements were also performed on PB. The (1,1,0) peak is not allowed by the crystal structure symmetry in the ORT CuMnAs phase, and the small, nonzero intensity we observed above 320 K is due to the half-wavelength ($\lambda/2$) contamination of the neutron beam [64]. The wavelength of 1.546Å we used at HB3A is selected by the Si-220 monochromator, which also picks the half-wavelength neutrons that make up 1.4% of the main beam flux at HB3A. In Figure 5.5 (a), magnetic satellite peaks begin to appear near (1,1,0) as the sample is cooled below 320 K, suggesting incommensurate antiferromagnetism (ICAFM) [106]. Figure 5.5 (c) shows a cut in the (hk0) plane at 227 K. We can clearly detect the three peaks shown in Figure 5.5 (a). The concentration of points at (0.9,1,0) and (1.1,1,0) indicates the presence of the incommensurate magnetic peaks, that can be indexed by the incommensurate propagation vector $\mathbf{k} = (0.1,0,0)$. Upon further cooling of the sample below 230 K, we observe that both the (0.9,1,0) and (1.1,1,0) peak intensities decrease while the (1,1,0) peak intensity starts to increase, indicating a competition between the CAFM with the propagation vector $\mathbf{k} = 0$ and ICAFM. Below 190 K, both (0.9,1,0) and (1.1,1,0) peaks have almost completely diminished while the (1,1,0) peak keeps increasing, suggesting the disappearance of ICAFM.

To better visualize the competition and coexistence between these two phases, Figure 5.5(d) shows the (0.9,1,0) and (1,1,0) peak intensities and dρ/dT as a function of temperature. We can see that $Cu_{0.98}Mn_{0.96}As$ undergoes a second-order paramagnetic (PM) to ICAFM phase transition at 320 K as well as a second-order ICAFM to CAFM phase transition at 230 K. ICAFM competes and coexists with the CAFM phase between 230 and 190 K and disappears below 190 K. Based on an analysis of 102 effective magnetic peaks, the refined CAFM structure is the same as the one in $Cu_{0.95}MnAs$ [Figures 5.4 (c) and 5.4 (d)]

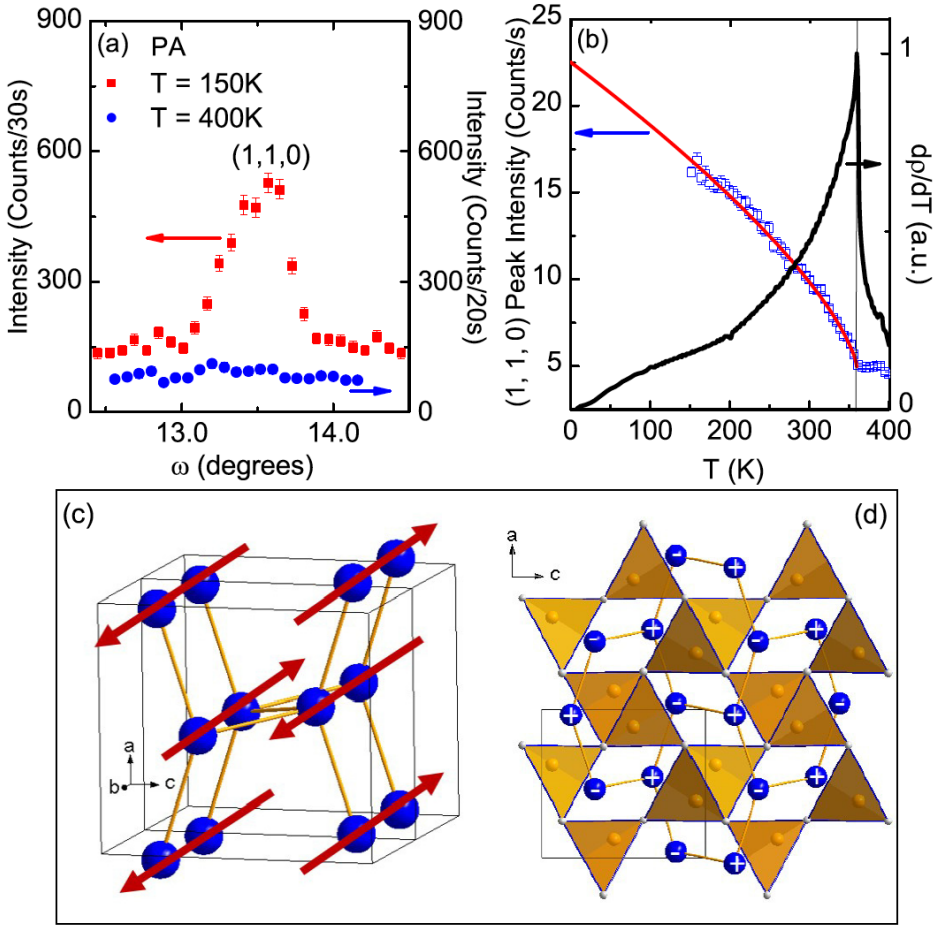

Figure 5.4: (a) The (1,1,0) intensity vs ω for PA. (b) A comparison between the (1,1,0) peak intensity and the dρ/dT vs T. The red line corresponds to the power-law fit. (c) Magnetic structure of PA in the CAFM state. Only the Mn sublattice is shown. (d) The view of the magnetic structure from the b direction. Mn atoms are shown in blue. "+" denotes spins pointing out of plane while "-" denotes spin pointing in plane.

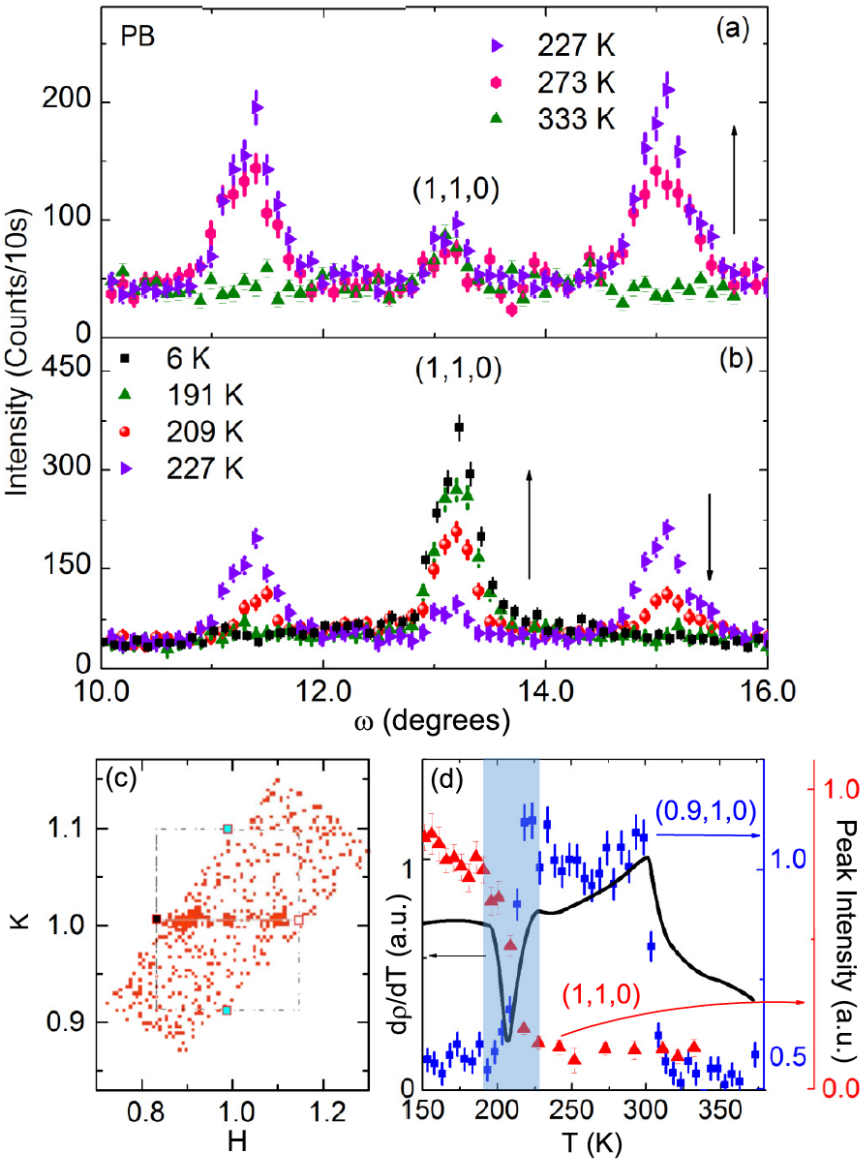

Figure 5.5: (a),(b) Intensity vs ω for PB. The black arrows indicate the trend of the peak intensity with decreasing temperature. (c) A cut of the neutron scattering in the $hk0$ plane. (d) A comparison between the (0.9,1,0) peak intensity and dρ/dT vs T . The light blue box marks the temperature region where CAFM and ICAFM compete and coexist.

with a refined magnetic moment at 6 K of 4.3(2) μ_B/Mn and an R factor of 0.0555. The moment is smaller than 5 μ_B/Mn, the theoretical saturation moment for Mn^{2+}.

5.4 Bulk band structure calculations with experimentally determined magnetic structure

Based on the magnetic structure and easy axis determined experimentally, in order to explore the electronic and topological properties of ORT CuMnAs with the magnetic moments oriented along the b axis, we recalculated its bulk band structure and the (010) surface states. Although no chemical disorder or vacancies are considered in the DFT calculation, since the material still holds the translational symmetry and maintains the ORT structure, the electronic structure and surface states shown in Figure 5.6 should capture the main features. Due to the presence of the $\mathcal{PT}$ symmetry in the experimentally determined CAFM phase, every bulk state is doubly degenerate. Furthermore, band inversion still occurs in this system, thus the nontrivial topological properties can still appear. Because the CAFM order breaks the nonsymmorphic gliding symmetry R_y and screw symmetry S_{2z}, in contrast to the case with spin orientation along the c axis [101], now the gapless coupled Weyl fermions disappear and the Dirac nodal line becomes fully gapped everywhere by SOC in the bulk Brillouin zone, as shown in Figure 5.6 (a). As shown in Figure 5.6 (b), the band gap induced by SOC along the ΓX line is only 7 meV. Figure 5.6(c) shows the spin-polarized surface states emerging from the gapped bulk states [Figures 5.6 (d) and 5.6 (e)] on the (010) side surface. Due to the absence of rotational symmetries on the (010) surface, the Fermi-surface contour at the Fermi level is asymmetric, and the spin-polarized surface states are gapped. Because the bulk Dirac fermions in this case are massive and the time-reversal symmetry is broken, the fluctuations could resemble the dynamical axion field, which gives rise to exotic modulations of the electromagnetic field showing a similar signature to axion insulators [107].

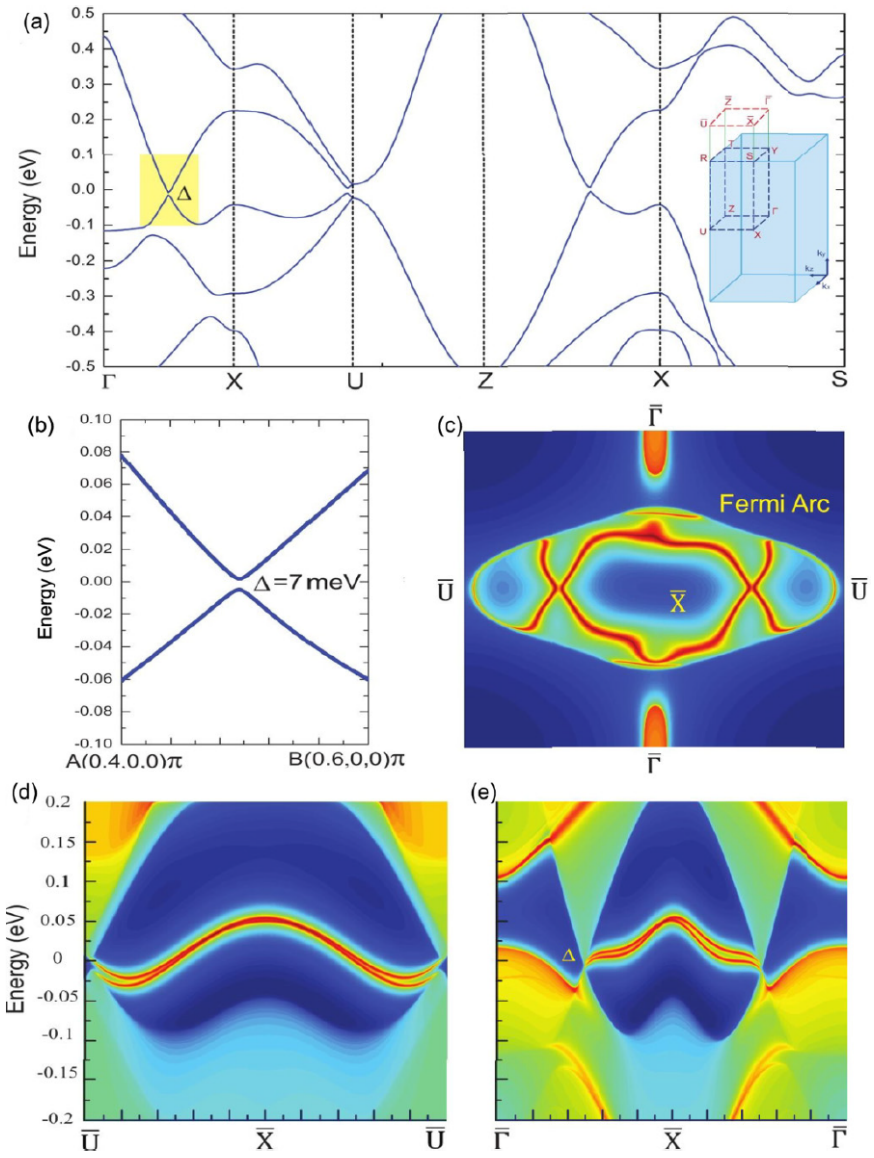

Figure 5.6: (a) Calculated band structures of the ORT CuMnAs with SOC and the magnetic structure shown in Figure 5.4 (c). The inset shows the Brillouin zone and its projection to the (010) surface. Δ is the band gap of a massive topological fermion along ΓX line. (b) The detail of the band structure marked by the yellow box in (a). (c) Fermi-surface contour on the (010) surface at the calculated Fermi level. Corresponding electronic spectra along (d) $\bar{k}_x = \pi/a$ and (e) $\bar{k}_z = 0$. The Fermi level is set to zero.

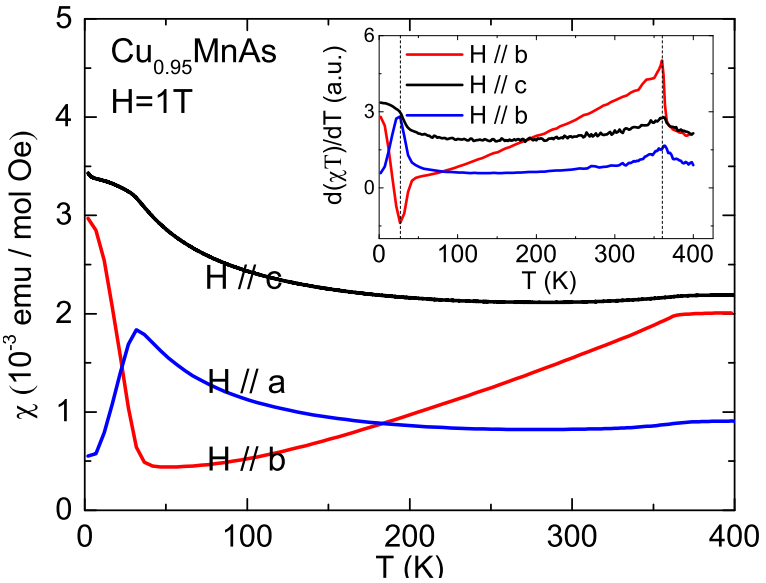

Figure 5.7: Temperature dependence of the susceptibility χ of $Cu_{0.95}MnAs$ with a magnetic field of 1 T, applied parallel to the a, b and c axes. Inset: The derivative of the quantity χ T with respect to temperature. The dashed lines indicate the transition temperatures.

5.5 Spin-flop transition in the orthorhombic antiferromagnetic topological semimetal $Cu_{0.95}MnAs$

This section has been adapted from [4].

AFM materials had originally been dismissed as candidates for spintronics devices because they have no net magnetic moment. However, it was eventually realized that antiferromagnets actually have many characteristics that make them suitable for spintronics; they are insensitive to magnetic field perturbations, do not generate stray fields and have faster spin dynamics than ferromagnets since their resonant frequencies are higher [108, 109]. Since our study suggests that ORT CuMnAs can be a promising material for AFM spintronics, its magnetic properties deserve further investigation. In this section I will discuss the observation of a spin-flop transition in $Cu_{0.95}MnAs$, and its absence in $Cu_{0.98}Mn_{0.96}As$, through a thorough study of their magnetic susceptibility and magnetoresistance, and present a magnetic phase diagram for $Cu_{0.95}MnAs$.

Figure 5.7 shows the temperature-dependent magnetic susceptibility χ of $Cu_{0.95}MnAs$ under a magnetic field of 1 T, applied parallel to the a, b and c axes. $Cu_{0.95}MnAs$ undergoes a temperature induced second-order paramagnetic (PM) to AFM phase transition at 360 K and the effect of the transition is most pronounced when H // b, as the susceptibility begins to decrease dramatically below this temperature. With H // a and H // c, χ shows much smaller change across 360 K, which can be seen more clearly in the d(χ T)/dT plot shown in the inset of Figure 5.7. This suggest that the magnetic easy axis for $Cu_{0.95}MnAs$ is the b axis, consistent with our neutron diffraction results. No Curie-Weiss behavior is observed up to 400K.

As the sample is further cooled, a second anomaly is observed around 27 K. In contrast to the high temperature transition, the susceptibility with H // a, starts decreasing sharply, while increasing in the other two directions. For H // b the increase is dramatic; the susceptibility at 2 K is more than twice as large as that at 30 K. This transition can also be clearly seen in the inset of Figure 5.7.

To investigate the nature of the low temperature transition, we measured the isothermal magnetization and magnetoresistance of $Cu_{0.95}MnAs$ with H // b for temperatures between 2 K and 100 K, as shown in Figure 5.8. A metamagnetic phase transition, which broadly refers to the abrupt increase of the magnetization with applied magnetic field, can be seen very clearly as a sharp upturn in the isothermal magnetization up to 100 K, as shown in Figure 5.8 (a). The critical field H_{SF}, defined here as the maximum of dM/dH, increases with increasing temperature, as shown in Figure 5.8 (c). This behavior suggests a spin-flop transition, which was first experimentally observed in $CuCl_2 \cdot H_2O$ single crystals [110], and has since also been observed in many other systems with magnetocrystalline anisotropy [111–117]. In a spin-flop transition with weak magnetocrystalline anisotropy, when a magnetic field is applied parallel to the magnetic easy axis of a material and exceeds a critical value H_{SF}, the antiferromagnetic spins try to align perpendicular to the magnetic field, and this results in a net moment along the easy axis [118]. Upon further increasing the field, the net moment grows until saturation. The spin-flop transition takes place because the total energy of the system is a sum of the

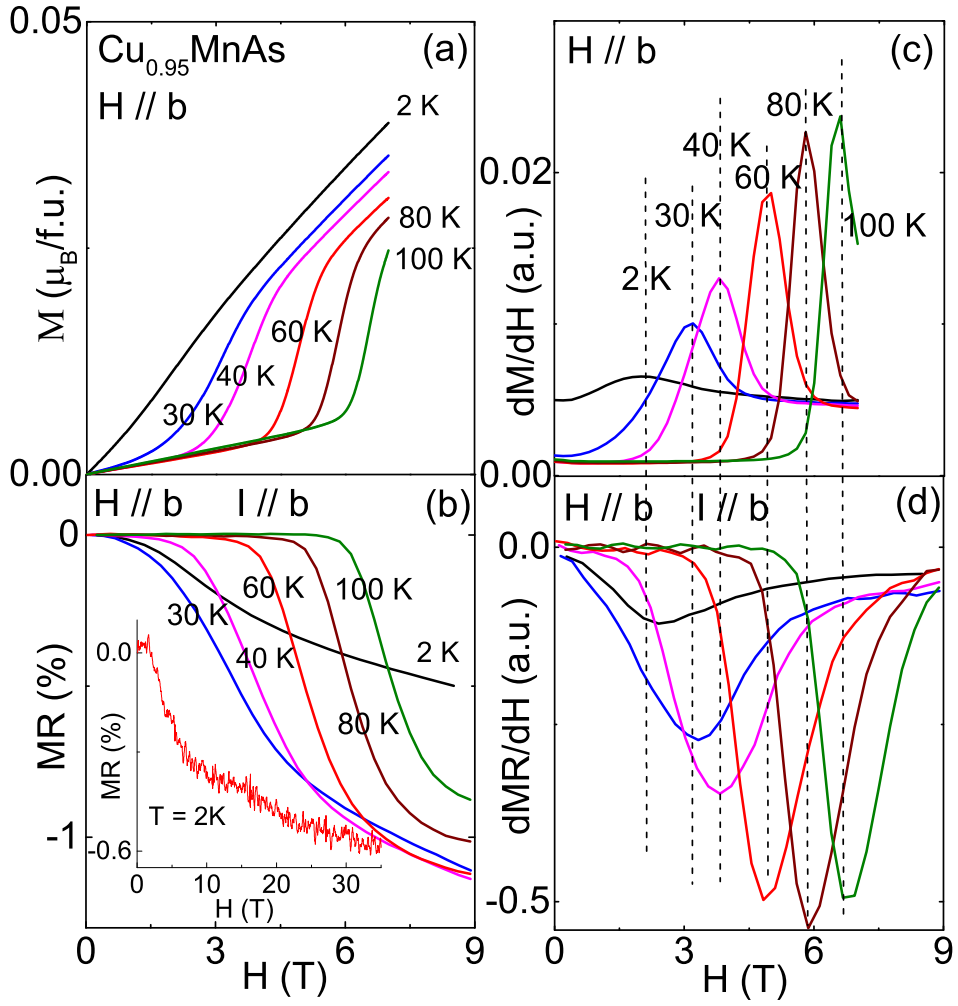

Figure 5.8: (a) The magnetization, M, of $Cu_{0.95}MnAs$ at several temperatures for H // *b*. (b) The magnetoresistance, MR, of $Cu_{0.95}MnAs$ at several temperatures, for H // *b* and I // *b*. Inset: The MR for for fields up to 35 T. (c)-(d) The derivatives of M and MR with respect to H. The dashed lines go through the peaks of the derivatives, which is the criterion we used to determine the transition temperatures.

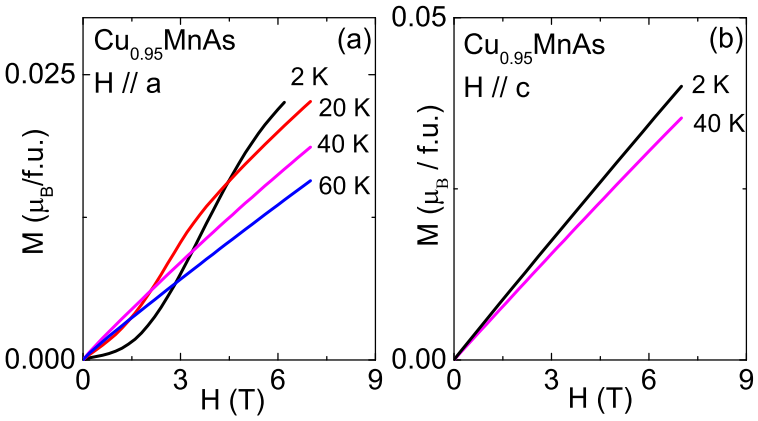

Figure 5.9: (a) The field dependence of the magnetization of $Cu_{0.95}MnAs$ for 2 K, 20 K, 40 K and 60 K with the field parallel to a. (b) The field dependence of the magnetization of $Cu_{0.95}MnAs$ for 2 K and 40 K with the field parallel to c.

Zeeman energy of each magnetic sublattice and the magnetic anisotropy energy. At low fields the AFM configuration is the ground state, but above H_{SF}, it is the spin-flop state with spins almost perpendicular to the field that minimizes the energy [51].

No hysteresis is observed in Figure 5.8 (a), as is the case for most AFM materials with spin-flop transitions. The spin-flop transition had been considered to be first-order, despite the fact that no hysteresis has been been observed experimentally. Hysteresis loops are an experimental hallmark of first-order transitions, and its absence in spin-flop transitions has been attributed to low magnetic anisotropy, but the nature of the transition has more recently been challenged [119]. No saturation is observed up to 7T for $Cu_{0.95}MnAs$, which indicates that the system remains in the spin-flop state without saturation up to 7 T. This is consistent with the fact that the maximum magnetic moment at 2 K and 7 T is just 0.04 μ_B / f.u., much smaller than the saturation moment of Mn^{2+}.

The spin-flop transition can also be clearly seen in the isothermal magnetoresistance data, shown in Figure 5.8 (b). Associated with the transition is a sharp drop in the magnetoresistance to about -1% at 9 T, suggesting the loss of spin scattering above H_{SF}, which is consistent with the spin-flop transition scenario. The inset of of Figure 5.8 (b) shows the magnetoresistance measured up to 35 T at 2 K. The magnetoresistance decreases lin-

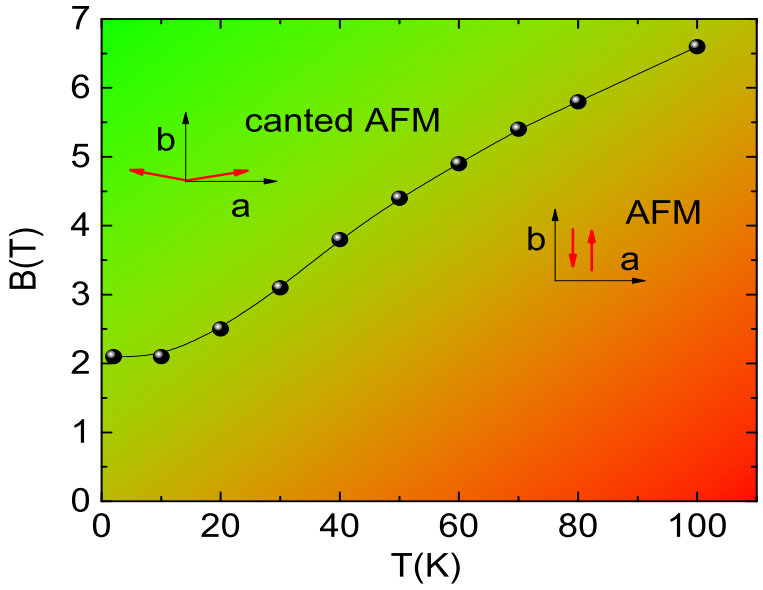

Figure 5.10: The magnetic phase diagram of $Cu_{0.95}MnAs$ with the field parallel to the b axis.

early with field above 9 T, suggesting that the system remains in the spin-flop state up to 35 T without saturation. The critical fields in both measurements are in very good agreement, as seen in Figures 5.8 (c) and 5.8 (d), which show the derivatives of the isothermal magnetization and magnetoresistnace respectively. The small mismatches can ascribed to misalignment between the magnetic field direction and the magnetic easy axis.

To further investigate the magnetic anisotropy, the isothermal magnetization of $Cu_{0.95}MnAs$ with H // a and H // c was measured and is shown in Figures 5.9 (a) and (b), respectively. With H // a, the isothermal magnetization shows a metamagnetic transition below 30 K, while linearly increasing with field above 30 K. This is in sharp contrast to what we observe when H // b, where the metamagnetic transition can be observed even at 100 K. When the field is parallel to the c direction, the magnetization remains linear with field at both 2 K and 40 K up to 7 T, showing no sign of a metamagnetic transition. This behavior suggests that the b axis is the easy axis and c the hard axis.

Based on our observations, we propose that this spin-flop transition results in a canted antiferromagnetic state when a small magnetic field is applied as shown schematically in

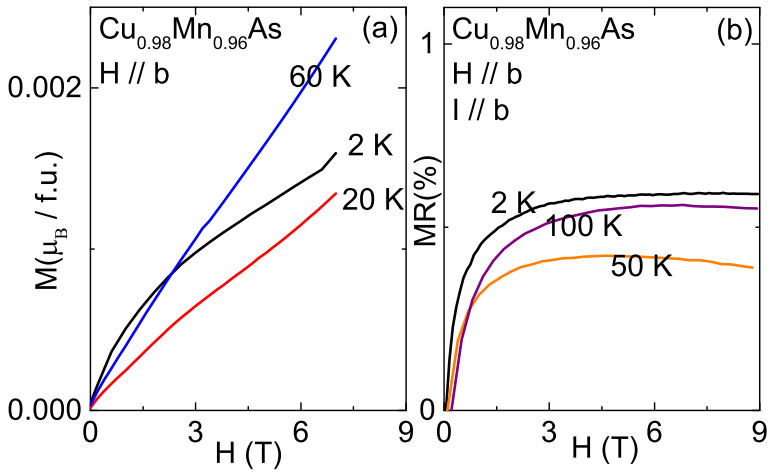

Figure 5.11: (a)-(b) The isothermal magnetization (a) and magnetoresistance (b) of $Cu_{0.98}Mn_{0.96}As$ for certain temperature values. The magnetic field was applied parallel to the b axis.

Figure 5.10. A proposed magnetic phase diagram for $Cu_{0.95}MnAs$, based on our results from magnetic susceptibility, magnetization and magnetoresistance with the field parallel to the easy axis is shown in Figure 5.10. The H_{SF} at each temperature was determined by the field at which the derivative had its maximum value. At high temperatures and below H_{SF}, the Mn spins are oriented along the b axis. Above H_{SF}, the magnetic structure consists of the Mn spins that have now flipped and form a small canting angle with the a axis that causes the magnetization to have a small component along the b axis. In the previous section, we suggested that in ORT CuMnAs, the magnetism is very sensitive to the Cu vacancies and Cu/Mn site mixing. while $Cu_{0.95}MnAs$ is a commensurate antiferromagnet below 360 K, $Cu_{0.98}Mn_{0.96}As$ enters an incommensurate antiferromagnetic state at 320 K and then a commensurate antiferromagnetic state below 230 K.

To further examine the effect of Cu vacancies and Cu/Mn site mixing on the spin-flop phase transition, we performed isothermal magnetization and magnetoresistance measurements on $Cu_{0.98}Mn_{0.96}As$. The data are summarized in Figures 5.11 (a) and (b). No sign of a spin-flop transition was observed. The field-dependent magnetization evolves from a convex shape at 2 K to linear behavior at 60 K, with no sharp upturn. The MR is positive

and quickly plateaus, reaching a maximum of 0.5%. We attribute the disappearance of the spin-flop transition to a few % of Cu vacancies or mixing with Mn atoms. Similar to what was discussed in the previous section, these findings confirm the sensitivity of the magnetic properties on defects or disorder in CuMnAs.

5.6 Conclusion

I discussed the synthesis and magnetic structure of ORT $Cu_{0.95}MnAs$ and $Cu_{0.98}Mn_{0.96}As$. While $Cu_{0.95}MnAs$ is a commensurate antiferromagnet below 360 K with a propagation vector of $\mathbf{k} = 0$, $Cu_{0.98}Mn_{0.96}As$ undergoes a second-order paramagnetic to incommensurate AFM phase transition at 320 K with $\mathbf{k} = (0.1,0,0)$, followed by a second-order incommensurate to commensurate AFM phase transition at 230 K. Neutron diffraction measurements revealed that when both compounds are in their commensurate AFM state, their distorted Mn honeycomb sublattice has Mn spins aligned antiparallel to each of their nearest neighbors with all spins parallel to the b-axis. We concluded that this magnetic structure breaks the S_{2z} symmetry, leading to the disappearance of Dirac fermions. Our first-principles calculations also showed that this magnetic order can support spin-polarized surface states, a much sought-after property for spintronics. Furthermore, we mapped out the $H - T$ phase diagram of $Cu_{0.95}MnAs$. A spin-flop transition at high temperatures and low fields with the field along the easy axis b is observed, leading to a canted AFM state with a small net moment along the b axis. On the other hand, in $Cu_{0.98}Mn_{0.96}As$ these transitions are absent, indicating that the magnetic interactions in this system are very sensitive to Cu vacancies and Cu/Mn site mixing.

CHAPTER 6

Fermiology and Type-I superconductivity in the chiral superconductor $NbGe_2$

This chapter is adapted from [5]

6.1 Introduction

A new addition to the class of topological semimetals are the Kramers-Weyl semimetals [50]. Topological insulators and semimetals are characterized by band crossings that are protected by crystalline or time-reversal symmetries. In nonmagnetic chiral crystals which only have pure rotational symmetries, spin-orbit coupling (SOC) splits the doubly degenerate bands everywhere except at the time-reversal invariant momenta (TRIMs), where the bands must remain doubly degenerate according to Kramers' theorem. These crossings are characterized by a quantized chiral charge and were thus termed Kramers-Weyl fermions [50].

$NbGe_2$, the subject of this chapter, was predicted to belong to this new class of Kramers-Weyl semimetals. Additionally, studies dating back to the 1970s found that it becomes superconducting (SC) at low temperatures, although the reported T_cs ranged from 2 K in single crystals to 16 K in sputtered films [120, 121]. In non-centrosymmetric superconductors (NCSs), the lack of an inversion center and the presence of antisymmetric spin-orbit coupling (ASOC) can lead to an admixture of spin-singlet and spin-triplet states [122]. Previously discovered NCSs exhibit a wide range of behaviors, with some showing evidence of unconventional SC [123] and others being fully gapped s-wave SCs [124]. The presence of nontrivial band topology coupled with superconducting properties make $NbGe_2$ a candidate for chiral

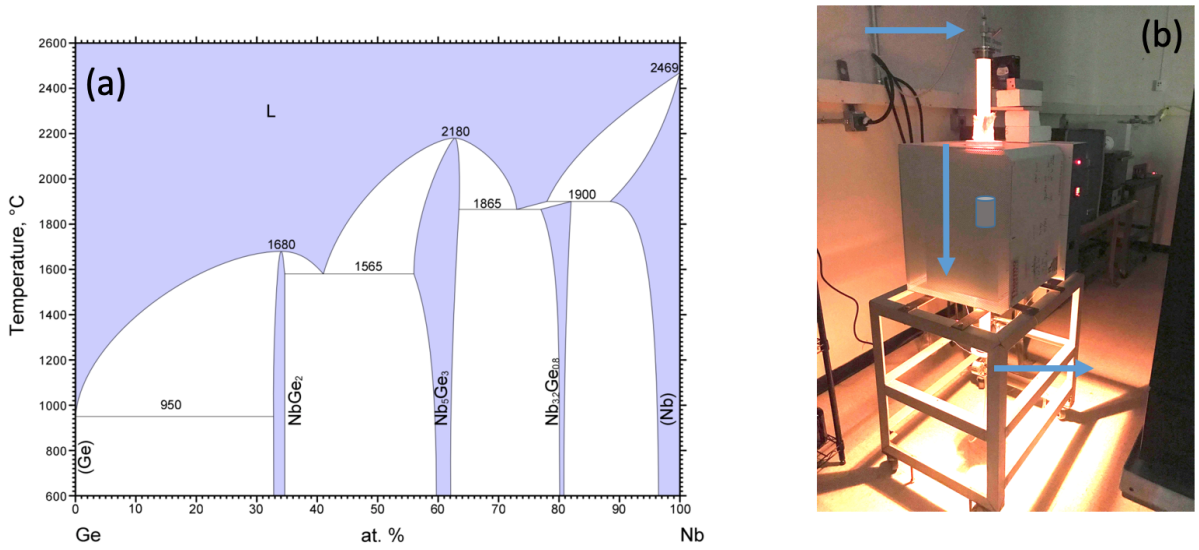

Figure 6.1: (a) The binary phase diagram of Nb-Ge. Taken from [125]. (b) A picture of the vertical tube furnace used for the synthesis of $NbGe_2$. Arrows indicate Ar flow, and the cylinder indicates the approximate location of the Ta tube.

topological SC.

In this chapter, I will present our results on the single crystal growth, thermodynamic, magnetotransport and torque measurements, as well as first principles calculations.

6.1.1 Single crystal growth of $NbGe_2$

$NbGe_2$ was synthesized using the self-flux method, with Ge as the flux. This was a particularly challenging growth because a small concentration of Nb becomes soluble in Ge only in temperatures above 1000 ^{o}C. Because the quartz tube which is used to protect the growth from air deforms at $\sim$ 1250 ^{o}C, a modified two-step process was used for the growth of $NbGe_2$ single crystals. A large alumina tube was placed inside a tube furnace capable of reaching 1500 ^{o}C, and the furnace was placed on its side with the alumina tube standing vertically on a metal support plate. Both ends of the tube were connected to an Ar gas cylinder using rubber tubing so that Ar gas can flow through the tube to prevent

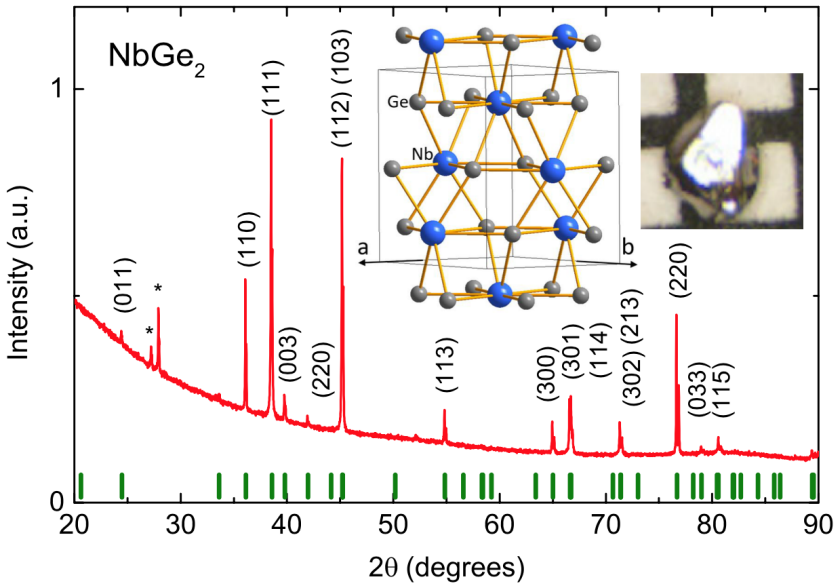

Figure 6.2: The x-ray powder diffraction pattern of $NbGe_2$, with indexed peaks. The peaks with asterisks are due to impurities, most likely due to Ge flux. The crystal structure and a picture of a single crystal against a mm background are shown as insets.

the oxidation of the growth ampoule. Enough firebrick was placed in the bottom half of the tube, so that the Ta tube could be placed on it. The exact position was determined after calibrating the furnace with a thermocouple. Nb powder was combined with Ge pieces at a molar ratio of 6:94 and placed inside alumina crucibles which were in turn placed in Ta tubes, which were evacuated and filled with some Ar gas before being sealed using an arc-welder. The Ta tubes were subsequently placed in the vertical one-zone surface that was flushed with Ar gas during the heat treatment, which consisted of quick heating to 1400 ^{o}C, dwelling for 2 hours, and then slowly cooling to 900 ^{o}C. At that point the furnace was shut down and allowed to cool to room temperature. The alumina crucible was finally retrieved from the Ta tube and placed in a quartz tube, which was placed into a pre-heated furnace at 960 ^{o}C for 30 minutes and then a centrifuge was used to separate the liquid from the single crystals. Small but thick three dimensional single crystals were obtained, as shown in Figure 3.2 (c).

$NbGe_2$ has a $CrSi_2$-type (C40) hexagonal noncentrosymmetric crystal structure with the

space group $P6_222$, as shown in the inset of Figure 6.2, where each Nb atom is covalently bonded to 6 Ge atoms that lie on the vertices of a hexagon in the ab plane and four Ge atoms out of plane. The powder diffraction shows that all peaks can be matched to the $NbGe_2$, except ones with the asterisks denoting impurity peaks.

6.1.2 Transport properties and Fermiology of $NbGe_2$

Figure 6.3 presents the temperature-dependent resistivity of $NbGe_2$ from 300 K to 2 K. The sample shows metallic behavior with a resistivity of 50 $\mu\Omega$·cm at room temperature and has a residual resistivity ratio (RRR), defined here as $\rho(300\text{ K})/\rho(2.2\text{ K})$, of 520. The high RRR and the sharp superconducting transition, shown in the inset of Fig. 6.3 are indicative of the high quality of the sample.

The Fermi surface of $NbGe_2$ was studied by measuring the angular dependence of the de Haas-van Alphen oscillations observed in torque. Figure 6.4(a) shows a contour plot of the frequencies obtained using a Fast Fourier Transform (FFT) as a function of angle. The measurement geometry is shown in the inset, and the data were collected at 5^o intervals. Three branches of dHvA frequencies (F_{dHvA}) were observed, which we assigned to three different Fermi pockets. The small difference in frequencies and similar angular dependence of α and α' suggest spin splitting of the electronic structure caused by ASOC. Since ASOC has the form of a Zeeman term but with a fictitious magnetic field that is momentum dependent, it lifts the two-fold spin degeneracy in noncentrosymmetric materials, resulting in a spin-split Fermi surface. This behavior has also been observed in other noncentrosymmetric materials such as VSi_2 [126], but was too small to be discerned in the chiral Weyl semimetal CoSi [127].

DFT calculations were performed to examine the Fermiology and compare with the experimental dHvA data. The orbital-projected electronic band structure of $NbGe_2$ obtained from DFT calculations along high symmetry directions with SOC considered is shown in Fig. 6.4(b). The different colors depict contributions from different orbitals while the size of the dots shows the actual contribution. It can be readily seen that several valence and conduction bands cross the Fermi energy, suggesting a metallic type behavior with the ma-

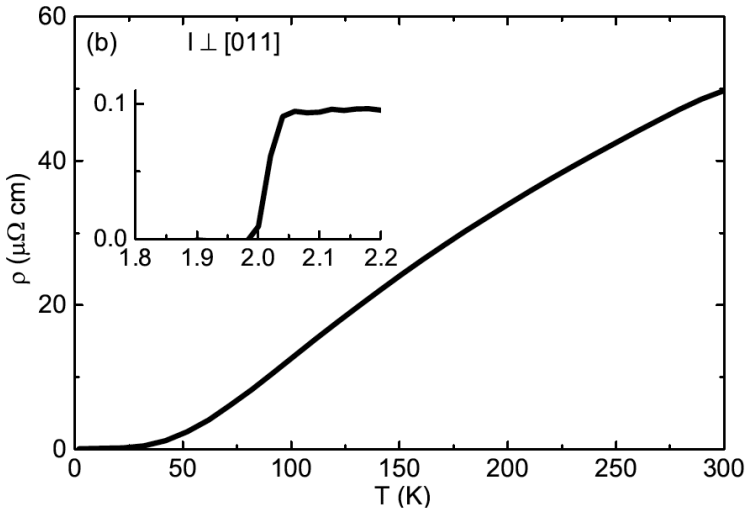

Figure 6.3: The resistivity of a $NbGe_2$ single crystal at 0 T. Inset: zoomed-in plot of the superconducting transition.

jor contributions to the band structure coming from the hybridization of the Nb$-4d$ and Ge$-4p$ orbitals around the Fermi energy. The band structure shows band splitting due to the breaking of spatial inversion symmetry everywhere except at the TRIMs (Γ, M, A, and L) of the BZ. Our calculation indicates that these gapless band crossings at the TRIMs marked by the red arrows in Fig. 6.4(b) are the Kramers-Weyl points, which is consistent with the recent publication [50]. The Weyl point at the high symmetry point M (≈ 0.05 eV) is close to the Fermi energy, and is expected to contribute relativistic electrons/holes near the Fermi level. Additionally, the band structure at M (≈ 0.05 eV) and H (≈ -0.05 eV) features a saddle-point-like dispersion near the Fermi level which eventually results in a Van Hove type singularity in the DOS at Fermi energy, which may be responsible for the observed SC.

The Fermi surface of $NbGe_2$ is shown in Fig. 6.4(c). Of the four Fermi pockets which comprise the Fermi surface, three are hole type (left panels) and one is electron type (right panel). With the magnetic field rotating away from the [011] axis and toward the a axis, we computed the frequencies F_{DFT} associated with the extremal cross sectional areas for all Fermi pockets and plotted them in Fig. 6.4(a) as black dots. Excellent agreement between F_{DFT} and F_{dHvA} is achieved in terms of both angular dependence and magnitude. We circled

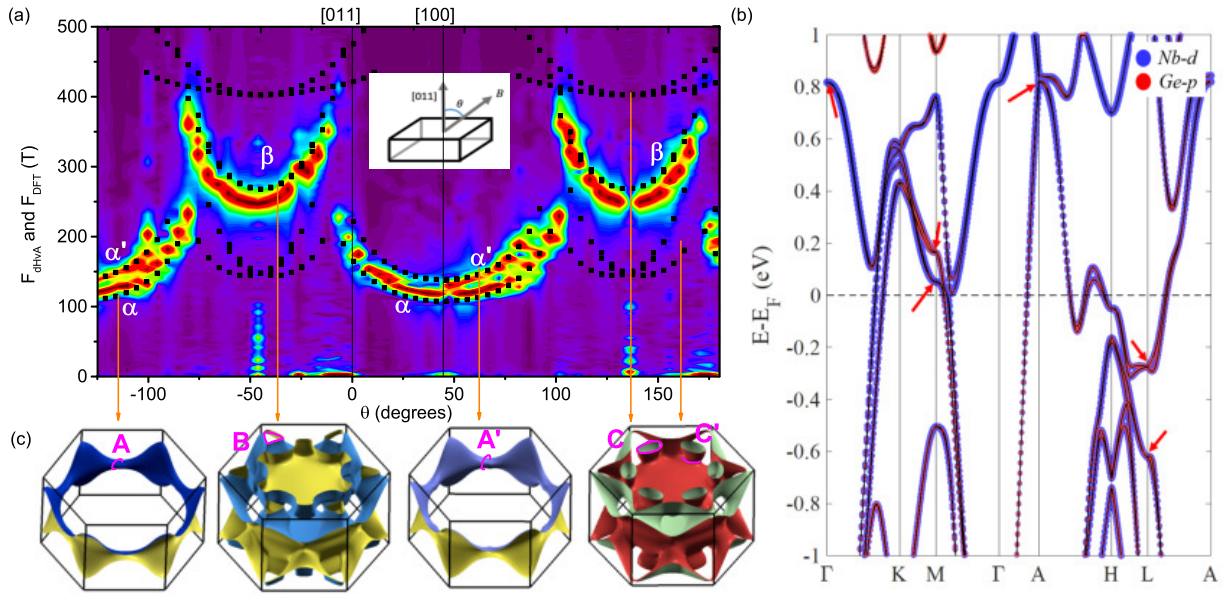

Figure 6.4: (a) The contour plot of the FFT frequencies as a function of angle. Three frequency branches can be distinguished, labeled α, α' and β. Strong spin splitting is observed for α and α'. The black dots correspond to the DFT calculated frequencies. The inset shows the measurement geometry. (b) The orbital-resolved electronic band structure of bulk $NbGe_2$ with SOC. The blue and red dots indicate Nb-4d orbitals and Ge-4p orbitals, respectively. The red arrows denote the positions of Weyl points. (c) The Fermi surfaces in the full BZ of $NbGe_2$. The first three panels show hole like pockets and the last panel an electron pocket. The extremal cross sections with oscillation frequencies less than 500 T are labeled A, A$'$, B, C and C$'$. From a comparison of dHvA and DFT, it is clear that the α, α' and β branches correspond to A, A$'$ and B, respectively.

the location of the Fermi pockets that correspond to F_{DFT} and labeled them as pockets A, A′, B, C, and C′ as shown in Fig. 6.4 (c). The α, α' and β branches correspond to sheets A, A′ and B, respectively. A and A′ are centered around the M Weyl point and B is near the trivial H point.

We noticed that the frequency branches associated with the Fermi pockets C and C′ are missing from the experiment. This is, however, common. In $NbAs_2$, for example, despite the excellent agreement between DFT and experiment, a small frequency branch is completely absent from the observed quantum oscillations [87]. If we increase the E_F by 25 meV to examine if a better agreement is possible, pockets C and C′ become much larger and disappear from the frequency range shown in Fig. 2(a), but the sizes of the F^{A}_{DFT} and $F^{A'}_{DFT}$ become half of the experimental values. It is worth noting that in both cases α, α' and β correspond to pockets A, A′ and B.

6.2 Berry phase revealed by the dHvA oscillations

In order to experimentally investigate the topology of each Fermi pocket, we rotated the sample in such a way so as to only observe the frequencies associated with that pocket. Figure 6.5(a) shows the oscillations in torque as a function of $1/B$ after the subtraction of a polynomial background. The field was applied at an angle of $\approx 120^o$ with respect to the [011] axis. At this angle, only one frequency $F_\beta = 257$ T was observed, as shown in Fig. 6.5 (b).

As shown in Fig. 6.5(a), the amplitude of the oscillations decays rapidly with temperature, suggesting that this pocket is associated with a relatively sizable effective mass. Indeed, using the expression for the thermal damping factor R_T (2.45), a fit of the amplitude at a fixed field of 8.8 T as function of temperature results in the value m^*=1.21(5) m_e, as shown in Fig. 6.5(c). Figure 6.5(d) shows a fit of the oscillation pattern to the LK formula (2.51) with the frequency of 257 T. The phase shift ϕ_i is equal to 0.49.

Next, we investigated the topological character of the spin-split A and A′ pockets. Figure

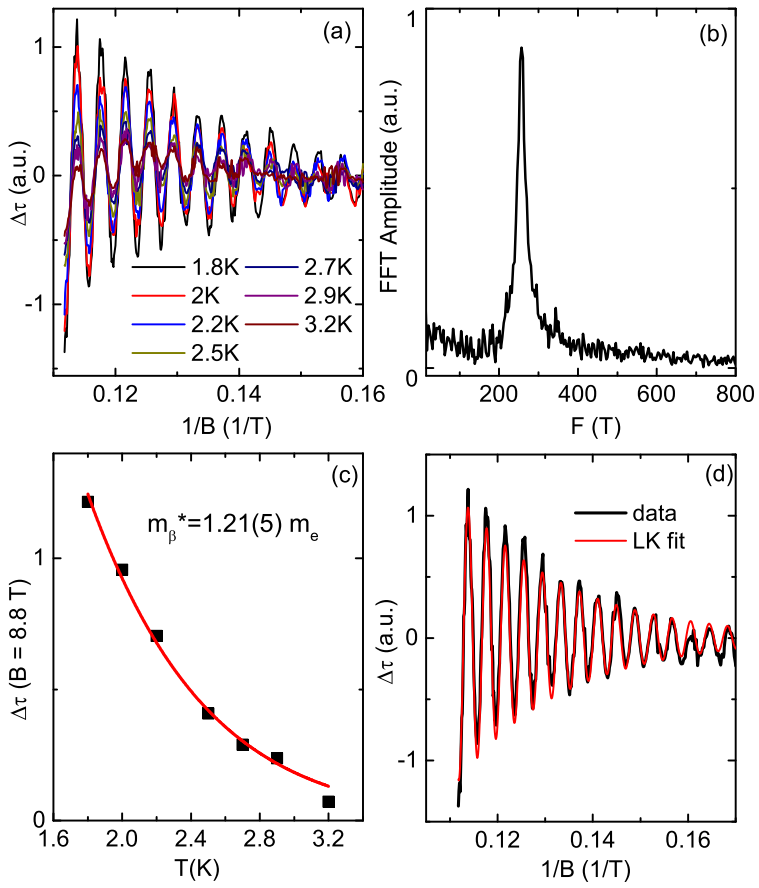

Figure 6.5: F_β branch: (a) $\Delta\tau$, obtained after subtracting a polynomial background, as a function of 1/B for temperatures up to 3.2 K. (b) The FFT plot of $\Delta\tau$, revealing $F_\beta = 257$ T at this angle. (c) A fit of the amplitude at a fixed magnetic field of 8.8 T to obtain the effective mass associated with the orbit. (d) Data at 1.8 K (black line) with LK fit (red line).

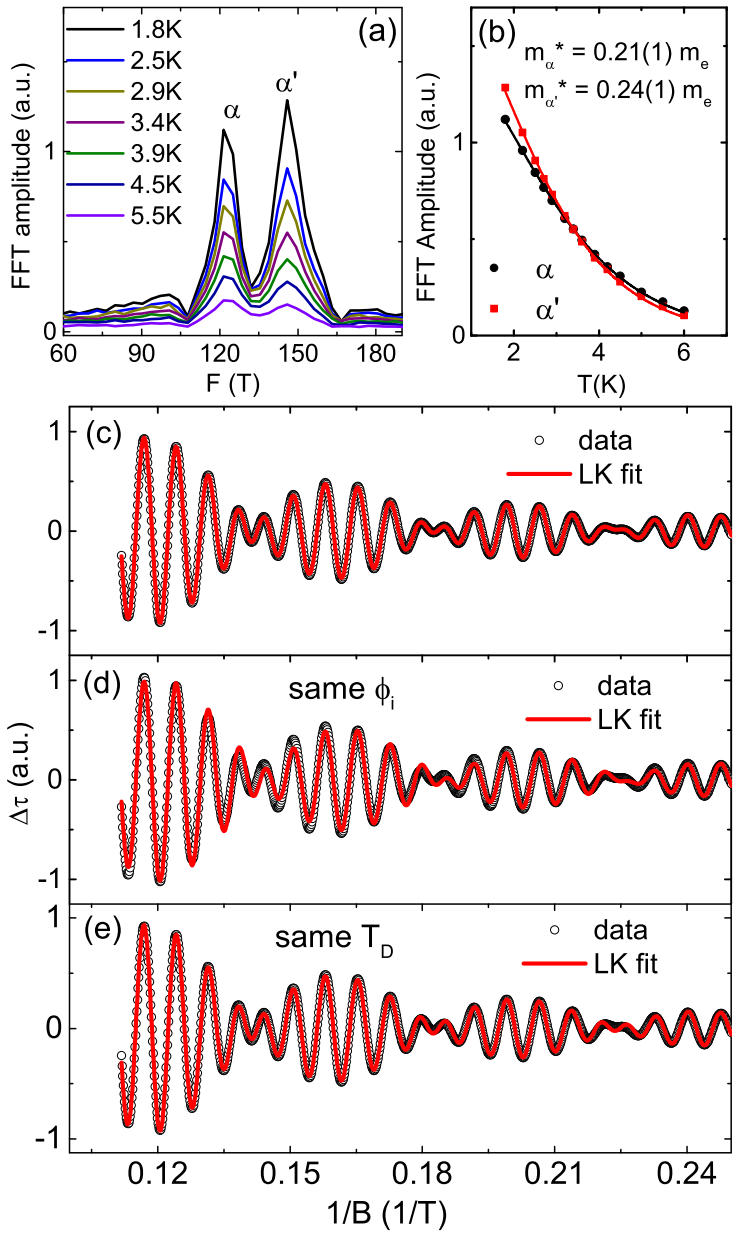

Figure 6.6: (a) The FFT spectrum of the oscillations obtained with the magnetic field at an angle of $\approx 60^o$ with respect to the [011] axis. (b) Fit of the temperature dependence of the FFT amplitude to determine the effective masses. (c)-(e) $\Delta\tau$ (black line) with the LK fit with two frequencies shown in red. For both frequencies, (c) ϕ_i and T_D are all free parameters; (d) T_D are free parameters and ϕ_i are set to be equal; (e) ϕ_i are free parameters and T_D are set to be equal.

6.6(a) shows the FFT spectrum of the oscillations obtained when the magnetic field was applied at an angle of $\approx 60^o$ with respect to the [011] axis at various temperatures. At this angle, the effect of spin splitting can be seen very clearly without the contamination from the β frequency. Figure 6.6(b) shows the temperature dependence of the FFT amplitudes of these two oscillation peaks. An effective field $1/B_{eff} = (1/B_1 + 1/B_2)/2$ with $B_1 = 9$ T and $B_2 = 2.5$ T, the limits of the FFT we performed, were used to fit R_T. The effective masses associated with frequencies α and α' were $0.21(1)m_e$ and $0.24(1)m_e$, respectively. These effective masses are much smaller than $1.21m_e$, but still larger than those in the topological semimetal Cd_3As_2 [16, 92]. Figures 6.6 (c)-(e) show the fits to the LK formula in order to determine the Berry phases and quantum mobilities associated with these pockets. We examined three different cases; that they are characterized by different phase factors and Dingle temperatures (c), that they have the same phase factors (d), and that they have the same Dingle temperatures (e). All expressions seem to fit the data very well, and the phase factors derived from all three fits are quite robust with very similar values. However, since A and A$'$ are very similar (Fig. 2 (c), we believe that they should be characterized by the same Dingle temperatures, therefore the values obtained in Fig. 6.6(e) were adopted.

Table I summarizes the obtained quantum lifetimes τ_q, quantum mobilities μ_q, ϕ_i and Berry phase ϕ_B. Since it is unclear if the positive or negative sign should be used in Eq. 2.51, both situations were considered and summarized in Table I. Since all three Fermi pockets are hole pockets and the data we analyzed was collected near the minima of the extremal cross sections, $\delta = -1/8$ was used in the calculation of the Berry phases, which are summarized in Table 6.1.

A trivial Berry phase was expected for the β branch since Fermi pocket B is near the trivial H point. We therefore believe that the negative sign, which results in a trivial Berry phase of 0.23π, should be used. On the other hand, regardless of the choice of sign, the Berry phases calculated for the α and α' pockets do not allow us to conclude whether they are trivial or not. Interestingly, in a quantum oscillations study of CoSi, despite a long Fermi arc surface state being observed in ARPES measurements [128], a trivial Berry phase

	F(T)	m/m_e	T$_D$ (K)	τ_q (ps)	μ_q (cm^2/ v $\cdot$ s)	sign	ϕ_i	ϕ_B
α	122	0.21	1.2	1.0	8500	+	0.11	1.47 π
						-	***0.61***	***0.47*** π
α'	146	0.24	1.2	1.0	7400	+	0.16	1.57 π
						-	***0.66***	***0.57*** π
β	257	1.21	0.48	2.5	3700	+	0	1.24 π
						-	***0.49***	***0.23*** π

Table 6.1: Effective masses, Dingle temperatures, quantum lifetimes and mobilities, and ϕ_i Berry phases for pockets α, α' and β summarized from Figures 6.6 and 6.5.

was observed for the electron pockets at the Kramers-Weyl point [127] because the linear dispersion region was too far from the Fermi level.

6.3 Quasi linear magnetoresistance arising from open Fermi surfaces

The normal state field-dependent magnetoresistance (MR), which was measured with $H\|[011]$ and is shown in Figures 6.7(a)-(b), is quasi linear and quite high at low temperatures, exceeding 1000% at 2.4 K and 9 T, but decays quickly with increasing temperature. At 100 K, the highest temperature measured, the MR becomes quadratic and only reaches 1% at 9 T. The field-dependent Hall resistivity is shown in Fig. 6.7(c) for a few temperatures. The Hall resistivity is non-linear, agreeing with the previous discussion that both hole and electron pockets are present at the Fermi level. Two-band model fitting cannot be used here because of the linear MR. To get a rough estimate of the carrier concentration, a linear fit of the Hall resistivity at 4 K gives a value of 1.27 $\times$ 10^{22} cm^{-3}. Theoretical models for linear MR have been established for low-carrier-density semimetals with linear dispersions in their ultra-quantum limit [129], which is clearly not the case here since 9 T is too low for $NbGe_2$ to enter the ultra-quantum limit region. The linear MR has also been proposed to be a

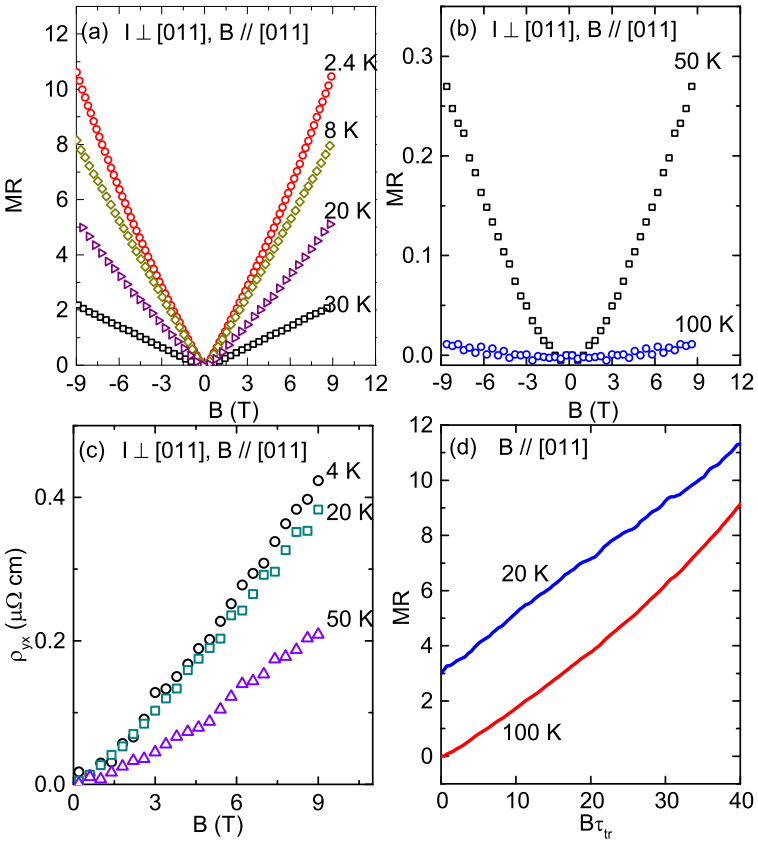

Figure 6.7: (a) and (b) MR at several temperatures. (c) Hall resistivity at various temperatures. (d) The calculated MR at 20 K and 100 K with offset. The calculation was done by solving the Boltzmann transport equation within the relaxation time approximation.

result of the lifting of the topological protection from backscattering by magnetic field [16], mobility fluctuations [92] or the formation of open orbits on their Fermi surface [130].

To understand the possible cause of the linear MR, a theoretical analysis was performed. To obtain the conductivity tensor we solved the Boltzmann transport equation within the relaxation time approximation [131] as implemented in the WannierTool code suit [132,133]. The main equation of interest is

$$\sigma_{ij}^{(n)}(\mathbf{B}) = \frac{e^2}{4\pi^3}\int d\mathbf{k}\tau_n \mathbf{v}_n(\mathbf{k})\overline{\mathbf{v}}_n(\mathbf{k})\left(-\frac{\partial f}{\partial \varepsilon}\right)_{\varepsilon=\varepsilon_n(\mathbf{k})}, \tag{6.1}$$

where n is the band index, e is electronic charge, f is Fermi-Dirac distribution, $\mathbf{v}_n(\mathbf{k})$ is the velocity obtained from the gradient of the band energy and $\overline{\mathbf{v}}_n(\mathbf{k})$ is the velocity averaged

over the past time of the charge carrier written as

$$\overline{\mathbf{v}}_n(\mathbf{k}) = \int_{-\infty}^{0} \frac{dt}{\tau_n} e^{\frac{t}{\tau_n}} \mathbf{v}_n(\mathbf{k}(t)) \ . \tag{6.2}$$

The evolution of $\mathbf{k_n}(t)$ is caused by the orbital motion of charge carrier in the external magnetic filed as written

$$\frac{d\mathbf{k}_n(t)}{dt} = -\frac{e}{\hbar} \mathbf{v}_n(\mathbf{k}(t)) \times \mathbf{B} \ . \tag{6.3}$$

The relaxation time for different bands τ_n is assumed to independent of momentum and within the relaxation time approximation we have neglected the inter-band scattering events. Once the conductivity tensor $\hat{\sigma}$ was obtained we calculated the resistivity using the equation $\hat{\rho} = \hat{\sigma}^{-1}$. As shown in Fig. 6.7(d), we can indeed see linear MR at low temperatures and quadratic MR at high temperatures. This calculation did not take into account SOC or a complicated anomalous velocity that could result from the Berry curvature, and only considered Fermi surface effects. The agreement with our experimental results suggests that the observed linear MR might simply arise from Fermi surface effects, and is most likely due to the presence of open Fermi surfaces.

6.4 Type-I superconductivity with a full superconducting gap

The superconducting properties of $NbGe_2$ were studied using specific heat, magnetization and resistivity measurements. The inset of Fig. 6.8(a) shows the low temperature C_p/T versus T^2, with the red line corresponding to a fit of the normal state data to equation $C_p = C_{el} + C_{ph} = \gamma_n T + \beta T^3$, which results in a Sommerfeld coefficient $\gamma_n = 6.34$ mJ / mol K^{-2} and $\beta = 0.05$ mJ / mol K^{-4}. The size of the peak indicates that $NbGe_2$ is a bulk superconductor and the sharpness of the transition highlights the excellent degree of crystallinity of our sample. The Debye temperature can be calculated from the equation $\Theta_D = (12\pi^4 nR/5\beta)^{1/3}$, where n is the number of atoms in the unit cell. For $NbGe_2$ $n = 3$, and thus our estimate of Θ_D is 485 K. To estimate the electron-phonon coupling constant

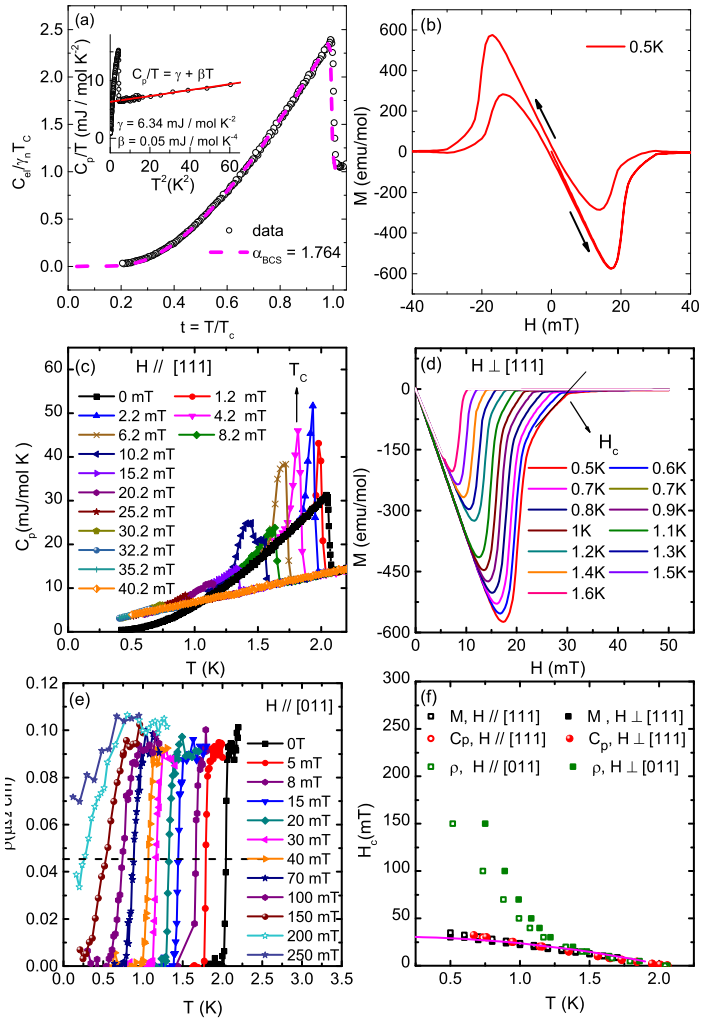

Figure 6.8: (a) A comparison of the electronic part of the specific heat $C_{el}/\gamma_n T_c$ to the predictions of the BCS model. Inset: C_p/T as a function of T^2, with the fit to $C_p/T = \gamma + \beta T^2$ and the derived parameters shown as an inset. (b) $M - H$ loop at 0.5 K. (c) Specific heat with $H \| [111]$ direction at various fields. The criterion inferring T_c is shown. (d) Magnetic isotherms with $H \perp [111]$ at several temperatures. The criterion inferring T_c is shown. (e) Resistivity under various fields with $H \| [011]$. The criterion inferring T_c is shown. (f) $H - T$ phase diagram, with values determined from specific heat, magnetic susceptibility and resistivity measurements. The purple line corresponds to a fit to the expression $H_c(T) = H_c(0)[1 - (T/T_c)^2]$.

λ_{ep}, we used the McMillan formula [134]

$$\lambda_{ep} = \frac{1.04 + \mu^* ln(\frac{\Theta_D}{1.45T_C})}{(1 - 0.62\mu^*) ln(\frac{\Theta_D}{1.45T_C}) - 1.04} \tag{6.4}$$

Using our values for Θ_D, T_c, and using $\mu^* = 0.13$, a common value for intermetallic superconductors [135], we estimated λ_{ep} to be 0.47, suggesting the weak coupling in the superconducting state of $NbGe_2$. Figure 6.8 (a) shows the electronic heat capacity divided by $\gamma_n T_c$ as a function of the reduced temperature T/T_c. $\Delta C_{el}/\ \gamma_n T_c$ was estimated to be $\approx$ 1.36, very close to the BCS value of 1.43. The prediction of the single-band α model [136], for $\alpha = \alpha_{BCS}$, is shown as a pink dashed line. The excellent agreement in the entire temperature range indicates that $NbGe_2$ is a fully gapped weak-coupling superconductor.

The hysteresis curve at 0.5 K (Fig. 6.8(b)) shows a typical type-II SC behavior. However, the specific heat measurements under magnetic field presented in Fig. 6.8(c) provide strong evidence of type-I SC since the application of a magnetic field causes a sudden jump in the specific heat and thus a large latent heat even at 1.2 mT. This suggests a first-order phase transition under field, typical for Type-I SCs [137, 138]. To understand the controversy, we measured several magnetization isotherms from 0.5 K to 1.5 K with $H \perp$ [111] direction, as shown in Fig. 6.8(d) and found Type-II to Type-I crossover behavior upon warming. This is consistent with the data shown in Fig. 6.8(c), where the latent heat was only observed above 1.5 K, suggesting Type-I SC above 1.5 K and Type-II SC below 1.5 K.

The $H - T$ phase diagram is presented in Fig. 6.8(f) using data from all three types of measurements. The thermodynamic critical fields extracted from magnetization and specific heat can be fit to the BCS expression $H_c(T) = H_c(0)[1 - (T/T_c)^2]$, resulting in the value $H_c(0) = 30.9(5)$ mT. However, the critical fields we obtained using resistivity data show distinct behavior. Although a different field direction was used, above 1.3 K, all critical fields are in good agreement, suggesting isotropic superconductivity. Below 1.3 K, however, the critical fields extracted from resistivity measurements show a steep upturn leading to an extrapolated $H_c(0)$ around 10 times of that from the other two measurements. The fact that the upturn of H_c is missing from the specific heat and magnetization data indicates that it is

filamentary superconductivity. This upturn has also been seen in other noncentrosymmetric superconductors, such as AuBe, $LaRhSi_3$ and BiPd [139]. The non-trivial band topology that has been proposed by DFT calculations for $NbGe_2$, AuBe and BiPd raises the question of whether the upturn of H_c could be related to non-trivial topology. Could it be indicative of the topological surface superconductivity which arises from the proximity effect of bulk superconductivity and surface topological electrons, like the one proposed in $FeTe_{1-x}Se_x(x = 0.45)$ and $PbTaSe_2$ [140,141]? Further theoretical work is necessary to address this interesting and apparently common behavior in NCSs.

To understand the possible origin and nature of the superconductivity in $NbGe_2$, we calculated the phonon mode and wave-vector resolved electron-phonon coupling using the EPW code [142, 143].

$$\lambda_{\mathbf{q}\nu} = \frac{\gamma_{\mathbf{q}\nu}}{\pi N\left(\varepsilon_{\mathrm{F}}\right)\omega_{\mathbf{q}\nu}^2} \ , \tag{6.5}$$

where $\mathbf{q}$ is the wave-vector, ν is the phonon branch index, $N\left(\varepsilon_{\mathrm{F}}\right)$ is the electron density at the Fermi energy ε_{F}, $\omega_{\mathbf{q}\nu}$ is the phonon frequency. The phonon linewidth (imaginary part of the phonon self energy) $\gamma_{\mathbf{q}\nu}$ obtained from

$$\begin{aligned}\gamma_{\mathbf{q}\nu} =& 2\pi\omega_{\mathbf{q}\nu}\sum_{nm}\int_{\mathrm{BZ}}\frac{d\mathbf{k}}{\Omega_{\mathrm{BZ}}}\left|g_{mn,\nu}(\mathbf{k},\mathbf{q})\right|^2 \\ &\times\delta\left(\varepsilon_{n\mathbf{k}}-\varepsilon_{\mathrm{F}}\right)\delta\left(\varepsilon_{m\mathbf{k}+\mathbf{q}}-\varepsilon_{\mathbf{F}}\right) \ ,\end{aligned} \tag{6.6}$$

where $g_{mn,\nu}(\mathbf{k},\mathbf{q})$ is the electron-phonon matrix element and m, n are the electronic band indices. The phonon mode and wave vector resolved electron-phonon coupling for $NbGe_2$ is shown in Fig. 6.9, where the size and color of the points depict the weight of the electron-phonon coupling. We found that the modes near the high symmetry point Γ along the $\Gamma - A$ direction has the prominent contribution. We have further calculated the total electron-phonon coupling from the BZ average of the mode-resolved electron-phonon coupling by using $\lambda_{eq} = \sum_{\mathbf{q}\nu} w_{\mathbf{q}\nu}\lambda_{\mathbf{q}\nu}$. Our calculation results in $\lambda_{ep} = 0.67$, which is 30% larger than 0.47, the experimentally obtained value. To estimate the T_c, we used the value of $\lambda_{ep} = 0.67$ with the Allen-Dynes formula

$$T_c = \frac{\omega_{\log}}{1.2}\exp\left[\frac{-1.04(1+\lambda_{ep})}{\lambda_{ep}\left(1-0.62\mu^*\right)-\mu^*}\right], \tag{6.7}$$

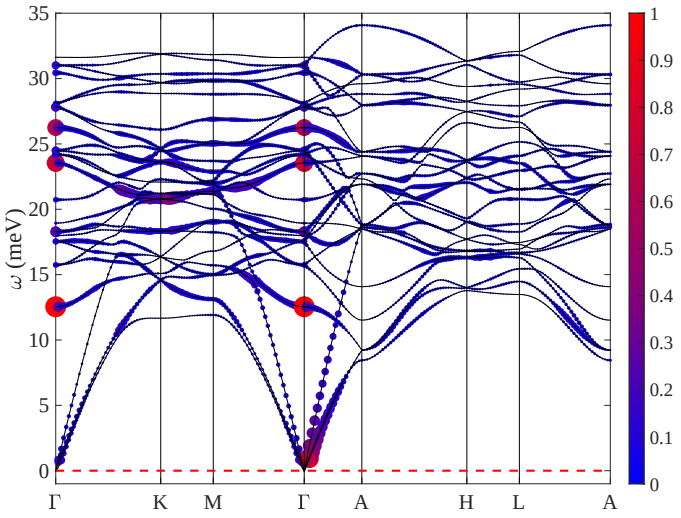

Figure 6.9: The electron-phonon coupling weighted phonon band structure of $NbGe_2$. The size and color of each marker denotes the mode and wave-vector resolved electron-phonon coupling. The colorbar denotes the value of the electron-phonon coupling.

For a screened Coulomb interaction parameter of $\mu^* = 0.13$ or 0.16, the T_c is estimated to be ≈ 5.4 K and 3.8 K respectively, comparable to the experimental value. This suggests that the SC in $NbGe_2$ is indeed electron-phonon mediated.

6.5 Conclusion

In this chapter we presented a systematic study of the de Haas-van Alphen (dHvA) oscillations, magnetotransport, and superconductivity in the Kramers-Weyl semimetal candidate $NbGe_2$. We show that $NbGe_2$ is a type-I chiral superconductor with a T_c of 2.06 K, a full gap, a Type-II to Type-I crossover around 1.5 K and an enhanced critical field from filamentary superconductivity. The study of the dHvA oscillations reveals three distinct frequency branches, β and the spin-split α/α', with cyclotron effective masses of $1.21(5)m_e$, $0.21(1)m_e$ and $0.24m_e$, respectively. The magnetoresistance of $NbGe_2$ exceeds 1000 % at 2.4 K and 9 T, and exhibits quasi-linear behavior at low temperatures. The comparison of our experimental results with first-principles calculations shows excellent agreement and suggests that α and α' correspond to the hole Fermi pockets centered at the Weyl M point and β is associated with

the hole pocket near the trivial H point in the Brillouin Zone. Furthermore, we show that a Van Hove singularity arising from the contributions at the M and H points at the Fermi level, together with the calculated electron-phonon coupling, are strong enough to account for the observed superconductivity. Lastly, our calculation of the conductivity tensor within the relaxation time approximation suggests that the observed linear magnetoresistance most likely arises from the presence of open Fermi surfaces.

CHAPTER 7

Conclusion

In this dissertation I described our studies of the topological semimetals CaAgAs, CaCdGe, CuMnAs and $NbGe_2$. Each material provided us with a platform to ask different questions and utilize a variety of techniques to answer them. Our comparative study of CaAgAs and CaCdGe shed light on the phenomenon of extremely large magnetoresistance in semimetals, CuMnAs was found to have a magnetic structure that led to the prediction of spin-polarized surface states and $NbGe_2$ provided us with an avenue to investigate the interplay between nontrivial topology and superconductivity. The field of topological materials has blossomed over the last decade. Materials with special properties arising from their nontrivial topology are being discovered constantly. As it turns out, nontrivial topology is a far more ubiquitous phenomenon than what one might have expected ten years ago. The next frontier lies in identifying and synthesizing ideal material realizations whose topological properties can be easily probed and are not obscured by contributions from trivial bands. Hopefully the manipulation of topologically protected properties in technological applications is not too far in the future.

Appendix A

Temperature dependent resistance curves for CuMnAs crystals from all synthesis trials

Figures A.1 to A.5 show the temperature dependent resistance curves for batches A-E, highlighting how sensitive the physical properties are to the stoichiometry of the material. Since the pollycrystalline ORT CuMnAs shows a single slope change in the resistivity around 360 K, it was used as a standard to determine the best recipe with pieces whose physical properties were consistent with the polycrystalline ones. Based on this criterion, we can see the best recipe is the one we used for batch A. Although some pieces in other batches may also show only one slope change, the temperature of the phase transition was much lower. For example, in batch E, the transition temperature is around 300 K, indicating a higher level of site/mixing or deficiency in the sample compared to batch A.

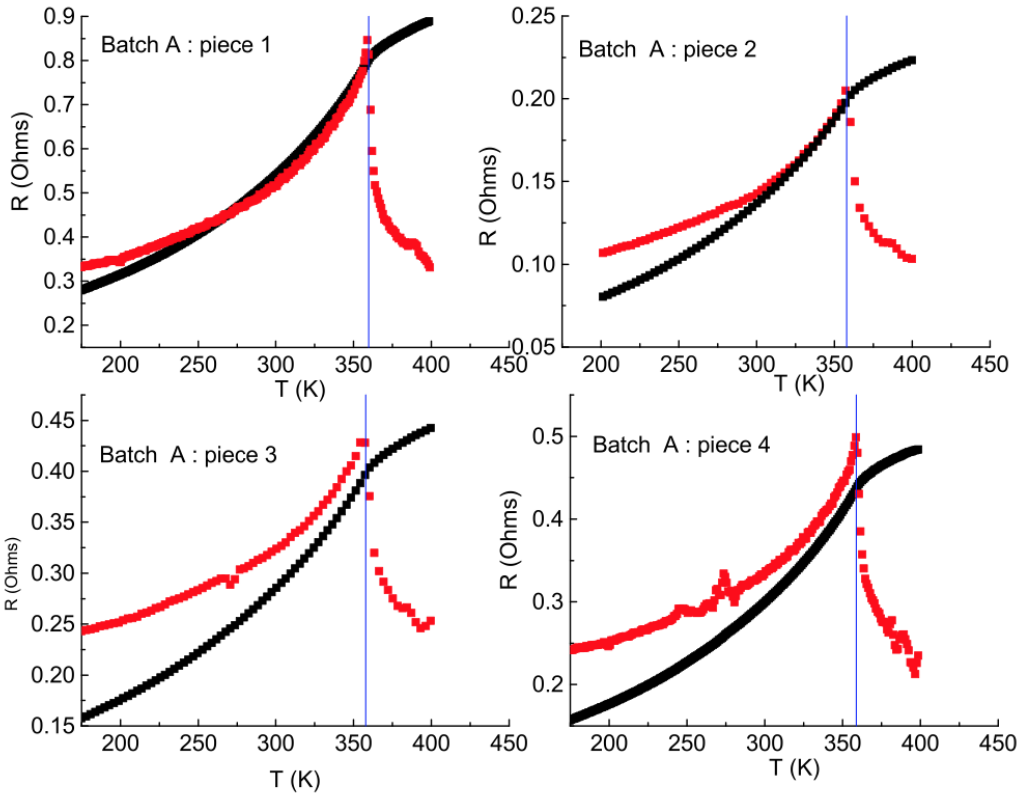

Figure A.1: The temperature dependent resistance for pieces selected from batch A.

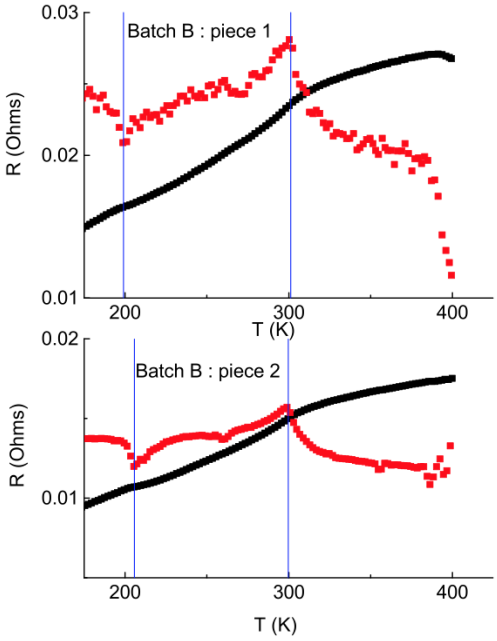

Figure A.2: The temperature dependent resistance for pieces selected from batch B.

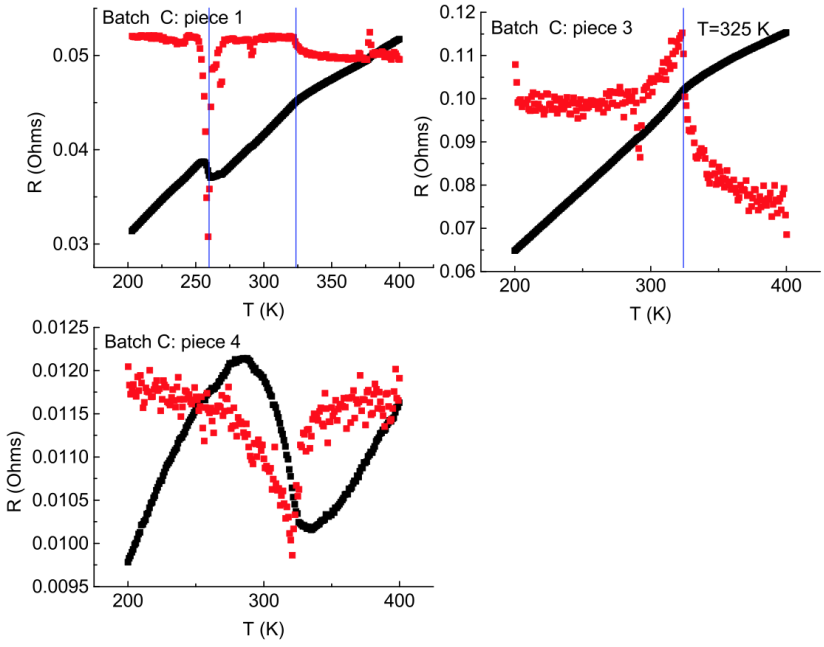

Figure A.3: The temperature dependent resistance for pieces selected from batch C.

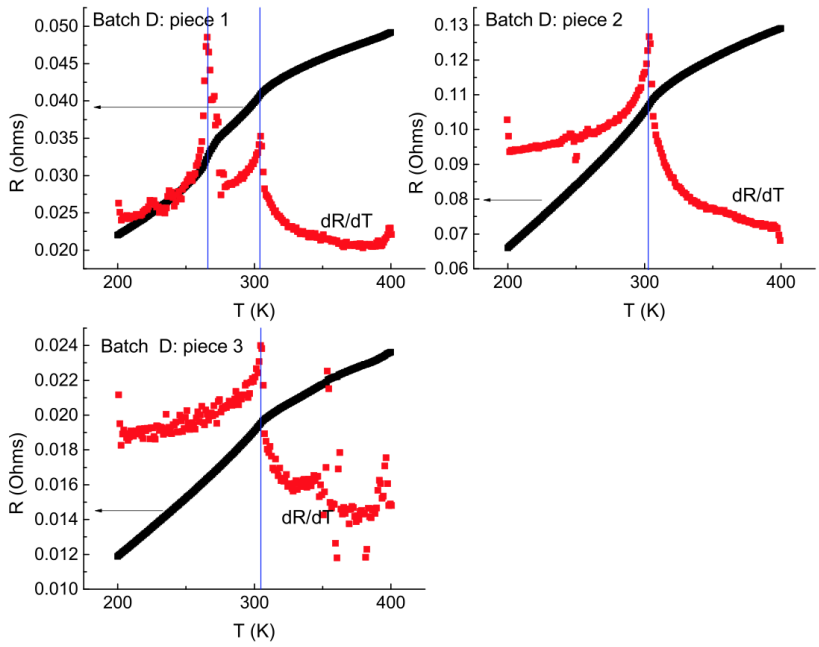

Figure A.4: The temperature dependent resistance for pieces selected from batch D.

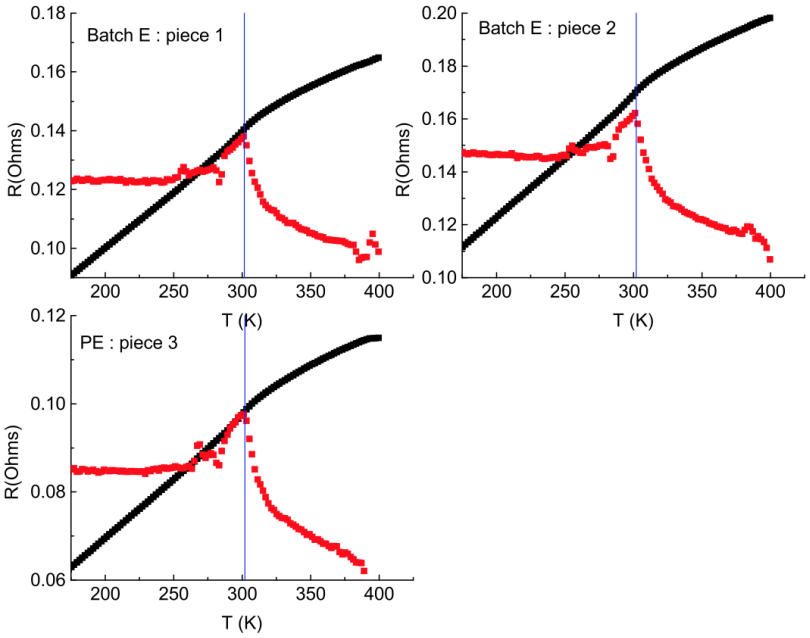

Figure A.5: The temperature dependent resistance for pieces selected from batch E.

Appendix B

First principles calculations

The electronic structure of CaCdGe was studied using first principles calculations based on density functional theory and the full-potential linear augmented plane wave method as implemented in the WIEN2K package [144]. Spin-orbit coupling (SOC) was taken into account in the calculation. The local density and generalized gradient approximations (LDA/GGA) [145] and the Tran-Blaha modified Becke-Johnson (MBJ) [146] exchange potential were used in our calculations.

The first-principles calculations for CuMnAs were carried out using the density functional theory with the projector augmented wave method [147], as implemented in the Vienna ab initio simulation package (VASP) [148]. The Perdew-Burke-Ernzerhof exchange correlation functional and the plane-wave basis with energy cutoff of 300 eV were employed. The inner atomic positions of the lattice were allowed to be fully relaxed until the residual forces were less than 1×103 eV/ Å. The Monkhorst-Pack k points were 9×15×9, and SOC was included in self-consistent electronic structure calculations. The maximally localized Wannier functions were constructed to obtain the tight-binding Hamiltonian [149], which was used to calculate the bulk Fermi surface, surface electronic spectrum, and surface states.

First principles calculations for $NbGe_2$ were carried out within the framework of density functional theory (DFT) [150, 151], with the projector augmented wave (PAW) pseudopotentials [152], as implemented in the Vienna ab initio simulation package (VASP) [148, 153]. The exchange-correlation effects were included within the generalized gradient approximation (GGA) with the Perdew-Burke-Ernzerhof (PBE) parametrization [145]. SOC effects were treated self-consistently to incorporate relativistic effects. To perform the electronic

calculations, we used a plane-wave energy cutoff of 300 eV while the BZ sampling is done by a $21 \times 21 \times 11$ Γ-centered k-mesh [154]. Total energies were converged to 10^{-6} eV in combination with Gaussian type broadening of 0.05 eV. The experimental lattice parameters were used in all calculations, while the ionic positions were relaxed until the residual force on each atom was less than 10^{-3} eV/Å. The Fermi surface calculation was done by employing a tight-binding model obtained through the VASP2WANNIER90 interface [155], and visualization of the Fermi surface was done using the Xcrysden software.

Bibliography

[1] E. Emmanouilidou, B. Shen, X. Deng, T.-R. Chang, A. Shi, G. Kotliar, S.-Y. Xu, and N. Ni, "Magnetotransport properties of the single-crystalline nodal-line semimetal candidates $CaTX(T = Ag, Cd; X = As, Ge)$," *Physical Review B*, vol. 95, p. 245113, Jun 2017.

[2] X.-B. Wang, X.-M. Ma, E. Emmanouilidou, B. Shen, C.-H. Hsu, C.-S. Zhou, Y. Zuo, R.-R. Song, S.-Y. Xu, G. Wang, *et al.*, "Topological surface electronic states in candidate nodal-line semimetal CaAgAs," *Physical Review B*, vol. 96, no. 16, p. 161112, 2017.

[3] E. Emmanouilidou, H. Cao, P. Tang, X. Gui, C. Hu, B. Shen, J. Wu, S.-C. Zhang, W. Xie, and N. Ni, "Magnetic order induces symmetry breaking in the single-crystalline orthorhombic CuMnAs semimetal," *Physical Review B*, vol. 96, p. 224405, Dec 2017.

[4] E. Emmanouilidou, J. Liu, D. Graf, H. Cao, and N. Ni, "Spin-flop phase transition in the orthorhombic antiferromagnetic topological semimetal $Cu_{0.95}MnAs$," *Journal of Magnetism and Magnetic Materials*, vol. 469, pp. 570–573, 2019.

[5] E. Emmanouilidou, S. Mardanya, J. Xing, P. V. S. Reddy, A. Agarwa, T.-R. Chang, and N. Ni, "Fermiology and Type-I superconductivity in the chiral superconductor $NbGe_2$ with Kramers-Weyl Fermions," *Physical Review B*, under review, 2020.

[6] L. Fu, C. L. Kane, and E. J. Mele, "Topological Insulators in Three Dimensions," *Physical Review Letters*, vol. 98, p. 106803, Mar 2007.

[7] J. E. Moore and L. Balents, "Topological invariants of time-reversal-invariant band structures," *Physical Review B*, vol. 75, p. 121306, Mar 2007.

[8] R. Roy, "Z_2 classification of quantum spin hall systems: An approach using time-reversal invariance," *Physical Review B*, vol. 79, p. 195321, May 2009.

[9] D. Hsieh, D. Qian, L. Wray, Y. Xia, Y. S. Hor, R. J. Cava, and M. Z. Hasan, "A topological Dirac insulator in a quantum spin Hall phase," *Nature*, vol. 452, no. 7190, pp. 970–974, 2008.

[10] Y. Xia, D. Qian, D. Hsieh, L. Wray, A. Pal, H. Lin, A. Bansil, D. Grauer, Y. S. Hor, R. J. Cava, and M. Z. Hasan, "Observation of a large-gap topological-insulator class with a single Dirac cone on the surface," *Nature Physics*, vol. 5, no. 6, pp. 398–402, 2009.

[11] D. Hsieh, Y. Xia, D. Qian, L. Wray, J. H. Dil, F. Meier, J. Osterwalder, L. Patthey, J. G. Checkelsky, N. P. Ong, A. V. Fedorov, H. Lin, A. Bansil, D. Grauer, Y. S. Hor, R. J. Cava, and M. Z. Hasan, "A tunable topological insulator in the spin helical Dirac transport regime," *Nature*, vol. 460, no. 7259, pp. 1101–1105, 2009.

[12] Z. Wang, H. Weng, Q. Wu, X. Dai, and Z. Fang, "Three-dimensional Dirac semimetal and quantum transport in Cd_3As_2," *Physical Review B*, vol. 88, p. 125427, Sep 2013.

[13] I. Crassee, R. Sankar, W.-L. Lee, A. Akrap, and M. Orlita, "3D Dirac semimetal Cd_3As_2: A review of material properties," *Physical Review Materials*, vol. 2, no. 12, p. 120302, 2018.

[14] A. J. Rosenberg and T. C. Harman, "Cd_3As_2—a noncubic semiconductor with unusually high electron mobility," *Journal of Applied Physics*, vol. 30, no. 10, pp. 1621–1622, 1959.

[15] W. Żdanowicz, L. Żdanowicz, J. Portal, and S. Askenazy, "Shubnikov-de Haas effect in thin films of cadmium arsenide," *Thin Solid Films*, vol. 61, no. 1, pp. 41–50, 1979.

[16] T. Liang, Q. Gibson, M. N. Ali, M. Liu, R. J. Cava, and N. P. Ong, "Ultrahigh mobility and giant magnetoresistance in the Dirac semimetal Cd_3As_2," *Nature Materials*, vol. 14, pp. 280–284, mar 2015.

[17] J. Feng, Y. Pang, D. Wu, Z. Wang, H. Weng, J. Li, X. Dai, Z. Fang, Y. Shi, and L. Lu, "Large linear magnetoresistance in Dirac semimetal Cd_3As_2 with fermi surfaces close to the Dirac points," *Physical Review B*, vol. 92, p. 081306, Aug 2015.

[18] Z. Liu, B. Zhou, Y. Zhang, Z. Wang, H. Weng, D. Prabhakaran, S.-K. Mo, Z. Shen, Z. Fang, X. Dai, *et al.*, "Discovery of a three-dimensional topological Dirac semimetal, Na_3Bi," *Science*, vol. 343, no. 6173, pp. 864–867, 2014.

[19] Z. Wang, Y. Sun, X.-Q. Chen, C. Franchini, G. Xu, H. Weng, X. Dai, and Z. Fang, "Dirac semimetal and topological phase transitions in A_3Bi (A= Na, K, Rb)," *Physical Review B*, vol. 85, no. 19, p. 195320, 2012.

[20] J. Xiong, S. K. Kushwaha, T. Liang, J. W. Krizan, M. Hirschberger, W. Wang, R. J. Cava, and N. P. Ong, "Evidence for the chiral anomaly in the Dirac semimetal Na_3Bi," *Science*, vol. 350, no. 6259, pp. 413–416, 2015.

[21] H. Weng, C. Fang, Z. Fang, B. A. Bernevig, and X. Dai, "Weyl semimetal phase in noncentrosymmetric transition-metal monophosphides," *Physical Review X*, vol. 5, p. 011029, Mar 2015.

[22] B. Lv, H. Weng, B. Fu, X. Wang, H. Miao, J. Ma, P. Richard, X. Huang, L. Zhao, G. Chen, *et al.*, "Experimental discovery of Weyl semimetal TaAs," *Physical Review X*, vol. 5, no. 3, p. 031013, 2015.

[23] X. Huang, L. Zhao, Y. Long, P. Wang, D. Chen, Z. Yang, H. Liang, M. Xue, H. Weng, Z. Fang, X. Dai, and G. Chen, "Observation of the Chiral-Anomaly-Induced Negative Magnetoresistance in 3D Weyl Semimetal TaAs," *Physical Review X*, vol. 5, p. 031023, Aug 2015.

[24] S. Liang, J. Lin, S. Kushwaha, J. Xing, N. Ni, R. J. Cava, and N. P. Ong, "Experimental tests of the chiral anomaly magnetoresistance in the Dirac-Weyl semimetals Na_3Bi and GdPtBi," *Physical Review X*, vol. 8, no. 3, p. 031002, 2018.

[25] Q. Wang, Y. Xu, R. Lou, Z. Liu, M. Li, Y. Huang, D. Shen, H. Weng, S. Wang, and H. Lei, "Large intrinsic anomalous Hall effect in half-metallic ferromagnet $Co_3Sn_2S_2$ with magnetic Weyl fermions," *Nature Communications*, vol. 9, no. 1, pp. 1–8, 2018.

[26] Y.-J. Hao, P. Liu, Y. Feng, X.-M. Ma, E. F. Schwier, M. Arita, S. Kumar, C. Hu, M. Zeng, Y. Wang, *et al.*, "Gapless surface Dirac cone in antiferromagnetic topological insulator $MnBi_2Te_4$," *Physical Review X*, vol. 9, no. 4, p. 041038, 2019.

[27] C. Hu, K. N. Gordon, P. Liu, J. Liu, X. Zhou, P. Hao, D. Narayan, E. Emmanouilidou, H. Sun, Y. Liu, *et al.*, "A van der waals antiferromagnetic topological insulator with weak interlayer magnetic coupling," *Nature Communications*, vol. 11, no. 1, pp. 1–8, 2020.

[28] C. Hu, L. Ding, K. N. Gordon, B. Ghosh, H.-J. Tien, H. Li, A. G. Linn, S.-W. Lien, C.-Y. Huang, S. Mackey, *et al.*, "Realization of an intrinsic ferromagnetic topological state in $MnBi_8Te_{13}$," *Science Advances*, vol. 6, no. 30, p. eaba4275, 2020.

[29] M. Sato and Y. Ando, "Topological superconductors: a review," *Reports on Progress in Physics*, vol. 80, no. 7, p. 076501, 2017.

[30] M. V. Berry, "Quantal phase factors accompanying adiabatic changes," *Proceedings of the Royal Society of London. A. Mathematical and Physical Sciences*, vol. 392, no. 1802, pp. 45–57, 1984.

[31] D. Xiao, M.-C. Chang, and Q. Niu, "Berry phase effects on electronic properties," *Reviews of modern physics*, vol. 82, no. 3, p. 1959, 2010.

[32] R. Karplus and J. Luttinger, "Hall effect in ferromagnetics," *Physical Review*, vol. 95, no. 5, p. 1154, 1954.

[33] K. v. Klitzing, G. Dorda, and M. Pepper, "New method for high-accuracy determination of the fine-structure constant based on quantized hall resistance," *Physical Review Letters*, vol. 45, no. 6, p. 494, 1980.

[34] M. Z. Hasan and C. L. Kane, "Colloquium: topological insulators," *Reviews of modern physics*, vol. 82, no. 4, p. 3045, 2010.

[35] D. J. Thouless, M. Kohmoto, M. P. Nightingale, and M. den Nijs, "Quantized Hall conductance in a two-dimensional periodic potential," *Physical Review Letters*, vol. 49, no. 6, p. 405, 1982.

[36] B. I. Halperin, "Quantized Hall conductance, current-carrying edge states, and the existence of extended states in a two-dimensional disordered potential," *Physical Review B*, vol. 25, pp. 2185–2190, Feb 1982.

[37] K. Sun, "Time-reversal symmetry, the theorem of Kramers and 3D topological insulator," Lecture Notes, 2012.

[38] C. L. Kane and E. J. Mele, "Z_2 topological order and the quantum spin Hall effect," *Physical Review Letters*, vol. 95, no. 14, p. 146802, 2005.

[39] C. L. Kane and E. J. Mele, "Quantum spin Hall effect in graphene," *Physical Review Letters*, vol. 95, no. 22, p. 226801, 2005.

[40] B. A. Bernevig and S.-C. Zhang, "Quantum Spin Hall Effect," *Physical Review Letters*, vol. 96, p. 106802, Mar 2006.

[41] D. Vanderbilt, *Berry Phases in Electronic Structure Theory: Electric Polarization, Orbital Magnetization and Topological Insulators*. Cambridge University Press, 2018.

[42] L. Fu and C. L. Kane, "Topological insulators with inversion symmetry," *Physical Review B*, vol. 76, p. 045302, Jul 2007.

[43] L. Fu, "Topological crystalline insulators," *Physical Review Letters*, vol. 106, p. 106802, Mar 2011.

[44] S. Murakami, "Phase transition between the quantum spin Hall and insulator phases in 3D: emergence of a topological gapless phase," *New Journal of Physics*, vol. 9, no. 9, p. 356, 2007.

[45] A. Burkov, "Topological semimetals," *Nature Materials*, vol. 15, no. 11, pp. 1145–1148, 2016.

[46] T. M. McCormick, *Electronic and Transport Properties of Weyl Semimetals*. PhD thesis, Ohio State University, 2018.

[47] H. B. Nielsen and M. Ninomiya, "No-go theorem for regularizing chiral fermions," tech. rep., Science Research Council, 1981.

[48] X. Dai, "A group family picture," *Nature Materials*, vol. 15, no. 1, pp. 5–6, 2016.

[49] A. Bernevig, H. Weng, Z. Fang, and X. Dai, "Recent progress in the study of topological semimetals," *Journal of the Physical Society of Japan*, vol. 87, no. 4, p. 041001, 2018.

[50] G. Chang, B. J. Wieder, F. Schindler, D. S. Sanchez, I. Belopolski, S.-M. Huang, B. Singh, D. Wu, T.-R. Chang, T. Neupert, S.-Y. Xu, H. Lin, and M. Z. Hasan, "Topological quantum properties of chiral crystals," *Nature Materials*, vol. 17, no. 11, pp. 978–985, 2018.

[51] S. Blundell, *Magnetism in Condensed Matter*. OUP Oxford, 2001.

[52] J. Hu, S.-Y. Xu, N. Ni, and Z. Mao, "Transport of topological semimetals," *Annual Review of Materials Research*, vol. 49, pp. 207–252, 2019.

[53] A. A. Taskin and Y. Ando, "Berry phase of nonideal Dirac fermions in topological insulators," *Physical Review B*, vol. 84, p. 035301, Jul 2011.

[54] C. Li, C. Wang, B. Wan, X. Wan, H.-Z. Lu, and X. Xie, "Rules for phase shifts of quantum oscillations in topological nodal-line semimetals," *Physical Review Letters*, vol. 120, no. 14, p. 146602, 2018.

[55] M. Tinkham, *Introduction to superconductivity*. Courier Corporation, 2004.

[56] F. London and H. London, "The electromagnetic equations of the supraconductor," *Proceedings of the Royal Society of London. Series A-Mathematical and Physical Sciences*, vol. 149, no. 866, pp. 71–88, 1935.

[57] V. L. Ginzburg and L. D. Landau, "On the theory of superconductivity," in *On Superconductivity and Superfluidity*, pp. 113–137, Springer, 2009.

[58] D. J. Rebar, *Exploring superconductivity in chiral structured AuBe*. PhD thesis, Louisiana State University, 2015.

[59] A. Manchon, H. C. Koo, J. Nitta, S. Frolov, and R. Duine, "New perspectives for Rashba spin-orbit coupling," *Nature Materials*, vol. 14, no. 9, pp. 871–882, 2015.

[60] L. Fu and C. L. Kane, "Superconducting proximity effect and majorana fermions at the surface of a topological insulator," *Physical Review Letters*, vol. 100, p. 096407, Mar 2008.

[61] B. J. Lawson, G. Li, F. Yu, T. Asaba, C. Tinsman, T. Gao, W. Wang, Y. S. Hor, and L. Li, "Quantum oscillations in $Cu_xBi_2Se_3$ in high magnetic fields," *Physical Review B*, vol. 90, p. 195141, Nov 2014.

[62] Z. Liu, X. Yao, J. Shao, M. Zuo, L. Pi, S. Tan, C. Zhang, and Y. Zhang, "Superconductivity with Topological Surface State in $Sr_xBi_2Se_3$," *Journal of the American Chemical Society*, vol. 137, pp. 10512–10515, Aug 2015.

[63] P. C. Canfield and Z. Fisk, "Growth of single crystals from metallic fluxes," *Philosophical Magazine B*, vol. 65, no. 6, pp. 1117–1123, 1992.

[64] B. C. Chakoumakos, H. Cao, F. Ye, A. D. Stoica, M. Popovici, M. Sundaram, W. Zhou, J. S. Hicks, G. W. Lynn, and R. A. Riedel, "Four-circle single-crystal neutron diffractometer at the High Flux Isotope Reactor," *Journal of Applied Crystallography*, vol. 44, pp. 655–658, Jun 2011.

[65] J. M. Perez-Mato, S. V. Gallego, E. S. Tasci, L. Elcoro, G. de la Flor, and M. I. Aroyo, "Symmetry-Based Computational Tools for Magnetic Crystallography," *Annual Review of Materials Research*, vol. 45, no. 1, pp. 217–248, 2015.

[66] J. Rodríguez-Carvajal, "Recent advances in magnetic structure determination by neutron powder diffraction," *Physica B: Condensed Matter*, vol. 192, no. 1, pp. 55–69, 1993.

[67] Y. Wang and R. M. Nandkishore, "Topological surface superconductivity in doped Weyl loop materials," *Physical Review B*, vol. 95, no. 6, p. 060506, 2017.

[68] S. Sur and R. Nandkishore, "Instabilities of Weyl loop semimetals," *New Journal of Physics*, vol. 18, no. 11, p. 115006, 2016.

[69] R. Nandkishore, "Weyl and Dirac loop superconductors," *Physical Review B*, vol. 93, no. 2, p. 020506, 2016.

[70] G. Bian, T.-R. Chang, R. Sankar, S.-Y. Xu, H. Zheng, T. Neupert, C.-K. Chiu, S.-M. Huang, G. Chang, I. Belopolski, D. S. Sanchez, M. Neupane, N. Alidoust, C. Liu, B. Wang, C.-C. Lee, H.-T. Jeng, C. Zhang, Z. Yuan, S. Jia, A. Bansil, F. Chou, H. Lin, and M. Z. Hasan, "Topological nodal-line fermions in spin-orbit metal $PbTaSe_2$," *Nature Communications*, vol. 7, no. 1, p. 10556, 2016.

[71] Y.-H. Chan, C.-K. Chiu, M. Y. Chou, and A. P. Schnyder, "Ca_3P_2 and other topological semimetals with line nodes and drumhead surface states," *Physical Review B*, vol. 93, p. 205132, May 2016.

[72] Y. Chen, Y.-M. Lu, and H.-Y. Kee, "Topological crystalline metal in orthorhombic perovskite iridates," *Nature Communications*, vol. 6, no. 1, p. 6593, 2015.

[73] M. M. Hosen, K. Dimitri, I. Belopolski, P. Maldonado, R. Sankar, N. Dhakal, G. Dhakal, T. Cole, P. M. Oppeneer, D. Kaczorowski, F. Chou, M. Z. Hasan, T. Durakiewicz, and M. Neupane, "Tunability of the topological nodal-line semimetal phase in ZrSiX-type materials ($X = \mathrm{S}, \mathrm{Se}, \mathrm{Te}$)," *Physical Review B*, vol. 95, p. 161101, Apr 2017.

[74] Y. Kim, B. J. Wieder, C. L. Kane, and A. M. Rappe, "Dirac line nodes in inversion-symmetric crystals," *Physical Review Letters*, vol. 115, p. 036806, Jul 2015.

[75] Q.-F. Liang, J. Zhou, R. Yu, Z. Wang, and H. Weng, "Node-surface and node-line fermions from nonsymmorphic lattice symmetries," *Physical Review B*, vol. 93, p. 085427, Feb 2016.

[76] H. Weng, Y. Liang, Q. Xu, R. Yu, Z. Fang, X. Dai, and Y. Kawazoe, "Topological node-line semimetal in three-dimensional graphene networks," *Physical Review B*, vol. 92, p. 045108, Jul 2015.

[77] M. Zeng, C. Fang, G. Chang, Y.-A. Chen, T. Hsieh, A. Bansil, H. Lin, and L. Fu, "Topological semimetals and topological insulators in rare earth monopnictides," *arXiv:1504.03492*.

[78] D. Gosálbez-Martínez, I. Souza, and D. Vanderbilt, "Chiral degeneracies and fermi-surface chern numbers in bcc Fe," *Physical Review B*, vol. 92, p. 085138, Aug 2015.

[79] L. M. Schoop, M. N. Ali, C. Straßer, A. Topp, A. Varykhalov, D. Marchenko, V. Duppel, S. S. P. Parkin, B. V. Lotsch, and C. R. Ast, "Dirac cone protected by non-symmorphic symmetry and three-dimensional Dirac line node in ZrSiS," *Nature Communications*, vol. 7, no. 1, p. 11696, 2016.

[80] J. Hu, Z. Tang, J. Liu, X. Liu, Y. Zhu, D. Graf, K. Myhro, S. Tran, C. N. Lau, J. Wei, and Z. Mao, "Evidence of topological nodal-line fermions in ZrSiSe and ZrSiTe," *Physical Review Letters*, vol. 117, p. 016602, Jun 2016.

[81] Y. Ai, Y. Youichi, T. Yukio, and O. Yoshihiko, "Line-Node Dirac Semimetal and Topological Insulating Phase in Noncentrosymmetric Pnictides CaAgX (X = P, As)," *Journal of the Physical Society of Japan*, vol. 85, no. 1, p. 13708, 2016.

[82] O. Yoshihiko, I. Takumi, Y. Ai, Y. Youichi, and T. Koshi, "Low Carrier Density Metal Realized in Candidate Line-Node Dirac Semimetals CaAgP and CaAgAs," *Journal of the Physical Society of Japan*, vol. 85, no. 12, p. 123701, 2016.

[83] P. R. Subramanian, "Ca-Cd Binary Phase Diagram." ASM Alloy Phase Diagrams Database. http://www.asminternational.org.

[84] E. Dichi, G. Morgant, B. Legendre, and S. Fries, "Cd-Ge Binary Phase Diagram." ASM Alloy Phase Diagrams Database. http://www.asminternational.org.

[85] C.-L. Zhang, S.-Y. Xu, I. Belopolski, Z. Yuan, Z. Lin, B. Tong, G. Bian, N. Alidoust, C.-C. Lee, S.-M. Huang, T.-R. Chang, G. Chang, C.-H. Hsu, H.-T. Jeng, M. Neupane, D. S. Sanchez, H. Zheng, J. Wang, H. Lin, C. Zhang, H.-Z. Lu, S.-Q. Shen, T. Neupert, M. Zahid Hasan, and S. Jia, "Signatures of the Adler–Bell–Jackiw chiral anomaly in a Weyl fermion semimetal," *Nature Communications*, vol. 7, no. 1, p. 10735, 2016.

[86] M. N. Ali, J. Xiong, S. Flynn, J. Tao, Q. D. Gibson, L. M. Schoop, T. Liang, N. Haldolaarachchige, M. Hirschberger, N. P. Ong, and R. J. Cava, "Large, non-saturating magnetoresistance in WTe_2," *Nature*, vol. 514, no. 7521, pp. 205–208, 2014.

[87] B. Shen, X. Deng, G. Kotliar, and N. Ni, "Fermi surface topology and negative longitudinal magnetoresistance observed in the semimetal $NbAs_2$," *Physical Review B*, vol. 93, p. 195119, May 2016.

[88] C. Shekhar, A. K. Nayak, Y. Sun, M. Schmidt, M. Nicklas, I. Leermakers, U. Zeitler, Y. Skourski, J. Wosnitza, Z. Liu, Y. Chen, W. Schnelle, H. Borrmann, Y. Grin, C. Felser, and B. Yan, "Extremely large magnetoresistance and ultrahigh mobility in the topological Weyl semimetal candidate NbP," *Nature Physics*, vol. 11, no. 8, pp. 645–649, 2015.

[89] Y. Zhao, H. Liu, C. Zhang, H. Wang, J. Wang, Z. Lin, Y. Xing, H. Lu, J. Liu, Y. Wang, S. M. Brombosz, Z. Xiao, S. Jia, X. C. Xie, and J. Wang, "Anisotropic fermi surface and quantum limit transport in high mobility three-dimensional dirac semimetal Cd_3As_2," *Physical Review X*, vol. 5, p. 031037, Sep 2015.

[90] Y. Zhao, H. Liu, J. Yan, W. An, J. Liu, X. Zhang, H. Wang, Y. Liu, H. Jiang, Q. Li, *et al.*, "Anisotropic magnetotransport and exotic longitudinal linear magnetoresistance in WTe_2 crystals," *Physical Review B*, vol. 92, no. 4, p. 041104, 2015.

[91] J. Xiong, S. Kushwaha, J. Krizan, T. Liang, R. J. Cava, and N. P. Ong, "Anomalous conductivity tensor in the Dirac semimetal Na_3Bi," *Europhysics Letters*, vol. 114, p. 27002, Apr 2016.

[92] A. Narayanan, M. D. Watson, S. F. Blake, N. Bruyant, L. Drigo, Y. L. Chen, D. Prabhakaran, B. Yan, C. Felser, T. Kong, P. C. Canfield, and A. I. Coldea, "Linear magnetoresistance caused by mobility fluctuations in n-Doped Cd_3As_2," *Physical Review Letters*, vol. 114, p. 117201, Mar 2015.

[93] R. Xu, A. Husmann, T. F. Rosenbaum, M.-L. Saboungi, J. E. Enderby, and P. B. Littlewood, "Large magnetoresistance in non-magnetic silver chalcogenides," *Nature*, vol. 390, no. 6655, pp. 57–60, 1997.

[94] T. Khouri, U. Zeitler, C. Reichl, W. Wegscheider, N. E. Hussey, S. Wiedmann, and J. C. Maan, "Linear magnetoresistance in a quasifree two-dimensional electron gas in an ultrahigh mobility gaas quantum well," *Physical Review Letters*, vol. 117, p. 256601, Dec 2016.

[95] Y. Xing, H. Wang, C.-K. Li, X. Zhang, J. Liu, Y. Zhang, J. Luo, Z. Wang, Y. Wang, L. Ling, M. Tian, S. Jia, J. Feng, X.-J. Liu, J. Wei, and J. Wang, "Superconductivity in topologically nontrivial material Au_2Pb," *npj Quantum Materials*, vol. 1, no. 1, p. 16005, 2016.

[96] A. Pippard, *Magnetoresistance in Metals*. Cambridge University Press, 1989.

[97] Y.-Y. Lv, X. Li, J. Zhang, B. Pang, S.-S. Chen, L. Cao, B.-B. Zhang, D. Lin, Y. B. Chen, S.-H. Yao, J. Zhou, S.-T. Zhang, M.-H. Lu, M. Tian, and Y.-F. Chen, "Mobility-controlled extremely large magnetoresistance in perfect electron-hole compensated $\alpha - WP_2$ crystals," *Physical Review B*, vol. 97, p. 245151, Jun 2018.

[98] M. J. Manfra, S. H. Simon, K. W. Baldwin, A. M. Sergent, K. W. West, R. J. Molnar, and J. Caissie, "Quantum and transport lifetimes in a tunable low-density AlGaN/GaN two-dimensional electron gas," *Applied Physics Letters*, vol. 85, no. 22, pp. 5278–5280, 2004.

[99] Y. Kwan, P. Reiss, Y. Han, M. Bristow, D. Prabhakaran, D. Graf, A. McCollam, S. Parameswaran, and A. Coldea, "Quantum oscillations probe the Fermi surface topology of the nodal-line semimetal CaAgAs," *Physical Review Research*, vol. 2, no. 1, p. 012055, 2020.

[100] F. MácA, J. Mašek, O. Stelmakhovych, X. Martí, H. Reichlová, K. Uhlířová, P. Beran, P. Wadley, V. Novák, and T. Jungwirth, "Room-temperature antiferromagnetism in CuMnAs," *Journal of Magnetism and Magnetic Materials*, vol. 324, no. 8, pp. 1606–1612, 2012.

[101] P. Tang, Q. Zhou, G. Xu, and S.-C. Zhang, "Dirac fermions in an antiferromagnetic semimetal," *Nature Physics*, vol. 12, no. 12, pp. 1100–1104, 2016.

[102] P. Wadley, V. Hills, M. R. Shahedkhah, K. W. Edmonds, R. P. Campion, V. Novák, B. Ouladdiaf, D. Khalyavin, S. Langridge, V. Saidl, P. Nemec, A. W. Rushforth, B. L. Gallagher, S. S. Dhesi, F. Maccherozzi, J. Železný, and T. Jungwirth, "Antiferromagnetic structure in tetragonal CuMnAs thin films," *Scientific Reports*, vol. 5, p. 17079, nov 2015.

[103] P. Wadley, B. Howells, J. Železný, C. Andrews, V. Hills, R. P. Campion, V. Novák, K. Olejník, F. Maccherozzi, S. S. Dhesi, S. Y. Martin, T. Wagner, J. Wunderlich, F. Freimuth, Y. Mokrousov, J. Kuneš, J. S. Chauhan, M. J. Grzybowski, A. W. Rushforth, K. W. Edmonds, B. L. Gallagher, and T. Jungwirth, "Electrical switching of an antiferromagnet," *Science*, vol. 351, no. 6273, pp. 587–590, 2016.

[104] L. Šmejkal, J. Železný, J. Sinova, and T. Jungwirth, "Electric Control of Dirac Quasiparticles by Spin-Orbit Torque in an Antiferromagnet," *Physical Review Letters*, vol. 118, p. 106402, Mar 2017.

[105] K. Uhlířová, R. Tarasenko, F. J. Martínez-Casado, B. Vondráčková, and Z. Matěj, "Synthesis and single crystal study of $CuMn_3As_2$ and $Cu_2Mn_4As_3$," *Journal of Alloys and Compounds*, vol. 650, pp. 224–227, 2015.

[106] T. Chatterji, *Neutron scattering from magnetic materials*. Elsevier, 2005.

[107] R. Li, J. Wang, X.-L. Qi, and S.-C. Zhang, "Dynamical axion field in topological magnetic insulators," *Nature Physics*, vol. 6, no. 4, pp. 284–288, 2010.

[108] T. Jungwirth, X. Marti, P. Wadley, and J. Wunderlich, "Antiferromagnetic spintronics," *Nature Nanotechnology*, vol. 11, p. 231, mar 2016.

[109] M. B. Jungfleisch, W. Zhang, and A. Hoffmann, "Perspectives of antiferromagnetic spintronics," *Physics Letters A*, vol. 382, no. 13, pp. 865–871, 2018.

[110] N. J. Poulis, J. van den Handel, J. Ubbink, J. A. Poulis, and C. J. Gorter, "On antiferromagnetism in a single crystal," *Physical Review*, vol. 82, pp. 552–552, May 1951.

[111] H. Yamauchi, H. Hiroyoshi, M. Yamada, H. Watanabe, and H. Takei, "Spin flopping in $MnTiO_3$," *Journal of Magnetism and Magnetic Materials*, vol. 31-34, pp. 1071–1072, 1983.

[112] M. Wolf, K. Ruck, D. Eckert, G. Krabbes, and K.-H. Müller, "Spin—flop transition in the low-dimensional compound $Ba_3Cu_2O_4Cl_2$," *Journal of Magnetism and Magnetic Materials*, vol. 196-197, pp. 569–570, 1999.

[113] W. Zhang, K. Nadeem, H. Xiao, R. Yang, B. Xu, H. Yang, and X. G. Qiu, "Spin-flop transition and magnetic phase diagram in $CaCo_2As_2$ revealed by torque measurements," *Physical Review B*, vol. 92, p. 144416, Oct 2015.

[114] C. B. Liu, Z. Z. He, Y. J. Liu, R. Chen, M. M. Shi, H. P. Zhu, C. Dong, and J. F. Wang, "Magnetic anisotropy and spin-flop transition of $NiWO_4$ single crystals," *Journal of Magnetism and Magnetic Materials*, vol. 444, pp. 190–192, Dec. 2017.

[115] F. L. A. Machado, P. R. T. Ribeiro, J. Holanda, R. L. Rodríguez-Suárez, A. Azevedo, and S. M. Rezende, "Spin-flop transition in the easy-plane antiferromagnet nickel oxide," *Physical Review B*, vol. 95, p. 104418, Mar. 2017.

[116] G. Gitgeatpong, M. Suewattana, S. Zhang, A. Miyake, M. Tokunaga, P. Chanlert, N. Kurita, H. Tanaka, T. J. Sato, Y. Zhao, and K. Matan, "High-field magnetization and magnetic phase diagram of $\alpha-Cu_2V_2O_7$," *Physical Review B*, vol. 95, p. 245119, Jun 2017.

[117] X. Tan, V. O. Garlea, K. Kovnir, C. M. Thompson, T. Xu, H. Cao, P. Chai, Z. P. Tener, S. Yan, P. Xiong, and M. Shatruk, "Complex magnetic phase diagram with multistep spin-flop transitions in $La_{0.25}Pr_{0.75}Co_2P_2$," *Physical Review B*, vol. 95, p. 024428, Jan 2017.

[118] F. B. Anderson and H. B. Callen, "Statistical Mechanics and Field-Induced Phase Transitions of the Heisenberg Antiferromagnet," *Physical Review*, vol. 136, pp. A1068–A1087, Nov 1964.

[119] H.-F. Li, "Possible ground states and parallel magnetic-field-driven phase transitions of collinear antiferromagnets," *Npj Computational Materials*, vol. 2, p. 16032, oct 2016.

[120] C. M. Knoedler and D. H. Douglass, "Superconductivity in $NbGe_2$ and isostructural C-40 compounds," *Journal of Low Temperature Physics*, vol. 37, no. 1, pp. 189–218, 1979.

[121] J. P. Remeika, A. S. Cooper, Z. Fisk, and D. C. Johnston, "Superconductivity of single-crystal NbGe2," *Journal of the Less Common Metals*, vol. 62, pp. 211–213, 1978.

[122] M. Smidman, M. Salamon, H. Yuan, and D. Agterberg, "Superconductivity and spin–orbit coupling in non-centrosymmetric materials: A review," *Reports on Progress in Physics*, vol. 80, no. 3, p. 036501, 2017.

[123] W. Xie, P. Zhang, B. Shen, W. Jiang, G. Pang, T. Shang, C. Cao, M. Smidman, and H. Yuan, "CaPtAs: A new noncentrosymmetric superconductor," *Science China Physics, Mechanics & Astronomy*, vol. 63, no. 3, p. 237412, 2020.

[124] B. Li, C. Xu, W. Zhou, W. Jiao, R. Sankar, F. Zhang, H. Hou, X. Jiang, B. Qian, B. Chen, *et al.*, "Evidence of s-wave superconductivity in the noncentrosymmetric La_7Ir_3," *Scientific Reports*, vol. 8, no. 1, pp. 1–10, 2018.

[125] H. Okamoto, "Ge-Nb Binary Phase Diagram." ASM Alloy Phase Diagrams Database. http://www.asminternational.org.

[126] H. Tsutsumi, Y. Miura, H. Harima, F. Honda, and Y. Ōnuki, "Split Fermi Surface Properties of VSi_2 without Mirror Planes in the Chiral Crystal Structure," *Journal of the Physical Society of Japan*, vol. 82, no. 9, p. 094604, 2013.

[127] X. Xu, X. Wang, T. A. Cochran, D. S. Sanchez, G. Chang, I. Belopolski, G. Wang, Y. Liu, H.-J. Tien, X. Gui, *et al.*, "Crystal growth and quantum oscillations in the topological chiral semimetal CoSi," *Physical Review B*, vol. 100, no. 4, p. 045104, 2019.

[128] D. S. Sanchez, I. Belopolski, T. A. Cochran, X. Xu, J.-X. Yin, G. Chang, W. Xie, K. Manna, V. Süß, C.-Y. Huang, *et al.*, "Discovery of topological chiral crystals with helicoid arc states," *arXiv:1812.04466*, 2018.

[129] A. A. Abrikosov, "Quantum magnetoresistance," *Physical Review B*, vol. 58, pp. 2788–2794, Aug 1998.

[130] B. Wu, V. Barrena, H. Suderow, and I. Guillamón, "Huge linear magnetoresistance due to open orbits in γ- $PtBi_2$," *Physical Review Research*, vol. 2, no. 2, p. 022042, 2020.

[131] N. W. Ashcroft and N. D. Mermin, "Solid state physics by Neil W. Ashcroft and N. David Mermin.," 1976.

[132] Q. Wu, S. Zhang, H.-F. Song, M. Troyer, and A. A. Soluyanov, "Wanniertools: An open-source software package for novel topological materials," *Computer Physics Communications*, vol. 224, pp. 405–416, 2018.

[133] T. Zhang, Y. Jiang, Z. Song, H. Huang, Y. He, Z. Fang, H. Weng, and C. Fang, "Catalogue of topological electronic materials," *Nature*, vol. 566, no. 7745, pp. 475–479, 2019.

[134] W. McMillan, "Transition temperature of strong-coupled superconductors," *Physical Review*, vol. 167, no. 2, p. 331, 1968.

[135] D. Singh, J. Barker, A. Thamizhavel, A. Hillier, D. M. Paul, and R. Singh, "Superconducting properties and μSR study of the noncentrosymmetric superconductor $Nb_{0.5}Os_{0.5}$," *Journal of Physics: Condensed Matter*, vol. 30, no. 7, p. 075601, 2018.

[136] D. C. Johnston, "Elaboration of the α-model derived from the bcs theory of superconductivity," *Superconductor Science and Technology*, vol. 26, no. 11, p. 115011, 2013.

[137] E. Svanidze and E. Morosan, "Type-I superconductivity in $ScGa_3$ and $LuGa_3$ single crystals," *Physical Review B*, vol. 85, no. 17, p. 174514, 2012.

[138] D. C. Peets, E. Cheng, T. Ying, M. Kriener, X. Shen, S. Li, and D. Feng, "Type-I superconductivity in Al_6Re," *Physical Review B*, vol. 99, no. 14, p. 144519, 2019.

[139] D. J. Rebar, S. M. Birnbaum, J. Singleton, M. Khan, J. Ball, P. Adams, J. Y. Chan, D. Young, D. A. Browne, and J. F. DiTusa, "Fermi surface, possible unconventional fermions, and unusually robust resistive critical fields in the chiral-structured superconductor AuBe," *Physical Review B*, vol. 99, no. 9, p. 094517, 2019.

[140] P. Zhang, K. Yaji, T. Hashimoto, Y. Ota, T. Kondo, K. Okazaki, Z. Wang, J. Wen, G. Gu, H. Ding, *et al.*, "Observation of topological superconductivity on the surface of an iron-based superconductor," *Science*, vol. 360, no. 6385, pp. 182–186, 2018.

[141] T.-R. Chang, P.-J. Chen, G. Bian, S.-M. Huang, H. Zheng, T. Neupert, R. Sankar, S.-Y. Xu, I. Belopolski, G. Chang, *et al.*, "Topological Dirac surface states and superconducting pairing correlations in $PbTaSe_2$," *Physical Review B*, vol. 93, no. 24, p. 245130, 2016.

[142] E. R. Margine and F. Giustino, "Anisotropic Migdal-Eliashberg theory using Wannier functions," *Physical Review B*, vol. 87, no. 2, p. 024505, 2013.

[143] S. Poncé, E. R. Margine, C. Verdi, and F. Giustino, "Epw: Electron–phonon coupling, transport and superconducting properties using maximally localized wannier functions," *Computer Physics Communications*, vol. 209, pp. 116–133, 2016.

[144] P. Blaha, K. Schwarz, G. Madsen, D. Kvasnicka, and J. Luitz, "Wien2k: An augmented plane wave plus local orbitals program for calculating crystal properties," *Technische Universität Wien, Wien*, vol. 28, 01 2001.

[145] J. P. Perdew, K. Burke, and M. Ernzerhof, "Generalized gradient approximation made simple," *Physical Review Letters*, vol. 77, pp. 3865–3868, Oct 1996.

[146] F. Tran and P. Blaha, "Accurate band gaps of semiconductors and insulators with a semilocal exchange-correlation potential," *Physical Review Letters*, vol. 102, p. 226401, Jun 2009.

[147] P. E. Blöchl, "Projector augmented-wave method," *Physical Review B*, vol. 50, pp. 17953–17979, Dec 1994.

[148] G. Kresse and J. Furthmüller, "Efficient iterative schemes for ab initio total-energy calculations using a plane-wave basis set," *Physical Review B*, vol. 54, pp. 11169–11186, Oct 1996.

[149] A. A. Mostofi, J. R. Yates, Y.-S. Lee, I. Souza, D. Vanderbilt, and N. Marzari, "wannier90: A tool for obtaining maximally-localised Wannier functions," *Computer Physics Communications*, vol. 178, no. 9, pp. 685–699, 2008.

[150] P. Hohenberg and W. Kohn, "Inhomogeneous electron gas," *Physical Review*, vol. 136, no. 3B, p. B864, 1964.

[151] W. Kohn and L. J. Sham, "Self-consistent equations including exchange and correlation effects," *Physical Review*, vol. 140, no. 4A, p. A1133, 1965.

[152] P. E. Blöchl, "Projector augmented-wave method," *Physical Review B*, vol. 50, no. 24, p. 17953, 1994.

[153] G. Kresse and D. Joubert, "From ultrasoft pseudopotentials to the projector augmented-wave method," *Physical review B*, vol. 59, no. 3, p. 1758, 1999.

[154] H. J. Monkhorst and J. D. Pack, "Special points for Brillouin-zone integrations," *Physical Review B*, vol. 13, no. 12, p. 5188, 1976.

[155] N. Marzari and D. Vanderbilt, "Maximally localized generalized Wannier functions for composite energy bands," *Physical Review B*, vol. 56, no. 20, p. 12847, 1997.